UNIVERSITÀ DELLA CALABRIA

UNIVERSITA' DELLA CALABRIA

Dipartimento di Fisica

Scuola di Dottorato

Scienza e Tecnica "Bernardino Telesio"

Indirizzo

Fisica dei Sistemi Complessi: Diffusione degli Inquinanti in Atmosfera

---

XXVIII CICLO

A MODELLING STUDY OF ATMOSPHERIC CYCLE OF MERCURY AND ITS EXCHANGE PROCESSES AT ENVIRONMENTAL INTERFACES

Settore Scientifico Disciplinare FIS/06

Direttore: Prof. Roberto Bartolino

Supervisore: Prof. Vincenzo Carbone

Prof. Nicola Pirrone

Dr. Ian M. Hedgecock

Dottorando: Dr De Simone Francesco

A Modelling Study of Atmospheric Cycle of Mercury and its Exchange Processes at Environmental Interfaces

A DISSERTATION PRESENTED

BY

FRANCESCO DE SIMONE

TO

THE DEPARTMENT OF PHYSICS

IN PARTIAL FULFILLMENT OF THE REQUIREMENTS

FOR THE DEGREE OF

DOCTOR OF PHILOSOPHY

IN THE SUBJECT OF

BERNARDINO TELESIO SCIENCE AND TECHNOLOGY DOCTORATE SCHOOL

UNIVERSITY OF CALABRIA

RENDE, ITALY

NOVEMBER 2015

Thesis advisor: V. Carbone, N. Pirrone, I. M. Hedgecock Francesco De Simone

A Modelling Study of Atmospheric Cycle of Mercury and its Exchange Processes at Environmental Interfaces

Abstract

Since ancient times human activities have significantly altered the natural global Mercury (Hg) cycle through emissions to the environment. Hg is a global pollutant since its predominant atmospheric form, elemental Hg, reacts relatively slowly with the more abundant atmospheric oxidants and is therefore transported long distances from its emission source. Once oxidised however Hg is readily deposited, an can then be converted to the toxic monomethylmercury (MeHg) in soils and natural waters. MeHg is able to bioaccumulate and biomagnify, up to levels at which it is harmful to human health. Mercury pollution is therefore a threat to ecosystem health on a global scale, and is now being addressed by an international agreement, the Minamata Convention. Comprehensive knowledge of the details of the atmospheric Hg cycle is still lacking, and in particular there is some uncertainty regarding the atmospherically relevant reduction-oxidation reactions of mercury and its compounds. The exchange of Hg and its compounds between the atmosphere and the oceans also plays an important role in the cycling of mercury in the environment: understanding and quantifying mercury deposition patterns and fluxes is critically important for the assessment of the present, and future, environmental impact of mercury contamination. ECHMERIT is a global on-line chemical transport model, based on the ECHAM5 global circulation model, with a highly customisable chemistry mechanism designed to facilitate the investiga-

tion of both aqueous and gas phase atmospheric mercury chemistry. An improved version of the model which includes a new set of emissions routines, both on-line and off-line, has been developed and used for this thesis to investigate and assess a number of the uncertainties related to the Hg atmospheric cycle. Outputs of multi-year model simulations have been used to validate the model and to estimate emissions from oceans. Various redox mechanisms have been included to assess how chemical reactions influence the models ability to reproduce measured Hg concentrations and deposition flux patterns. To characterize the Hg emissions which result from Biomass Burning , three recent biomass burning inventories (FINNv1.0, GFEDv3.1 and GFASv1.0) were included in the model and used to investigate the annual variation of Hg. The differences in the geographical distribution and magnitude of the resulting Hg deposition fluxes, hence the uncertainty associated with this Hg source, were quantified. The roles of the Hg/CO enhancement ratio, the emission plume injection height, the $Hg^{\circ}_{(g)}$ oxidation mechanism and lifetime, and the inventory chosen, as well as their uncertainty were considered. The greatest uncertainties in the total deposition of Hg due to fires were found to be associated with the Hg/CO enhancement ratio and the emission inventory employed. Deposition flux distributions proved to be more sensitive to the emission inventory and the oxidation mechanism chosen, than all the other model parameters. Over 75% of Hg emitted from biomass burning is deposited to the world's oceans, with the highest fluxes predicted in the North Atlantic and the highest total deposition in the North Pacific. The net effect of biomass burning is to liberate Hg from lower latitudes and disperse it towards higher latitudes where it

is eventually deposited. Finally, the model was used to evaluate the fate of the Hg released into the atmosphere by human activities. Anthropogenic emissions are estimated to amount to roughly 2000Mg/y (1000-4000 Mg/y). Hg speciation (elemental, oxidised or associated with particulate matter) is subject to many uncertainties: the extremely variable lifetimes among Hg species, as well as the Hg emission heights, in combination with the complex physical and chemical mechanisms that drive its final fall-out lead to considerable uncertainties. To address this specific issue three anthropogenic Hg emission inventories, namely AMAP-UNEP, EDGAR and Streets, were included in the Model. Different model parametrisations were adopted to trace the fate of Hg to its final receptors and to thoroughly test the model performance against the measurements. Primary anthropogenic Hg contributes up to 40% of the present day Hg deposition. The oxidation mechanism has a significant impact on the geographical distribution of the deposition of Hg emitted from human activities globally, : 63% is deposited to the world's oceans. The results presented in this thesis provide a new and unique picture of the global cycle of mercury, evaluating and assessing the uncertainties related to many aspects with an on-line Global Circulation Model developed specifically to investigate the global atmospheric Hg cycle.

Sin dall'antichità, le attività umane hanno alterato il naturale ciclo del Mercurio attraverso il suo rilascio incontrollato nell'ambiente. Il Mercurio è un inquinante a diffusione globale in quanto la sua forma atmosferica predominante, detta Mercurio elementare, interagisce molto lentamente con i principali ossidanti presenti in atmosfera, e può essere quindi trasportato molto lontano dalle sorgenti di emissione. Comunque, il Mercurio, in seguito alla sua ossidazione, viene rapidamente depositato e può essere convertito in monometilmercurio (MeHg) sia nel suolo che nelle acque. Il monometilmercurio è in grado di accumularsi nei tessuti biologici, biomagnificandosi all'interno della catena alimentare fino a raggiungere livelli pericolosi per la salute umana. L'inquinamento da Mercurio è quindi una minaccia alla salute degli ecosistemi su scala planetaria, e, per tal motivo, è stato di recente oggeto di un accordo internazionale, noto come Convenzione di Minamata. La conoscenza dei dettagli riguardanti le fasi del ciclo del mercurio in atmosfera è molto lontana dall'essere completa. In particolare le incertezze riguardano le reazioni di ossido-riduzione a cui vannno incontro in atmosfera il mercurio e i suoi composti. Lo scambio del mercurio all'interfaccia atmofera-oceano è un altro elemento chiave nel ciclo del mercurio: la comprensione e la quantificazione di questi processi di scambio sono critici per una corretta valutazione dell'impatto sull'ambiente della contaminazione da mercurio.

ECHMERIT è un modello globale numerico di tipo on-line per lo studio del trasporto e della chimica, basato sul modello di circolazione globale ECHAM5. Dispone di un meccanismo chimico altamente personalizzabile e progettato per lo studio della chimica del mercurio in atmosfera sia nella fase gas che in quella

acquosa.

Per questo lavoro di tesi è stata sviluppata una versione migliorata del modello, che include un nuovo set di routine per la gestione delle emissioni, sia calcolate dinamicamente nel modello, sia importate off-line da campi esterni. Il modello così modificato è stato utilizzato per lo studio e per la valutazione delle incertezze relative alle diverse fasi del ciclo atmosferico del mercurio. I risultati ottenuti da simulazioni di diversi anni sono stati usati preliminarmente per validare il modello e per stimare le emissioni di mercurio dagli oceani. E' stato inoltre valutato l'impatto di diversi meccanismi chimici sulla capacità del modello di riprodurre i livelli di concentrazione e di deposizione di mercurio misurati. Per caratterizzare le emissioni di mercurio dalla cosiddetta combustione di biomassa (Biomass Burning), sono stati inclusi nel modello tre inventari recenti per questo tipo di emissioni (FINNv1.0, GFEDv3.1 e GFASv1.0). Si è quindi studiata la variazione annuale delle emissioni di mercurio dai fuochi, oltre alla distrubuzione geografica delle deposizioni risultanti. E' stato inoltre valutato il ruolo dei rapporti di arricchimento Hg/Co, l'altezza del plume delle emissioni, i meccanismi di ossidazione e i tempi di residenza in atmosfera del mercurio elementale, l'inventario utilizzato e caratterizzata l'incertezza di ciascuno di questi elementi. La più grossa fonte di incertezza sull'entità delle deposizioni di mercurio emesso dai fuochi è stata trovata essere associata al raporto di arricchimento Hg/CO e all'inventario utilizzato. La distribuzione dei flussi di deposizione è stata provata essere più sensibile all'inventario e al meccanismo di ossido-riduzione adottato, che a tutte le altre parametrizzazioni adottate. Più del 75% del mercurio rilasciato dai fuochi viene

depositato sugli oceani. Il più alto flusso è stato simulato nell'Atlantico del nord, mentre la deposizione totale più alta nel Nord Pacifico. L'effeto netto della combustione di biomassa è risultato quello di liberare mercurio dalle basse latitudini e di disperderlo nelle alte, dove eventualmente si deposita. Infine, il modello è stato utilizzato per valutare il destino del mercurio rilasciato in atmosfera dalle attività antropogeniche. Le emissioni antropogeniche si stima ammontino grossolanamente a circa 2000 Mg/a (con un margine che va da 1000 a 4000 Mg/a). Anche la speciazione delle emissioni, ovvero la forma in cui viene emesso (mercurio elementare, ossidato o associato a particolato) è incerta: la grande differenza nei tempi di residenza in atmosfera delle diverse specie di mercurio, così come l'altezza del rilascio delle emissioni in combinazione con i complessi e misconosciuti processi fisici e di trasformazione che guidano laricaduta finale del mercurio genera un'incertezza ancora maggiore riguardo i recettori finali. Per valutare specificatamente queste problematiche, son stati inclusi nel modello tre inventari per le emissioni antropogeniche di mercurio, AMAP-UNEP, EDGAR and Street. Sono state quindi adottate diverse parametrizzazioni per seguire la destinazione finale del mercurio e per valutare le performance del modello in termni di confronto con le misure disponibili. Le emissioni antropogeniche primarie di mercurio contribuiscono fino al 40% delle deposizioni locali and the 63% of mercury emitted is deposited to oceans. I risultati presentati in questa tesi forniscono una vista unica sul ciclo del mercurio in atmosfera, in quanto permettono di valutare le incertezze di molti aspetti con un modello di Circolazione generale globale di tipo on-line sviluppato appositamente per lo studio del ciclo atmosferico del Mercurio.

Contents

Author List

De Simone Francesco

Listing of figures

To my son.

Acknowledgments

I'm investigating things that begin with the letter M.

The Mad Hatter, from Alice in Wonderland (2010)

1 Introduction

The Earth's atmosphere is a mixture a of a number of gases, each with its own proprieties, that encircle our planet. It consists of about 78 percent nitrogen and about 21 percent oxygen. The remaining one-percent contains all the other gases including carbon monoxide, carbon dioxide, ozone, methane, ammonia along with a wide variety of trace chemical compounds. Air pollution occurs when one or more of these elements or compounds reach harmful concentrations. That is, concentrations which could be harmful to the health or comfort of humans and animals or which could cause damage to plants and materials. The substances that cause air pollution are collectively called pollutants and are emitted at any moment by such natural occurrences as volcanic eruptions, forest fires, decaying vegetation as well as by human activities. Air pollution is nothing new. In medieval England, where the burning of coal was the primary method people had for heating, the black smoke from chimneys caused many problems. This pushed the King, in

1306, to regulate the use of coal. Although these efforts failed to solve the problem, historically, they represent the first set of air pollution ordinances in attempt to clean the air [124]. While the problem of air pollution has existed for centuries, the present day industrial boom and population explosion have made it critical and only during the past few decades have we begun to understand that air is a resource that has to be managed for health and environmental quality.

1.1 Hg Air pollution

Mercury (Hg) and particularly methylmercury compounds (MeHg) are extremely toxic and represents a threat to the environment and ecosystems, and also for human health. Mercury is a natural element and is found throughout the world. The natural sources of Hg are many and background environmental levels have been present since long before the human race appeared. Hg is contained in many minerals, including cinnabar (HgS), an ore mined to produce Hg, however much of the present day demand for Hg is met by recovery Hg from industrial sources. Hg is also present as an impurity in many other minerals, such as gold and non-ferrous metal ores, and also fossil fuels, particularly coal. Human activities, mining and the burning of coal have increased the release of Hg into the environment, raising its burden in all environmnetal compartments: atmosphere, soils, fresh waters, and oceans. The majority of these human Hg emissions have occurred since the industrial revolution in 1800 and are continuing with fossil-fuel-based energy generation powering industrial and economic growth in South and South-East Asia [79, 110, 121] (See Figure 1.1.1).

Even now, Hg is commonplace in daily life. Electrical and electronic devices, switches (including thermostats) and relays, measuring and control equipment, energy-efficient fluorescent light bulbs, batteries, mascara, skin-lightening creams and other cosmetics which contain Hg compounds, dental fillings and a host of other consumables are used across the globe. Food products obtained from fish, terrestrial mammals and other products such as rice can also contain Hg. It is still

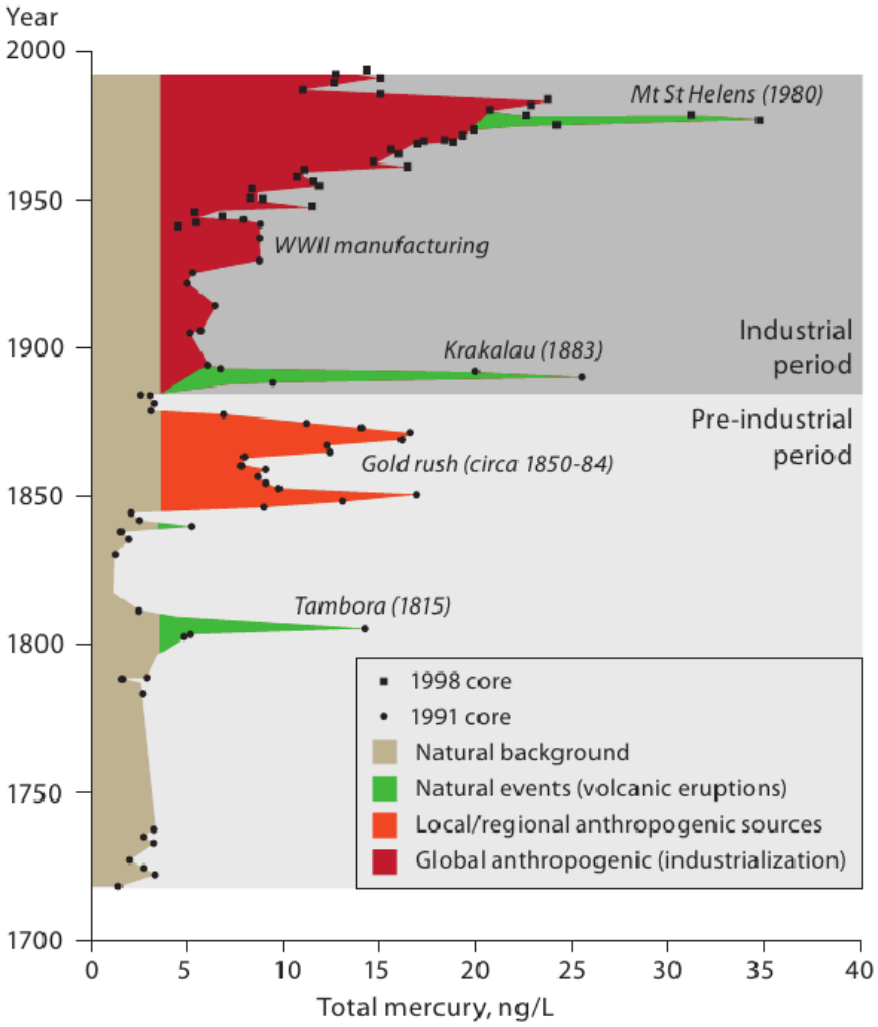

Figure 1.1.1: Ice core record of Hg deposition Upper Fremont Glacier. Image from [122].

widely used in health care equipment, where it is used in measurement equipment such as in sphygmomanometers (to measure blood pressure) and thermometers, although their use is declining.

1.1.1 Hg Emissions and Remedies

Hg is emitted in the atmosphere from a variety of sources, as illustrated in Figure 1.1.2. Estimates of natural emissions are in the range of 4000 to 7000 Mg yr−1 [121]. Natural sources include crustal degassing, volcanoes, the re-emission of previously deposited Hg from soils and aquatic surfaces, weathering processes of the Earth's crust and forest fires [78]. Contributions from natural sources and processes vary geographically and temporally depending on a number of factors including meteorological conditions, the presence of volcanic or geothermal activity, the presence of Hg and also the occurrence of forest fires [37, 78]. The two major source categories include those related to the geological presence of Hg in various minerals and evasion of Hg from aquatic and terrestrial ecosystems. This latter is related to the historical atmospheric deposition of Hg to these ecosystems, that originally was emitted by both natural and anthropogenic sources. Therefore it is not simple to distinguish between the emission of 'legacy' Hg and Hg emitted form natural sources.

Global emissions of Hg to the atmosphere in 2010 from human activities were estimated at 1,960 tonnes and appear to have been relatively stable from 1990 to 2010 [122]. Globally more than half of the Hg from anthropogenic sources is emitted as GEM, or Hg^0, while only 10% of emissions occur as PBM, or Hg^p. The rest of the Hg is emitted as GOM, or Hg^{II} [122]

The largest anthropogenic sources are associated with artisanal and small-scale gold mining (ASGM) and coal burning, and together contribute about 61% of annual anthropogenic emissions to the atmosphere. Other major contributors include ferrous and non-ferrous metal production and cement production, together responsible for 27% (See Figure 1.1.3).

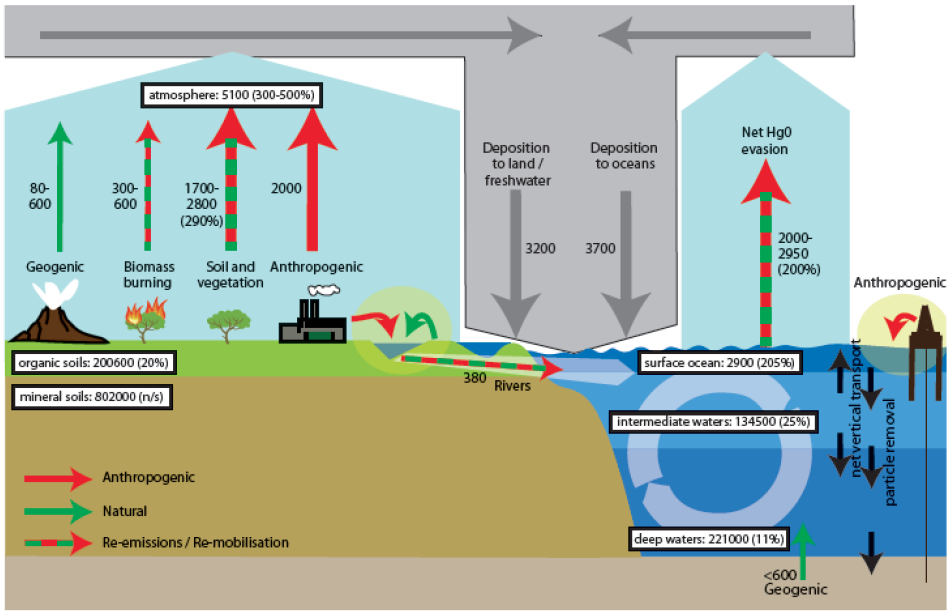

Figure 1.1.2: Global Hg budget illustrating the natural and anthropogenic emissions sources and the cycle between the main environmental compartments. Image from UNEP [121].

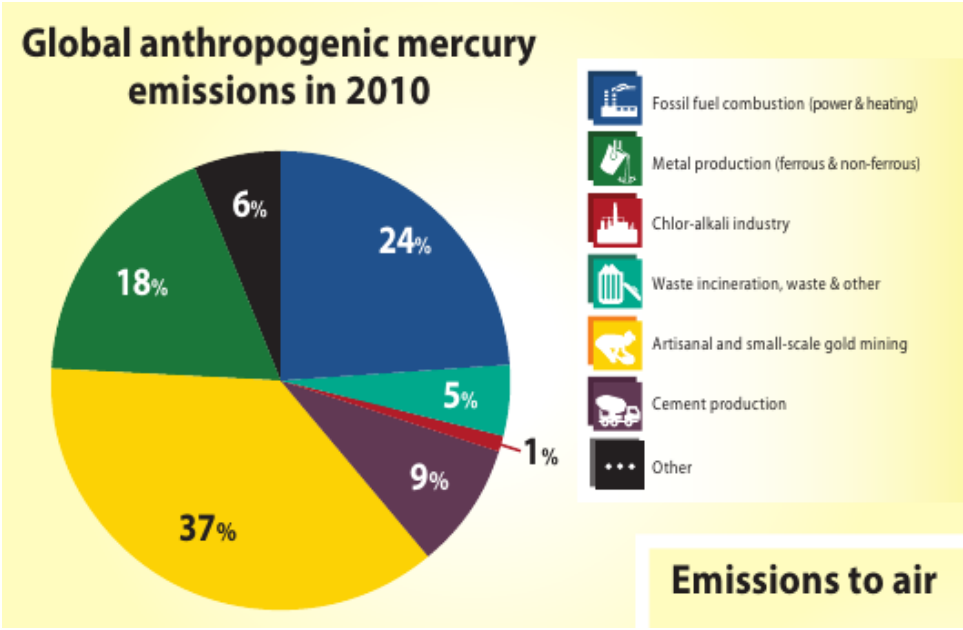

Figure 1.1.3: Global anthropogenic Hg emissions in 2010. Image from UNEP [121].

Hg residues from mining and industrial processing, as well as Hg in waste, have resulted in a large number of contaminated sites all over the world. Most Hg contaminated sites are concentrated in the industrial areas of North America, Europe and Asia; and in sub-Saharan Africa and South America.

Air pollution control technologies in industrial facilities remove Hg that would otherwise be emitted to the air. Although there is little information about the ultimate fate of the Hg captured in this way, it is likely that these control technologies will reduce the amount of Hg that is transported globally by the atmosphere. For many health care applications and for pharmaceuticals there are safe and cost-effective replacements for Hg, and the goal to reduce demand for Hg-containing fever thermometers and blood pressure devices by at least 70% by 2017 has been set[121].

However while the atmosphere responds relatively quickly to changes in Hg emissions, the large reservoirs of Hg in soils and oceans mean that there will be

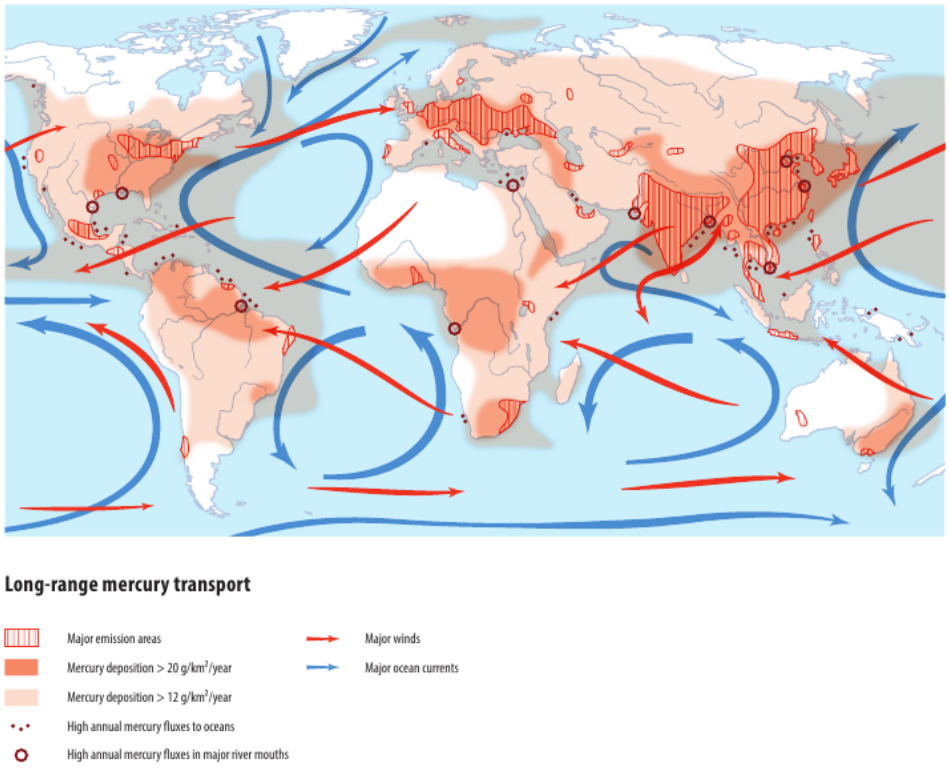

Figure 1.1.4: Long-range Hg transport. Image from [121].

a long time lag (on the order of years to decades [11]) before reductions in Hg inputs are reflected in depleted concentrations in these media and in the wildlife taking up Hg from them. Therefore it is necessary to act now to reduce ecosystem exposure to Hg in next decades [121].

1.1.2 Effects on Human Health

Differently from other pollutants that are restricted in their range and in the size and number of the populations they affect, wherever Hg is mined, used or discarded, it is liable to finish up thousands of kilometres away because of its lifetime in the atmosphere and oceans[11, 121] (See Figure 1.1.4).

Hg is bioaccumaulated as it rises up the food chain, reaching its highest level in

predator fish such as swordfish and shark that may be consumed by humans. There can also be serious impacts on ecosystems, including reproductive effects on birds and predatory mammals. High exposure to Hg is a serious risk to human health and to the environment [121]. Atmospheric emissions of Hg are highly mobile globally, while aquatic releases of Hg are more localised. Hg in water becomes more biologically hazardous when it is methylated and enters the food chain, although some is eventually reduced to Hg^{o} and evades to the atmosphere. Equally in soils and sediments, Hg can be methylated, largely through metabolism by bacteria or other microbes, and can enter the food chain and ultimately be of concern to human health [121]. Hg can seriously harm human health, and is a particular threat to the development of foetuses and young children. It affects humans in several ways. At very high air concentrations Hg vapour is rapidly absorbed into the blood stream when inhaled. It damages the central nervous system, thyroid, kidneys, lungs, immune system, eyes, gums and skin. Neurological and behavioural disorders may be signs of Hg contamination, with symptoms including tremors, insomnia, memory loss, neuromuscular effects, headaches, and cognitive and motor dysfunction. In the young it can cause neurological damage resulting in symptoms such as mental retardation, seizures, vision and hearing loss, delayed development, language disorders and memory loss [121].

People may be at risk of inhaling Hg vapour from their work (in industry or ASGM), or in spills, and may be at risk through extended direct contact of Hg with the skin. The most common form of direct exposure for humans, however, is through consuming fish and sea food contaminated with methylmercury. Once ingested, 95 per cent of the chemical is absorbed in the body [121].

A continuous release of the toxic methylmercury in the industrial waste water from the Chisso Corporation's chemical factory from 1932 to 1968 was the cause of the greatest local Hg poisoning event in the history. The so called Minamata disease was first discovered in Minamata city in Kumamoto prefecture, Japan, in 1956. Symptoms included numbness in the hands and feet, general muscle weakness, narrowing of the field of vision, and damage to hearing and speech (EINAP). In extreme cases, insanity, paralysis, coma and death have been known to ensue

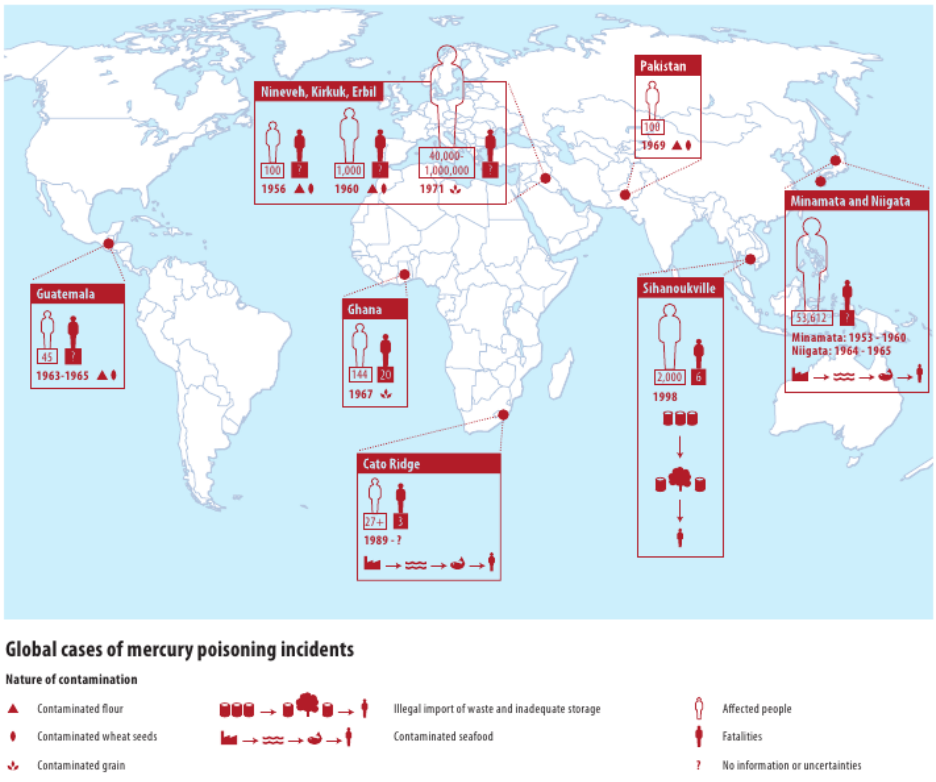

Figure 1.1.5: Global cases of Hg poisoning incidents. Image from [121].

rapidly. As of March 2001, 2,265 victims had been officially recognised as having Minamata disease (1,784 of whom had died) [1]. Unfortunately, this is only one example of the poisoning events which have occurred. Figure 1.1.5 summarizes the global cases of Hg poisoning incidents [121].

Hg pollution is therefore a threat to ecosystem health on a global scale, and is now being addressed as such following the negotiations to produce an international agreement, known as the Minamata Convention [121].

[1] http://www.env.go.jp/en/chemi/hs/minamata2002/ch2.html

1.2 Modelling Issues

Due to the ubiquitous presence of Hg in the atmosphere, numerical chemical transport models represent a useful tool for investigate the Hg pollution in conjunction with existing monitoring networks (CAMNet, Canada [2] MDN, USA [3], AMNet, USA [39], EMEP, Europe [4], GMOS, global [5]). The application of chemical transport models can supplement direct measurements providing information on the sources, processes and fate of Hg and allowing the investigation of the uncertainties regarding individual processes in the global Hg cycle.

Modelling the global spread and fate of Hg is a challenging task: it requires extensive treatment of multiple species that exist in different phases in the atmosphere with distinct physical and chemical properties. Moreover our current knowledge is far from complete, and some peculiar Hg characteristics, like the so called "prompt recycling" of deposited Hg [99], make the task even more complicated. The uncertainties are rather numerous and arise from many sources, including but not limited to: inaccuracies in existing chemical kinetic parameters, inadequate representation of chemical processes and of Hg species, a lack of detailed Hg chemical speciation in field studies, inaccuracies in Hg transport and deposition mechanisms and emission inventories [62, 113], lack of field studies and incomplete knowledge about exchange processes, and also the Enhancement Ratios used in Fire Emissions Inventories [29]. The interactions between different Hg species and the atmospheric media as well as the processes which are involved are also challenging to model and to CONSTRAIN, since they can vary at different temporal and spatial scales. Global models were designed and developed to study the global Hg atmospheric cycle and generally are applied for long-term simulations. Their coarse spatial resolution (on the order of hundreds of kilometers) make them useful for monthly/seasonal analysis and for the assessment of uncertainties related to Hg cycle at global scale. An indispensable application of global

[2] https://www.ec.gc.ca/natchem/default.asp?lang=en&n=4285446C-1
[3] http://nadp.sws.uiuc.edu/MDN/
[4] http://emep.int/index.html)
[5] http://www.gmos.eu/

models is to provide the Boundary and the Initial Conditions (BC/IC) to regional Hg models which perform simulations at higher spatial and temporal resolutions. A regional CTM is a type of numerical model which typically simulates atmospheric chemistry, atmospheric dispersion and trans-boundary transport within a continent or a particular region, with spatial resolution ranging from 1 to 100 km. These models are usually applied for the simulations of Hg dispersion over areas containing numerous emission sourceS, where IT is necessary to obtain a very high level of detail. The primary strengths of these models are the detailed treatment of Planetary Boundary Layer (PBL) processes and relatively high spatial resolutions. Another important distinction exists between off-line and on-line models. Off-line models are based on the assumption that chemical and physical processes in the atmosphere can be considered independent without loosing accuracy. Such models use the output of meteorological models, generally available at different spatial and temporal resolutions, to drive the transport of chemical species. The methodology of off-line models has some computational advantages, but leads to a potential loss of information about atmospheric processes due to the interpolation of meteorological fields both in space and time. Moreover in these model it is not possible to consider the two way feedback between chemistry and physics. On-line models differ from their off-line counterparts in the way that chemistry is calculated on-line during the simulation of physical processes. In this way it is possible to reproduce the actual strong coupling between meteorological and chemical processes in atmosphere. On-line models have disadvantages in their higher computational demands, but the growing availability of powerful computational resources nowadays make their use more feasible in terms of computation time.

Much of the content of this chapter appeared in [28]

2

The Mercury Chemical Transport Model ECHMERIT

ECHMERIT differs from almost all other global Hg models in that it is an on-line model. The concentration of atmospheric chemical species at a given place and time are determined both by chemical and transport phenomena. An on-line model calculates the concentration of a chemical species in a model cell at each time step considering its production and loss, as a result of chemical reactions, (and if appropriate emission and deposition), but also due to transport in and out of the cell. Off-line models, which use the output of meteorological models as input, differ in that the meteorological variables required to calculate the changes in concentration, which result from transport phenomena must be interpolated in time, and often in space, potentially leading to inaccuracies. In many instances

the parametrisation of the physical processes in the numerical weather prediction model and the chemical transport are different. This can give rise to inconsistencies in the model. Both of these problems are avoided using on-line models. However on-line model simulations are significantly more computationally expensive than off-line simulations. Recent advances in computing power have now made on-line simulations much more feasible.

2.1 Existing Models and Application

A number of off-line chemical transport models (CTMs) have been developed in recent years, they include GEOS-Chem-Hg [98, 111], which is still undergoing active development [9, 102], CTM-Hg (Global Chemical Transport Model for Mercury) developed by AER/EPRI [66, 93, 94], GLEMOS (Global EMEP Multimedia Modeling System) [118], and more recently CAM-Chem/Hg [59].

The GRAHM (Global/Regional Atmospheric Heavy Metals) model [27] is an on-line model which has been used in particular to investigate Hg deposition fluxes over North America [138], the sub-Arctic regions [88] and the Arctic itself [33, 42]. One feature of the GRAHM model (and also GLEMOS; above) is that they both use prescribed concentration fields from other CTMs which have detailed tropospheric chemistry routines, in the case of GRAHM output from MOZART [35, 50]. ECHMERIT on the other hand uses a version of the CBM-Z chemical mechanism [137] to which gas and aqueous phase Hg chemistry, and mass transfer between the gas and aqueous phase of soluble species, have been added, as described in section 2.3.

An important application of global models is to provide the boundary and the initial conditions (BC/IC) to regional Hg models which perform simulations at higher spatial resolutions. Regional CTM simulations of atmospheric Hg chemistry and deposition have been shown to be particularly sensitive to the BC/IC which are used [81]. Boundary conditions for regional simulations are generally more important than initial conditions for regional Hg CTMs, and therefore recently most regional models make use of time and space varying BCs from global

model output. However there can be some variation in the regional modelling results depending on which global model output is used [19, 20, 47].

2.2 Model Description

ECHMERIT is an on-line model global Hg model [55] based on the fifth generation Atmospheric General Circulation Model ECHAM5 [84, 85], developed ad maintained at the Max Planck Institute for Meteorology (MPI-M, Hamburg, Germany), which provides the atmospheric component and the routines for the transport of tracers. Different schemes for advection, convection and vertical diffusion are already implemented in the model. In ECHMERIT the semi-Lagrangian advection scheme of [61] and the convective mass transport scheme of [117] and [72] were adopted to ensure mass conservation and to preserve linear correlations. A mass flux correction scheme was also included in ECHMERIT to avoid negative mixing ratios in the case of a strong convective transport gradient [55].

In the full chemistry mode ECHMERIT transports 42 chemical species, including four Hg species: elemental Hg^0, reactive $Hg^{II}_{(g)}$ and $Hg^{II}_{(aq)}$ species, and the inert, insoluble Hg^P. Hg^P is assumed to be solid. It is emitted from anthropogenic activities, is subject to transport and deposition processes and it is not involved in any chemical reactions. $Hg^{II}_{(aq)}$ is a lumped species that includes all aqueous phase oxidised Hg species present in the chemistry mechanism implemented in the model. In grid cells with a liquid water content below a threshold value ($\leq 10^5\ \mu g\, m^{-3}$ [53]), it is assumed that the atmospheric aqueous phase (cloud or fog droplets, rain) have evaporated, and in this case $Hg^{II}_{(aq)}$ is considered to be solid and transported and deposited in the same way as atmospheric aerosol particles. When a grid cell's liquid water content increases above the threshold value, any $Hg^{II}_{(aq)}$ present is assumed to be in the aqueous phase.

The model uses a spectral grid. The horizontal resolution of the model is very flexible ranging from T21 to T159, whereas in the vertical the model is discretised with a hybrid-sigma pressure system with 19 or 31 non-equidistant levels up to 10 hPa. A number of studies have focused on the sensitivity of ECHAM5 to

the vertical and horizontal resolution employed. The results show that ECHAM5 tends to overestimate precipitation over the oceans at the highest vertical resolution [45]. Since the precipitations over oceans plays an important role in the global cycle of the Hg, the simulations described here used 19 vertical levels. A T42 grid (roughly 2.8° by 2.8°) has been used for these simulations, as with L19 vertical resolution, no improvement in simulation results has been found increasing horizontal resolutions to greater than T42 [85] .

To reproduce real meteorological conditions the nudging routine already implemented in ECHAM5 using reanalysis data from the ERA-INTERIM project (ECMWF) has been used. Averaged values obtained from previous multi-year long model simulations are used to initialise the concentrations of all species. A further two year chemical spin-up was performed, before a three-month spin-up to allow meteorological fields to converge using the nudging relaxation algorithms. In this Chapter are presented model simulations results for two years(2008/2009).

2.2.1 Ocean Emissions

Hg emissions from the oceans represent a major source of Hg to the atmosphere [68]. The difference in concentration between Dissolved Gaseous Mercury (DGM) that is Hg^0 dissolved in surface waters and $Hg^0_{(g)}$ generally results in Hg being emitted from the seas, the surface layer is often supersaturated in DGM [15, 102]. The rate of exchange is also determined by factors such as water temperature and wind speed, [129]. However there remain some uncertainties regarding the parametrisation air-sea exchange [129]. In the model, the Hg^0 fluxes are calculated using the two-layer gas exchange model introduced by Liss and Slater [64].

$$F = K_w(C_w - C_a/H(T)) \tag{2.1}$$

where F is the Hg^0 flux, in ng m^{-2} h^{-1}, K_w is the water-side mass transfer coefficient, in m h^{-1}, $H(T)$ is the Henry's Law constant corrected for the temperature, T, and C_w and C_a, both expressed in ng m^{-3}, are the Hg^0 concentrations in seawater and in air, respectively. The water-side mass transfer coefficient K_w was calculated

using the parametrisation of Wanninkhof [128]

$$K_w = 0.31 \times u_{10}^2 (Sc_{Hg}/Sc_{CO_2})^{-0.5} \tag{2.2}$$

where u_{10} is the wind speed at 10 m and Sc_{Hg} and Sc_{CO_2} are the Schmidt numbers of Hg and CO_2, respectively.

The parametrization of Andersson et al. [13] was used to calculate the temperature dependent Henry's law constant:

$$H = exp\left(\frac{-2404.3}{T} + 6.92\right) \tag{2.3}$$

A positive value of F indicates a net Hg flux from the ocean to atmosphere whereas a negative flux would indicate deposition to the ocean. Due to the (generally) supersaturated DGM concentrations, the oceans represent a net source of Hg to the atmosphere. In this study a uniform and constant DGM concentration of 0.1 pM has been assumed. This value is within the range of observations [14, 115]. Results obtained by using in the model this parametrisation are presented in the Section 2.5

2.2.2 Other Emissions

The anthropogenic Hg emission are calculated off-line and included in the model at run-time. The off-line calculation permits to include any anthropogenic Hg emission inventories available. These include the anthropogenic Hg emission inventory from the Arctic Monitoring and Assessment Programme (AMAP/UNEP)[1] for all years available and those included in EDGARv4 [2] [70]. The emissions provided by both inventories are annual, with no seasonal cycle considered. The three height levels (less than 50 meters, between 50 and 150 meters, and more than 150 meters) are available in the emission inventory from AMAP/UNEP, that are mapped to the appropriate model level, whereas no info about height is present in those from EDGAR. In this latter case is possible to include them in the first

[1] http://www.amap.no/mercury-emissions
[2] http://edgar.jrc.ec.europa.eu/edgar_v4tox1/

model level or to use the industrial categorical EMEP model distribution to map the emissions to the relative model levels.

Emissions for the other species included in the model are also derived off-line from the EDGAR/POET emission inventory [43] .

Monthly Hg emissions from Biomass Burning are calculated off-line and included in the model at run-time.The off-line calculation permits to include any inventories, given that the final file format remains the same. Actually it is possible to include the three principal Biomass-Burning inventories available, GFAS, GFED and FINN [1, 56, 125, 130].

The increase in atmospheric Hg concentration resulting from BB were estimated as in Friedli et al. [37], using an Enhancement Ratio (ER), defined as,

$ER = \Delta[Hg]/\Delta[CO]$

where $\Delta[Hg]$ is the sum of all Hg species in excess of background, and $\Delta[CO]$ is the difference between the plume and background CO concentration [37]. The global average ER (ER_{av}), as reported by Friedli et al. [37] to be 1.54×10^{-7}, can be used in all simulations including GFED, GFAS and FINN inventories. For GFED inventory only is also possible to use other two different biome specific sets of ERs, ER_{coarse} and ER_{fine}, calculated as described in A. Emissions from soils and vegetation were calcualted off-line and derived from the EDGAR/POET emission inventory [43, 77] that includes biogenic emissions from the GEIA inventories [3], as described in Jung et al. [55]. Monthly Hg emissions from fires are mapped to the biomass burning CO emissions in the EDGAR/POET inventory. So called prompt recycling of deposited Hg [99] is used in the model, 20% of wet and dry deposited Hg is re-emitted to the atmosphere as Hg^0 if the deposition occurs over land. This percentage is increased to 60% for snow covered land, icesheets and ice covered seas, (using the on-line snow cover from ECHAM5).

[3] http://www.geiacenter.org

2.2.3 Deposition

The dry deposition scheme, follows the approach of [57] as described in Jung et al. [55]. For the Hg^0 dry deposition, due the uncertainties in quantifying the deposition velocities of Hg^0 over different canopies [139], we further included a maximum allowed velocity of 0.03 cm/s, equal to the annual mean Hg^0 deposition velocity from Selin et al. [99]. Wet deposition is applied only to the transported chemical species with high solubility (i.e. with a Henry's Law constant greater than 100 $M\,atm^{-1}$), considering both below-cloud and in-cloud scavenging. The concentration and solubility of the species, total rainfall intensity, cloud water content, radius and velocity of the rain droplets are taken into account, as in Seinfeld and Pandis [95].

2.3 Chemistry

Until recently most models assumed the hydroxyl radical (OH) and ozone (O_3) were the main oxidants of Hg^0 in the gaseous phase, although the exact kinetics are still in debate [51].

Under atmospheric conditions it seems that the oxidation rate of Hg^0 by OH is actually slower than reported by laboratory kinetic study due the rapid thermal dissociation of HgOH [21, 40]. Moreover ozone as the only oxidant does not explain some observed patterns in both Hg concentrations and deposition [48, 98, 107].

More recently Br atoms have been proposed as the dominant global oxidant of the Hg^0 in the gas phase, explaining mercury depletion events (MDEs) in polar areas [40, 133] as well as the pattern of Hg^{II} in the MBL [48]. Reactions with Br have been included in a number of modelling studies[34, 49, 59] showing a good agreement with observations. Reactions with Bromine is included in the chemical mechanism since the first version of ECHMERIT, and the model requires a Br/BrO climatology, or to import external fields from oher models, like p-TOMCAT [134, 135], in order to activate the Bromine chemistry. The aqueous-phase reduction of Hg^{II} was observed by [76] although its atmospheric relevance

is still uncertain [38, 81]. Whether Hg^{II} in the gas phase can be reduced by CO or SO_2 has also been discussed [65, 81] The nitrate radical, NO_3 is important atmospheric oxidant during the night. There has been only a single study in the literature that have measured the kinetic of the reaction between NO_3 and Hg^0 studied by using a discharge flow technique [105]. This reaction has been included in the chemical mechanism only for sensitivity purpose and to compare the results with mechanisms which only include daytime oxidation, in fact the authors of this study acknowledged that the obtained constant rate (4.0×10^{-15} cm^3 $molec^{-1}$ s^{-1} should be taken as an upper limit for the reaction, since at typical nitrate radical atmospheric concentration the lifetime of Hg^0 would be in orders of days.

As concluded by Subir et al. [113] our relatively poor understanding of these reactions and the atmospheric Hg oxidation mechanisms, means that more work is needed in this field to understand better the global cycle of the Hg in the atmosphere.

2.3.1 Chemistry Modules

The Chemistry module is the core of ECHMERIT model and distinguish it from ECHAM5, that does not include any chemistry explicit module in the base version. Some extended versions of ECHAM include chemistry, like ECHAM-HAMMOZ [82], but the relative module it is not very easy to change. ECHMERIT instead uses a flexible and higly customizable Hg chemistry module. The ECHMERIT base chemistry module includes a gas phase photochemical mechanism, derived from the CBM-Z mechanism [137], and a tropospheric aqueous phase mechanism, which is based on the aqueous phase chemistry in the MECCA model [86]. It also includes the exchange of soluble compounds between gas and aqueous phases as a forward and backward reaction following the mass transfer approach of Schwartz [92]. The chemistry module was prepared using the version 2.2 of the Kinetic Pre-Processor (KPP) [26] and the SEULEX integration method [87] to solve the stiff chemical ODE system. Since only tropospheric chemistry is included in the model, the calculation of atmospheric chemistry is restricted to the model lay-

ers within the troposphere.The O_3 mixing ratios in the stratospheric model layers come directly from the climatology already implemented in ECHAM5 [55]. The complete module included 121 species involved in almost 300 reactions, the Hg chemistry has been described in full in Jung et al. [55].

To reduce the computational demands of the chemistry routine, a simplified variant of the original ECHMERIT full chemistry is also available. In this simplified version the reactant concentration fields were imported off-line and only reactions involving Hg species are included, reducing the computation-time required by solving chemistry equations (See Section 3.1.3).

It is also possible to run ECHMERIT simulations with a simple fixed-lifetime (against oxidation) tracer assumption for atmospheric Hg^0. Since in this configuration the "oxidation" of Hg^0 to Hg^{II}_g is temporally and spatially invariant it has been labelled the pseudo-oxidation mode. In this mode, the model included only the three emitted Hg species, Hg^0, Hg^{II} and Hg^P. At each time step of the model a fraction of Hg^0 present in a given model cell is assumed to "decay":

$$[Hg^0]_{t+t_{step}} = [Hg^0]_t \times \exp \frac{-t_{step}}{\tau} \tag{2.4}$$

where $[Hg^0]_t$ and $[Hg^0]_{t+t_{step}}$ are the concentrations at the beginning and at the end of time step of Hg^0, and t_{step} and τ are the time step length and the decay time of Hg^0 respectively. Each decayed Hg^0 atom is assumed to be converted in Hg^{II}_g. The 12-month lifetime runs were found to reproduce better the latitudinal profile of Hg concentrations and gave more similar results to the full chemistry simulations [28]. This simulation mode has also been used to investigate the Hg mass balance in the Mediterranean Basin [136].

2.3.2 Chemical Mechanisms

To study the impact of different reactions and oxidants on the global atmospheric cycle of the Hg, some variations on the original ECHMERIT chemistry mechanism have been implemented and assessed. The base mechanism includes Hg^0 oxidation by OH and O_3 in the gas and aqueous phases and reduction of Hg^{II}_{aq} by

Table 2.3.1: Red-ox reactions included in the mechanisms.

Model	Red-ox reactions
Base	$O_3 + OH + HO_{2(aq)}$
Base2	$O_3 + OH + NO_3 + HO_{2(aq)}$
Base3	$O_3 + OH + NO_3$
Base4	$O_3 + NO_3$

$HO_{2(aq)}$ in the aqueous phase. Further simulations were run in which NO_3 oxidation was added to the base mechanism (Base2 model). In a further simulation aqueous phase reduction was removed (Base3 model), and in the remaining simulation both the gas phase oxidation by OH and the aqueous phase $HO_{2(aq)}$ reduction were also removed (Base4 model). Table 2.3.1 summarizes the red-ox reactions included in the different models.

2.4 Surface Hg distribution

The modelled surface layer TGM concentration, averaged over the two year simulation period (2008-2009), is shown in figure 2.4.1. The figure shows the four variations of the chemical mechanism which were employed. The latitudinal variation of surface TGM is shown in figure 2.4.2 which shows the results from the different redox combinations and also includes the results from the 8 and 12-month lifetime tracer experiments. The model reproduces the observed surface TGM concentration gradient ($>$20%) between the Northern and Southern Hemisphere, independently of the chemical mechanism or the decay time adopted. This is an improvement on the previous version of the model, and is due to the revised treatment of oceanic emissions compared toJung et al. [55]. It is clear from figures 2.4.1 and 2.4.2 that only the Base mechanism reproduces the typical mean background concentration values of TGM of around 1.1 - 1.3 ng m^{-3} in the Southern and of 1.5 - 1.7 ng m^{-3} in the Northern hemisphere [63]. Of the tracer simulations the 12-

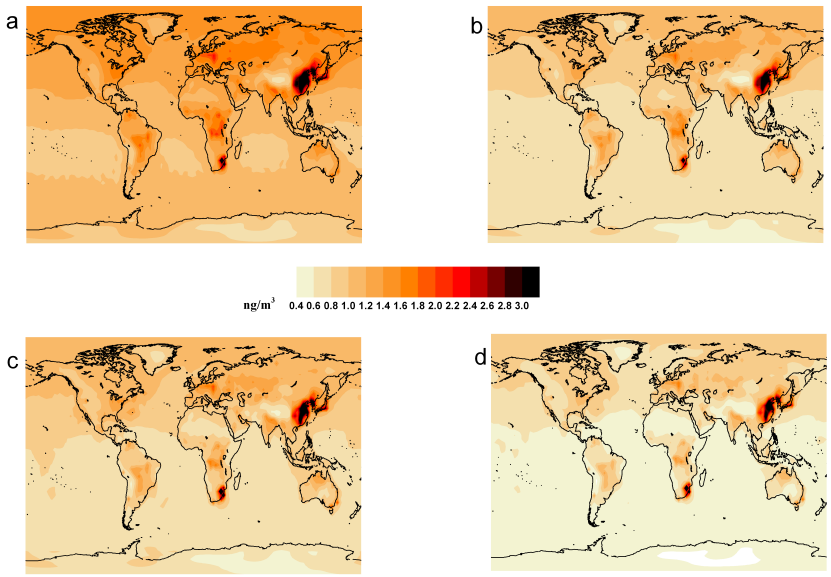

Figure 2.4.1: Geographical distribution of Total Gaseous mercury (TGM) surface concentration (ng/m^3) as resulted by using different full chemistry mechanism: a) Base, b) Base2, c) Base4, d) Base3. Model values are annually averaged for the simulation period (2008-2009).

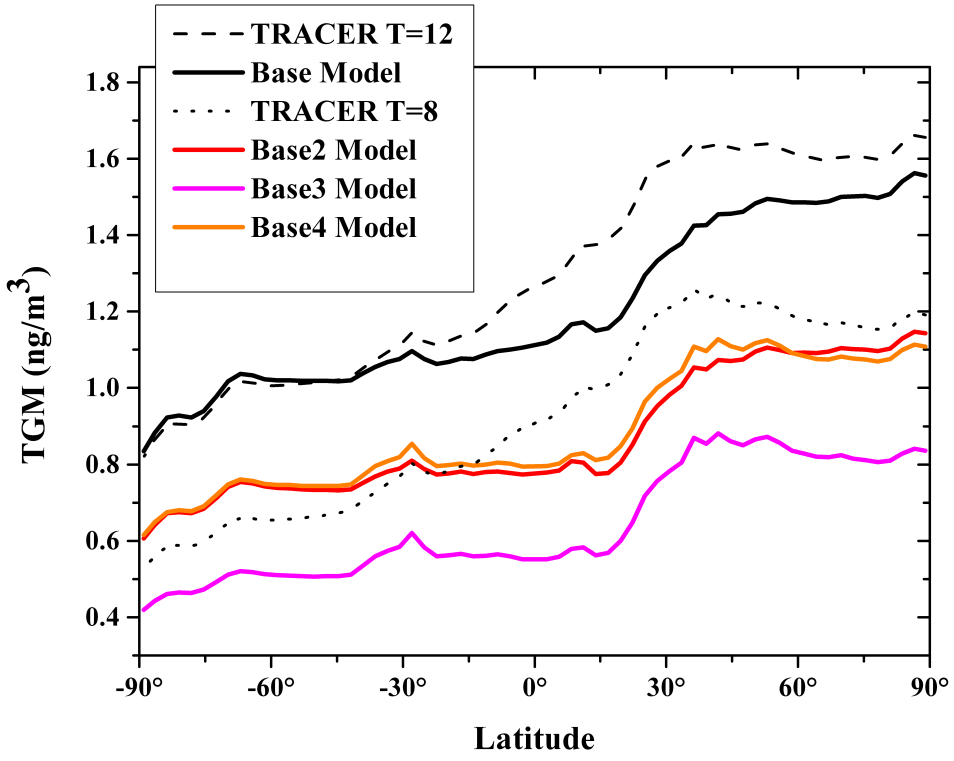

Figure 2.4.2: Hemispherical gradient of total gaseous mercury (TGM) as resulted by using different full chemistry mechanism. Model data are averaged longitudinally for the 2008-2009 simulated period.

month lifetime simulation comes closest to reproducing the observed TGM values and variation. The addition of Hg oxidation by NO_3 lowers the TGM surface concentrations significantly at all latitudes, and the values of around 0.7 ng m^{-3} in the Southern and of 1.1 ng m^{-3} in the Northern hemisphere are not realistic. These values are comparable with the concentrations obtained from the 8-month lifetime tracer experiment.

The simulation Base4 with no gas phase OH oxidation and no aqueous phase reduction, with oxidation by O_3 + NO_3 shows very similar surface concentrations to the Base2 model. As the Base2 simulation includes the reactions with OH and HO_2 in addition to those with O_3 + NO_3, it appears that the OH and HO_2 reactions have roughly equal but opposite effects on the TGM concentration. However this effect will vary with time and location as the distributions of OH and HO_2 differ over space and time.

The form of the latitudinal variation (figure 2.4.2) obtained in the tracer experiment simulations is quite different from those obtained using the model's chemistry mechanisms due to the fact that the "decay" of Hg^0 to Hg^{II} is assumed to be both temporally and geographically uniform, which is not a true reflection of the actual distribution of atmospheric oxidants. Figure 2.4.3 shows the average latitudinal distribution of the Hg^0 surface concentrations, and the 1^{st} to 99^{th} percentile range(shaded area) of modelled value at each latitude. The Base model annual average was compared with the annual average Hg^0 surface observations from 35 global sites. Observation data include those published in [119] plus additional data collected by sites belonging to EMEP programme. Where it was possible averages for the same years as the simulations were used (circles in figure 2.4.3), the other data shown (crosses) was collected over the period between 1995-2009. Figure 2.4.4 (top panel) reports the geographical distribution of the same observations and model data. The model reproduces the spatial distribution of the Hg^0 observations,with the peak model variability in the Northern Hemisphere matched by the peak in the range of the observations. The high variability of TGM con-

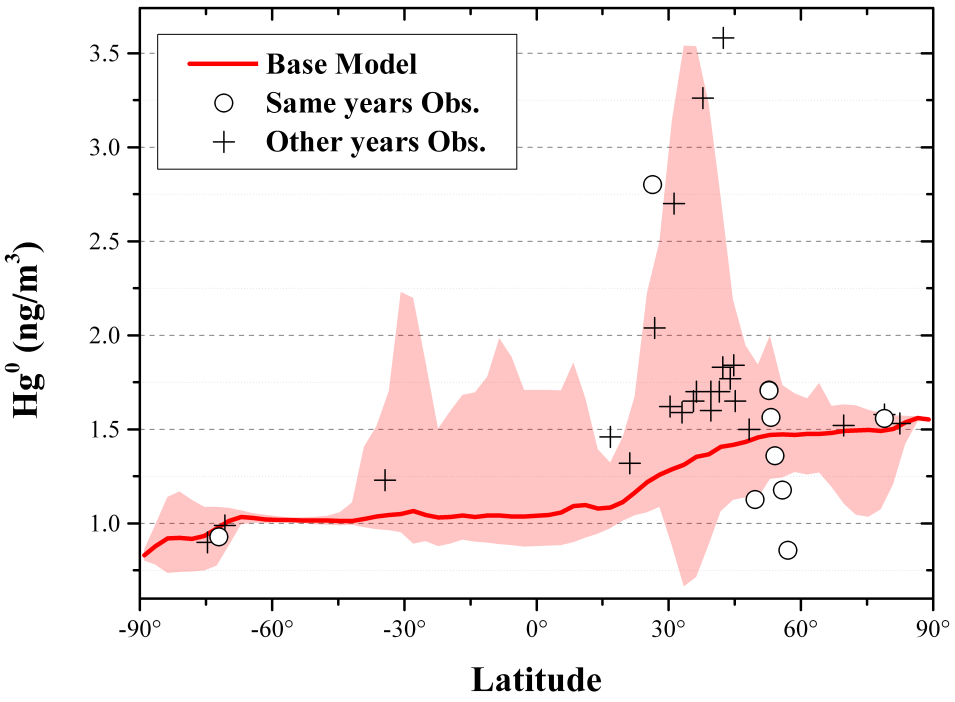

Figure 2.4.3: Averaged latitudinal distribution of air concentrations of Hg^0 as simulated by base Model. Red shadowed area represents the 1^{st} to 99^{th} percentile range of the longitudinal variation. Annually averaged measurements are also reported: circles indicates measurements collected during the same years of the simulation period. Observations include those used by [119] plus additional sites in Europe belonging to EMEP programme

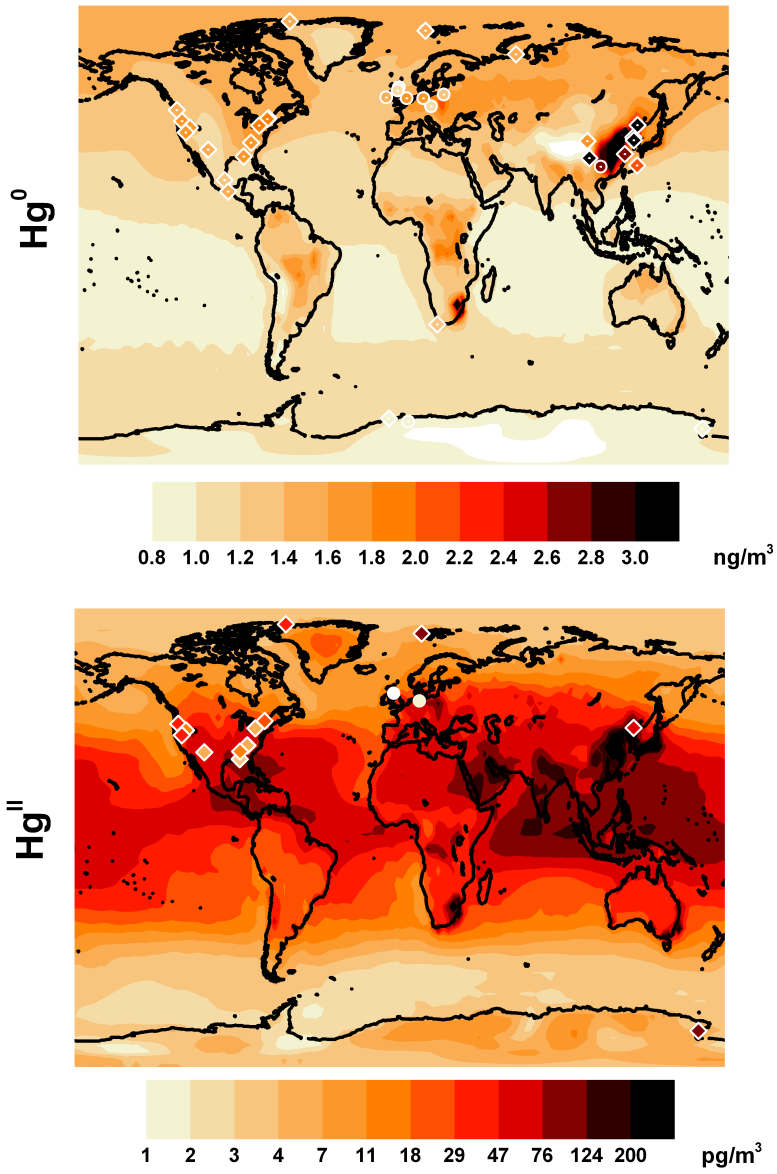

Figure 2.4.4: Spatial distribution of annually averaged air concentrations of Hg^{o} and Hg^{II} . The background model simulated data and the measurements for Hg^{o} are the same of Figure 2.4.3. Hg^{II} observations include those used by [119] plus additional sites in Europe belonging to EMEP programme

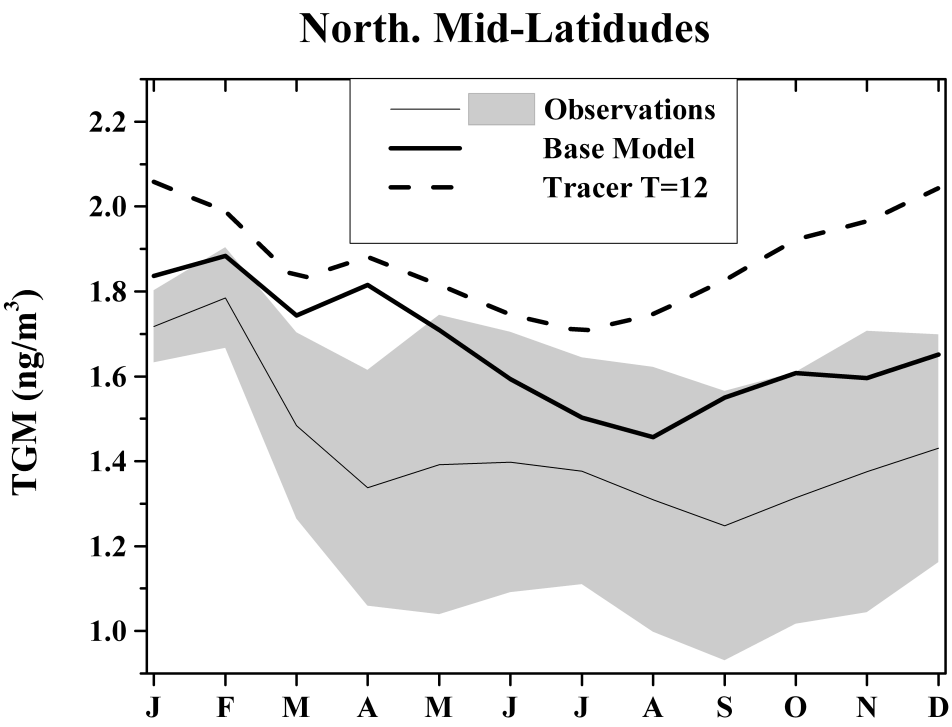

Figure 2.4.5: Mean seasonal variations of TGM at northern mid-latitudes. Observations are annual means averaged over 6 EMEP sites. Shadowed area indicates the standard deviation for observations.

centration at around 30 degree south, and caused by the peak in the South Africa, is due to an overestimation of Hg emissions in the region [18]. The global spatial correlation (by mean of the Pearson's r) is 0.7 with a slope of 0.85 and a normalised mean bias of -7% , in line with other model studies [49]

Figure 2.4.5 shows the comparison between simulated and observed monthly averages of TGM surface concentrations observed at Northern mid-latitudes sites (40-60°). The Base run compared with the observations has a normalised mean bias of 16%, and the correlation (Pearson's r) between them is 0.8. Using oxidation mechanism other than the Base gave poorer results. Interestingly the simulation in which oxidation by OH was not included gave particularly poor results, and correlation coefficient of just 0.1. In fact, observations show a minimum in the late

summer period in measurements. This minimum, well reproduced by the model, is attributed to oxidation of Hg by OH, and has been reported in previous modeling studies [49, 98].

2.5 Hg Ocean Evasion

Recently a number of papers focused on the estimation of Hg^0 evasion from oceans [67, 96, 99, 102, 111, 115] have been published. Figure 2.5.1 (a) shows the global distribution of the simulated annual Hg^0 ocean emissions. The largest fluxes occur in tropical regions where a combination of warm temperatures and relatively strong winds cause higher evasion rates. The mean Hg^0 emission flux for the ocean in tropical zones is between 0.7 and 1.5 $\mu g\, m^{-2}\, month^{-1}$ (Figure 2.5.1 (b)) and displays the largest seasonal variability at ± 15 degrees, reflecting the seasonal migration of the Intertropical Convergence Zone (ITCZ)[83, 108]. Around the equator there is an evasion minimum, and also a reduced seasonal variability due to the generally light winds in this area (the so-called Doldrums) [24]. Outside the tropics region, emissions from the northern hemisphere oceans show little seasonal variation, except for the Arctic Ocean where the seasonal formation and loss of sea-ice play a role. The Southern hemisphere oceans, show generally greater annual Hg^0 emissions with respect to those in the North. Emissions are strong during the entire year with a moderate seasonal variation, emissions are particularly high between 40 and 50° N, due to the strong westerly winds found here, known as the roaring forties [108]. The pattern of the latitudinal distribution of Hg^0 ocean flux is similar to that obtained by Strode et al. [111], whereas the absolute values are somewhat greater since in Strode et al. [111] the mean global ocean concentrations of DGM was 0.07 pM. In table 2.5.1 the simulated annual Hg^0 emissions from the different ocean basins for the period 2008-2009 are shown, with previous estimates in parentheses (see Sunderland and Mason [115] and references therein). The total simulated oceanic flux of Hg^0 to the atmosphere, 5500 $Mg\, yr^{-1}$, is at the at the high end of the range of previous estimates (800-5300 $Mg\, yr^{-1}$) and is com-

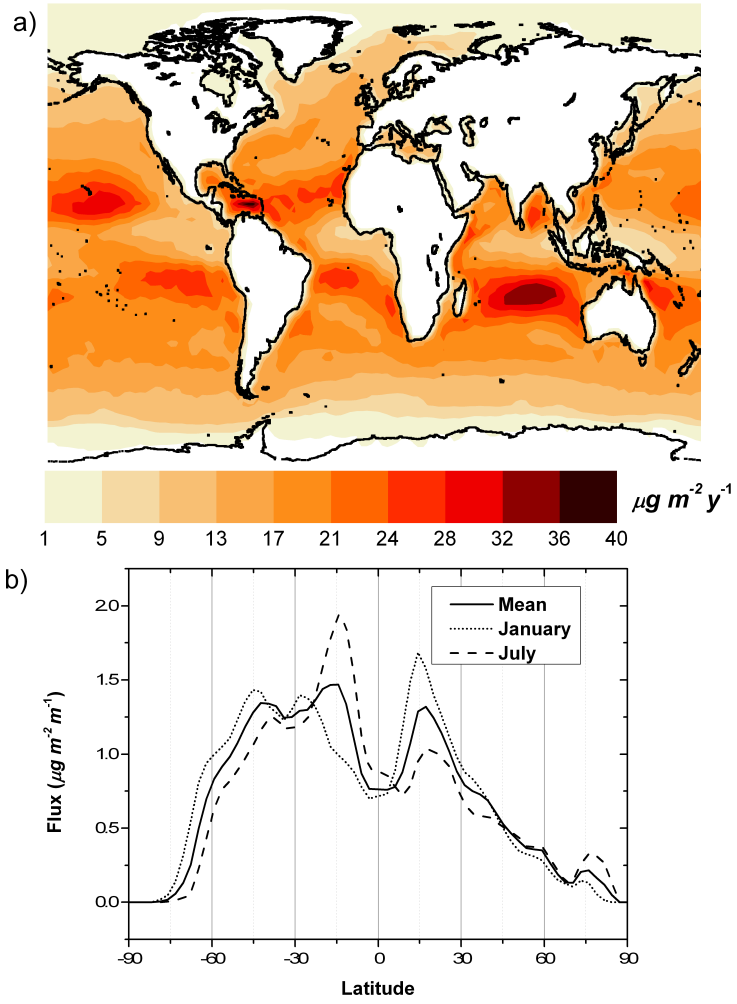

Figure 2.5.1: (a) Global distribution of Hg^o fluxes from oceans surface. Fluxes are annual mean values from the model simulation period. (b) Latitudinal distribution of the oceanic Hg^o Flux, in different seasons, and the annual mean.

Table 2.5.1: Simulated annual fluxes from the ocean to the atmosphere for the various ocean regions. Ranges (90% confidence intervals) of previously estimated fluxes are also reported.

Area	Latitude Range	Fluxes (Estimates) (Tons/y)
North Atlantic	>55 °N	49 (40-220)
Sur. Atlantic	35 °S - 55°N	731 (160 -1300)
Int. Atlantic	65 °S - 35°S	166 (20 -160)
Mediterranean	30 °S - 40°N	29 (8 -80)
North Pacific	>30 °N	407 (80-360)
Sur. Pacific & Indian	40 °S - 30°N	2925 (380 -2600)
Int. Pacific & Indian	65°S - 40°S	659 (60 -440)
Surf. Antarctic	>65°S	26 (4 - 22)
Other Basins, rivers and lakes		546 (30 -100)
Total		5537 (782 - 5282)

parable with the estimate of Selin et al. [99] of 5000 Mg yr^{-1}. This difference in the magnitude of the ocean evasion, with respect to other modeling studies may be due to differences between the re-analysis data used by ECHMERIT (ECMWF era-interim) and that used in other models. Moreover it should be noted that these are the first Hg^0 ocean emission estimates carried-out using a global scale on-line model, that does not interpolate in any way the meteorological fields (in either time and space) used in the parametrised calculation of oceanic Hg^0 fluxes.

2.6 Hg deposition

Figure 2.6.1 shows the averaged annual Hg^{II} wet deposition over the globe during simulation period as simulated by the Base model. The deposition is greatest over Asia, East Europe and over the eastern coast of North America, reflecting the largest anthropogenic emissions in these area.

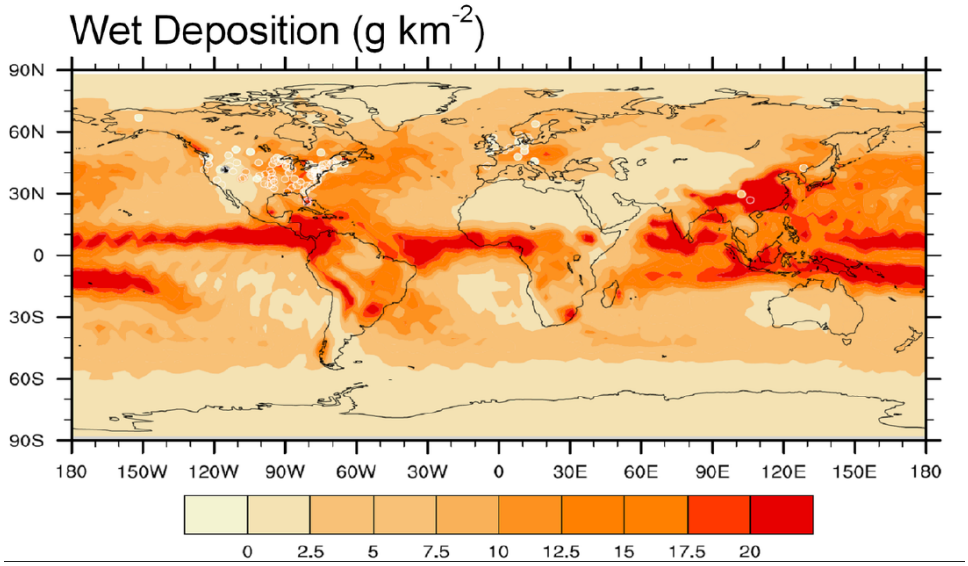

Figure 2.6.1: Global distribution of wet deposition fluxes during the simulation period

WET DEPOSITION OVER NORTH AMERICA Stations making up the Mercury Deposition Network (MDN, [39]) over North America collected samples on a weekly basis. In order to make an effective comparison between modelled and observed data only the stations that successfully collected data covering at least 3/4 of each year of the simulated period. Moreover any stations with no samples for a period longer than a month were excluded from the analysis. Figure 2.6.2 compares the results of the Base model with data collected by the MDN network for the simulated period, 2008-2009. Simulations reproduce well fluxes observed by MDN network over the western US, where emission levels are the lowest. In the Eastern US where the highest anthropogenic emissions occur and indeed the measurements at MDN sites are also highest the model overestimates the observed deposition by almost a factor of 2 during the year. However this overestimation shows a distinct regional and seasonal variation. Figure 2.6.3 compares the simulated wet deposition with the observations in each seasons. The largest discrepancies between the model

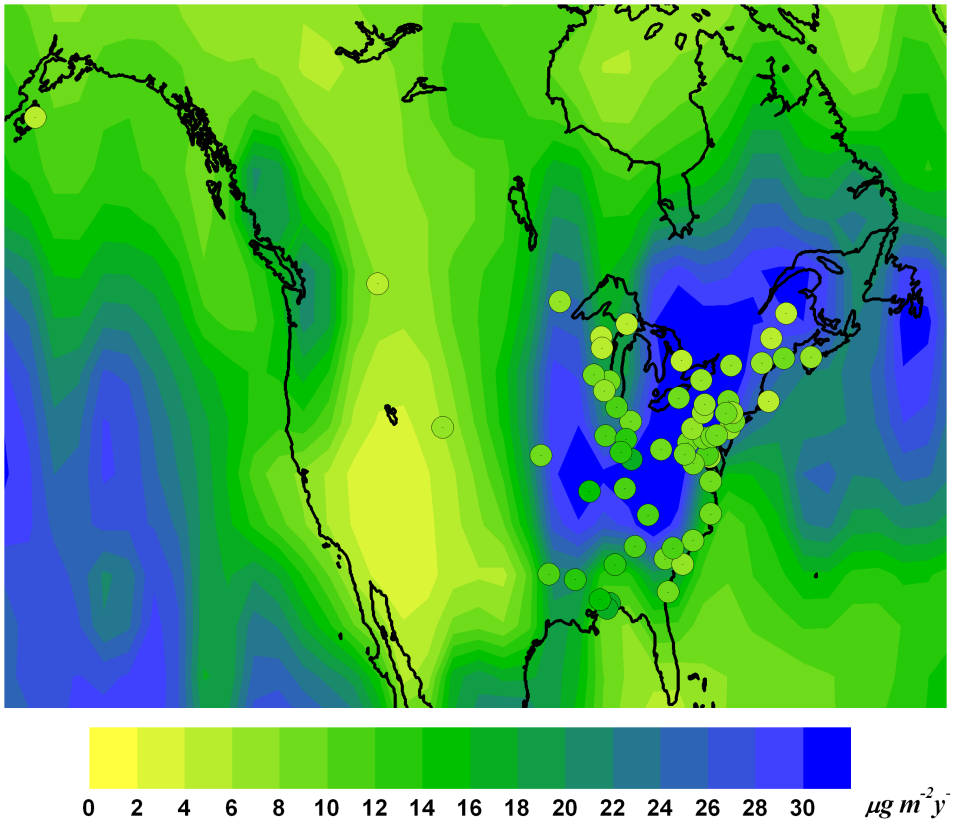

Figure 2.6.2: Annual Hg wet deposition fluxes over North America during 2008-2009 as simulated by base model. Overlaid circles show wet deposition observed during the same years by Mercury Deposition Network (MDN)

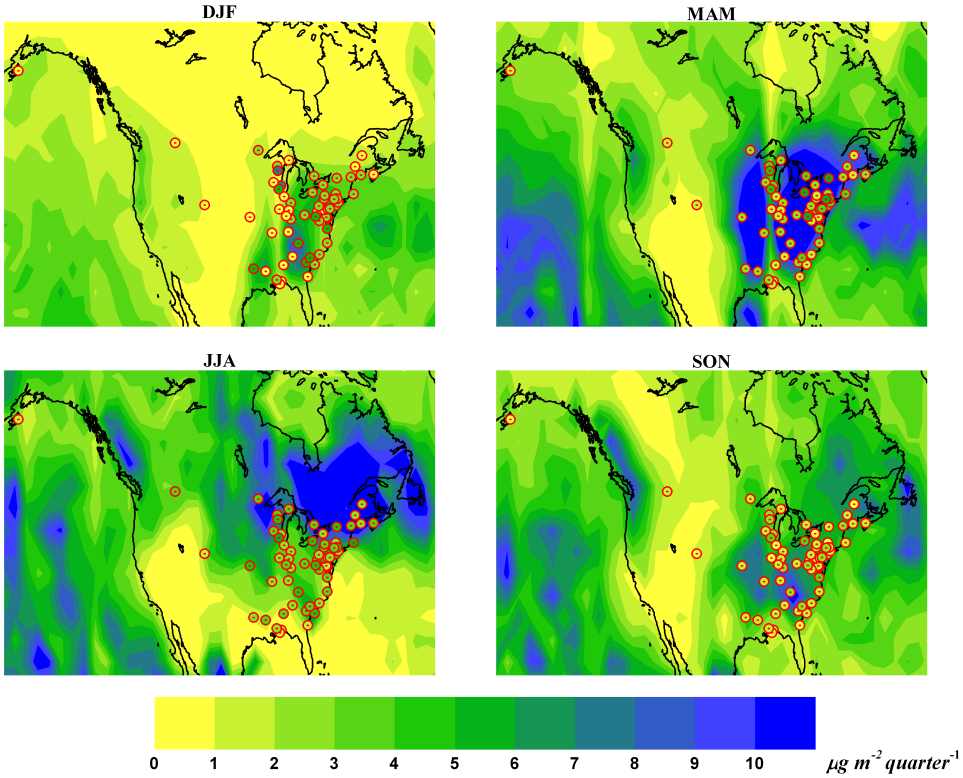

Figure 2.6.3: Seasonal Hg wet deposition fluxes over North America averaged over 2008-2009 period, as simulated by base model (background) and observed by MDN sites (Circles).

and observations occur in the Spring and Summer and in the more industrialised north-eastern part of the US. Emissions of Hg from this area would mostly be deposited locally and rapidly in the wetter autumn and winter months, however in Spring and Summer they are more likely to be transported further. However if the emissions have too high a proportion of Hg^{II} this could cause the model to overestimate the deposition nearby to sources. Zhang et al. [140] have considered this possibility in a nested regional simulation within their global model.

Wet Deposition over Europe Figure 2.6.4 compares the results obtained by the Base model with annual wet deposition data collected by European Monitoring and Evaluation Programme (EMEP) during 2008-2009. As above sites with at least 75 % of data available for each year of simulation period were used for the comparison. The highest wet deposition fluxes simulated by the model (the Base redox mechanism) are over the central and oriental area of the Europe, where the emissions from anthropogenic sources are the highest. The high wet deposition fluxes over some areas of the Atlantic Coast of Europe are due, at least in part to the frequent precipitation which occurs there. The model shows generally good geographical agreement with the observations, especially over the coastal regions of Northern Europe, but tends to overestimate deposition fluxes in the more industrialised regions of Central/Eastern Europe. Again this may be due to the proportion of oxidised Hg species in emissions, however due to the lack of monitoring stations in less industrial regions, particularly in Southern Europe it is not really possible to compare areas which are more and less directly impacted by local sources.

2.6.1 Global Hg Budget

Figure 2.6.5 shows the global budget of the Hg as simulated by our Base model considering the updated emissions.

As described in sections 2.2.1 and 2.5 the anthropogenic and ocean emissions account for 2300 and 5500 $Mg\,y^{-1}$. Terrestrial primary emissions from biogenic

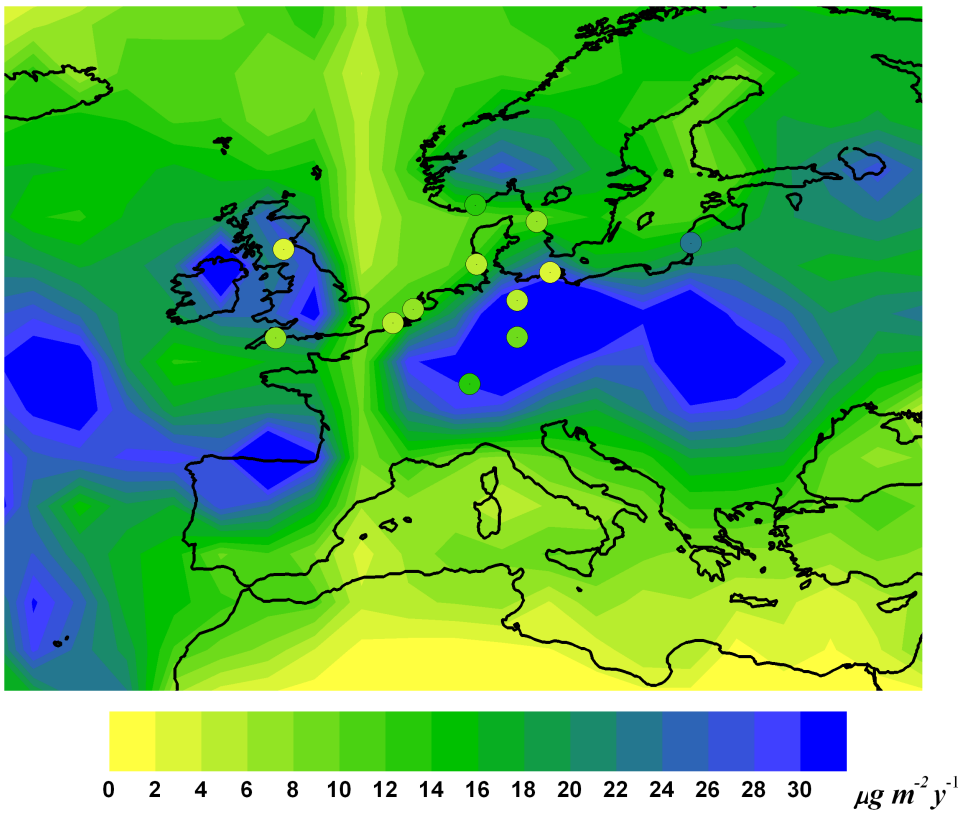

Figure 2.6.4: Annual Hg wet deposition fluxes over Europe during 2008-2009 as simulated by base model. Overlaid circles show wet deposition observed during the same years by EMEP sites.

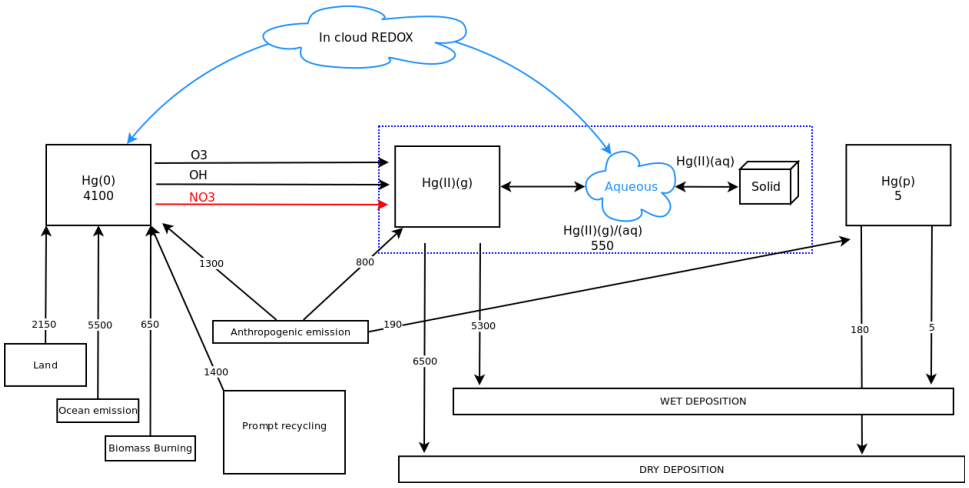

Figure 2.6.5: The total annual global Hg budget as derived from the base model. Emission and deposition rates are given in Mg y^{-1}. Inventories are in Mg.

activities, evapotranspiration and forest fires account for 2800 Mg y^{-1} close to other modelling estimates [99]. The prompt recycling of the previously deposited Hg species account for 1400 Mg y^{-1}, greater than previously reported [59, 99], reflecting the greater total deposition. The total source of Hg to the atmosphere is 11800 Mg y^{-1}, at the upper end of the range (6200-11200 Mg y^{-1}) previously estimated by GEOS-Chem [98, 99] and slightly larger than the recent independent estimate of 9700 Mg y^{-1} using CAM-Chem [59]. Almost all atmospheric Hg is removed as $Hg^{II}_{(g/aq)}$. Dry deposition in ECHMERIT is somewhat greater globally than wet deposition, (6500 vs 5300 Mg y^{-1}). The dry deposition of Hg^0 is negligible (less than 10 Mg y^{-1}) due to the approach used for modelling the Hg^0 deposition velocity (section 2.6). Other recent studies that suggest a much greater Hg^0 dry deposition flux, also found an atmospheric lifetime of total Hg of 0.5 and 0.69 year [59, 99], much shorter than previously estimated (see for example Lindberg et al. [63]. Although a shorter lifetime was supported by a decreasing trend in atmospheric Hg concentrations at many sites [101], "other regions show an increase in the Hg levels", suggesting possible not well-known regional reasons rather than a global trend [122].

The emitted inert and insoluble Hg^P, 190 Mg y^{-1}, is almost all removed by dry deposition (180 Mg y^{-1}. It should be recalled that in ECHMERIT much of the Hg associated with particulate matter is present as the soluble species $Hg^{II}_{(aq)}$. The total burden of Hg in atmosphere is 4650 Mg of which 4100 are Hg^0, 550 $Hg^{II}_{(g/aq)}$ and only a small fraction is Hg^P.

Much of the content of this chapter appeared in [29]

3

A Model Study of Global Mercury Deposition from Biomass Burning

Among all emissions source increased attention has also been given to Biomass Burning (BB) emissions [23, 37, 131], in trying to constrain the global budget of Hg as it cycles between environmental compartments. Friedli et al. [37] estimated Hg emissions from BB by combining outputs from global carbon emission models with Hg enhancement ratios and found that globally 675 ($\pm$240) Mg yr^{-1}, averaged over the period 1997-2006, is emitted from BB. As this figure is approximately one third of the yearly anthropogenic emissions of Hg to the atmosphere, it is clear that BB plays an important role in the Hg biogeochemical cycle. As controls on anthropogenic Hg emissions become stricter, proportionally the role of BB will increase, possibly substantially if the instances and extent of wildfires in-

creases in a changing climate. It should also be noted that the location of Hg emissions from BB is very different from the location of anthropogenic emissions, with the exception of artisanal and small scale gold mining. Mercury from BB is almost all emitted as $Hg^{0}_{(g)}$, with a small fraction associated with the soot from the fires [73]. Elemental mercury has an estimated lifetime of between 8 months and 1 year [32, 49, 91] and therefore can be deposited to ecosystems very distant from fire locations.

Atmospheric $Hg^{0}_{(g)}$ can be oxidized to $Hg^{II}_{(g)}$, which is subsequently removed by both wet and dry deposition. A part of the Hg^{II} that is deposited may be methylated within ecosystems and it is this form of Hg which can enter the food web and is toxic to living organisms. The recent Minamata Convention[1] is aimed at reducing the anthropogenic impact on the global Hg biogeochemical cycle [97]. However, the natural Hg cycle is already significantly perturbed; it is estimated that there is five times the Hg in the present day atmosphere than was present in pre-industrial times [32, 110]. The legacy of past emissions will most likely continue to influence the global biogeochemical cycle of Hg for decades to come [10], and fires will play an important role in the continued cycling of Hg between environmental compartments. The primary objective of the study is to simulate the magnitude and geographical location of the Hg deposition flux that result from BB.

Three recent BB inventories, FINNv1.0 [130], GFEDv3.1 [125] and GFASv1.0 [56], referred to simply as FINN, GFED and GFAS hereafter, have been used to simulate Hg emissions from fires over the period 2006–2010. Hg emissions have been calculated as a function of CO emissions and the deposition flux distribution of Hg from BB has been simulated, using the global on-line chemical transport Hg model ECHMERIT [28, 55].

[1] http://www.mercuryconvention.org/

3.1 Methodology

3.1.1 The Global Biomass Burning Inventories

The details of the three inventories used, FINN, GFAS, and GFED and how they were compiled can be found in the literature [56, 125, 130]. All three inventories are based on the imagery obtained from the MODIS instruments on-board the NASA Terra and Aqua satellites; however they differ in the way in which the data are filtered or processed. GFED makes use of the burned area retrieval, FINN uses an active fire data product, while GFAS uses fire radiative power retrievals (the algorithm for which is based on active fire detection). Further differences in the inventories concern the land cover maps used, and the details concerning fuel load and fuel consumption. A detailed comparison and description of the inventories can be found in Andela et al. [1].

Over the period 2003–2011 three inventories agree fairly well on the annual average CO emissions [1]. The inventories identify the same regional BB hot spots caused by tropical deforestation in South America, fires in African savannas, forest fires in South-East Asia and seasonal wildfires in Northern Hemisphere boreal regions. However, the regional differences in CO emissions between FINN, GFAS and GFED are substantial. GFAS has the highest values for areas with low burning intensity such as dry savannas. Conversely for high burning intensity fires, GFED has higher emissions. The different approaches in compiling the inventories is apparent from the relatively high emission estimate of GFAS and FINN in some areas of the world (Africa, South-East Asia and northern Brazil), whereas GFED is tuned particularly to capture large scale deforestation in central Brazil. GFED thus has higher emissions in the Southern Hemisphere than FINN and GFAS. For boreal forests GFAS and GFED emission estimates are considerably higher than FINN, see Andela et al.[1].

The GFAS and GFED inventories were obtained from the Emissions of Atmospheric Compounds and Compilation of Ancillary Data (ECCAD) Global Emis-

sions InitiAtive (GEIA) portal [2], while the FINN inventory was obtained from the Atmospheric Chemistry Division of National Center for Atmospheric Research (NCAR) [3]. For the purpose of model validation the most recent anthropogenic Hg emission inventory from AMAP/UNEP (reference year 2010) was used [7].

3.1.2 Model set-up

The global Hg chemical transport model ECHMERIT [28, 55] is based on the fifth generation General Circulation Model ECHAM5 [84, 85]. ECHMERIT was run using T42 horizontal resolution (roughly 2.8° by 2.8° at the equator) and 19 vertical levels up to 10 hPa. The increase in atmospheric Hg concentration resulting from BB were estimated as in Chapter 2.2.2 The GFAS and GFED emissions were mapped on the ECHMERIT T42 grid using the mass conserving remapping tool included in the Climate Data Operators (CDO) [5]. The NCAR ACD Fortran pre-processor program, *Fire_Emis*, was used to interpolate the FINN inventory on to the ECHMERIT grid [3]. The monthly average emissions were calculated for the FINN and GFAS inventories to be compatible with the GFED inventory.

With the exception of the simulations performed for model validation purposes, all simulations were performed using Hg emissions from BB only.

3.1.3 Oxidation Mechanisms

To study the impact of different oxidation schemes on the global deposition of Hg from BB some simplified variants of the original ECHMERIT full chemistry mechanism were needed, to reduce the computational demands of the chemistry routine. With this aim we implemented a chemical mechanism where the reactant concentration fields were imported off-line.

[2] http://bai.acd.ucar.edu/Data/fire/

[3] http://eccad.sedoo.fr/eccad_extract_interface/JSF/page_products_em.jsfdatabase

Base case oxidation mechanism

The base mechanism includes the $Hg^{\circ}_{(g)}$ oxidation of in $Hg^{II}_{(g/aq)}$ oxidation by OH and O_3 in the gas and aqueous phases. OH and O_3 concentration fields were imported from MOZART (Model for Ozone and Related chemical Tracers). The 6-hourly output from MOZART was interpolated in time to give hourly values using the ratio between solar radiation and daily maximum solar radiation for OH. A simple linear interpolation was chosen for the O_3.

Br-Based oxidation mechanism

To analyse the effect of Hg oxidation by Br on the Hg deposition fields a two-step gas phase oxidation mechanism, similar to the approach used by Holmes et al. [49], was implemented: Br initiates $Hg^{\circ}_{(g)}$ oxidation, forming unstable HgBr* [31]; this can decompose or react with OH and Br to form $Hg^{II}_{(g)}$ at a rate as described in Goodsite et al. [41]. Bromine concentrations were imported off-line from the three-dimensional tropospheric chemical transport model p-TOMCAT, now modified to include a detailed bromine chemistry scheme, also in the MBL [134, 135], making it no longer necessary to include the MBL sea-salt aerosol bromide parametrization used in Holmes et al. [49] (based on Platt and Janssen [80]). The 2 hourly output of Br from p-TOMCAT model was interpolated to provide hourly input for ECHMERIT. The reactions used for the two mechanisms included in the model are summarized in table 3.1.1.

Table 3.1.1: Reactions used in the model.

Reaction	Rate constant $cm^3\ molecule^{-1}\ s^{-1}$	Reference
(1) $Hg^0 + O_3 \longrightarrow Hg^{II}_{(g)}$	$3.0 \cdot 10^{-20}$	Hall [46]
(2) $Hg^0 + OH \longrightarrow Hg^{II}_{(g)}$	$8.7 \cdot 10^{-14}$	Sommar et al. [106]
(3) $Hg^0_{(aq)} + O_{3(aq)} \longrightarrow Hg^{II}_{(aq)}$	$4.7 \cdot 10^7$ **	Munthe [71]
(4) $Hg^0 + Br \longrightarrow HgBr$	$3.7 \cdot 10^{-13}\ (T/298)^{-2.76}$	Goodsite et al. [41]
(5) $HgBr + Br \longrightarrow Hg^{II}_{(g)}$	$2.5 \cdot 10^{-10}\ (T/298)^{-0.57}$	Goodsite et al. [40]
(6) $HgBr + OH \longrightarrow Hg^{II}_{(g)}$	$2.5 \cdot 10^{-10}\ (T/298)^{-0.57}$	Goodsite et al. [40]
(4) $HgBr \longrightarrow Hg^0 + Br$	$4.0 \cdot 10^9\ exp(-7292/T)$	Goodsite et al. [41]

3.1.4 The simulations performed

Base case simulations used the O_3/OH oxidation mechanism, however there is some uncertainty over the atmospheric Hg oxidation pathway [51, 113, 114], therefore simulations were performed using a Br based oxidation mechanism to assess how the oxidation mechanism influences the deposition flux fields. Further simulations were performed introducing the BB emissions into different model levels, and combinations of levels. Five year simulations (2006–2010) were performed to investigate long-term differences between the inventories, while single year simulations were performed to investigate how deposition patterns varied from year to year. In the case of the single year simulations, since these were aimed at assessing the direct deposition of Hg, the mechanism by which a fraction of deposited Hg is rapidly re-emitted from terrestrial, snow/ice and water surfaces [99] was switched off, in all other simulations re-emission was included. Single year simulations were continued beyond 12 months without further emissions until at least 95% of the emitted Hg had been deposited. This took a further 9 to 12 months. Finally, simulations to investigate the differences in emission and deposition fields when using biome/land-cover based ERs were performed. A summary of the simulations performed can be found in Table 3.1.2.

Table 3.1.2: Simulations performed with ECHMERIT

Family	Short description	Simulation Period*	Inventory(ies)	Scope of analysis
Model Validation	BASE + All emissions	2010	GFAS-GFED-FINN	Measur. comp.
	Br-based + All emissions	2010	GFED	Measur. comp.
	12 month fixed lifetime	2010	GFED	Measur. comp.
Long Run (LR)	BASE	(2006 to 2010)	GFAS-GFED-FINN	Inventories comp.
Short Run (SR)	BASE	2006	GFAS-GFED-FINN	Inventories comp.
	BASE	2007	GFAS-GFED-FINN	Inventories comp.
	BASE	2008	GFAS-GFED-FINN	Inventories comp.
	BASE	2009	GFAS-GFED-FINN	Inventories comp.
	BASE	2010	GFAS-GFED-FINN	Inventories comp.
Sensitivity Runs	Br-based Ox. mech.	2010	GFAS-GFED-FINN	Ox. mech.
	12 month fixed lifetime	2010	GFAS-GFED-FINN	Lifetime of Hg(0)
	6 month fixed lifetime	2010	GFAS-GFED-FINN	Lifetime of Hg(0)
	emiss. level 1	2010	GFED	Injection height impact
	emiss. level 2	2010	GFED	Injection height impact
	emiss. level 4	2010	GFED	Injection height impact
	emiss. level 6	2010	GFED	Injection height impact
	emiss. uniform in PBL	2010	GFED	Injection height impact
	emiss. lat dependent profile	2010	GFED	Inj. height impact
	Specific ER_{coarse}	2010	GFED	ER impact
	Specific ER_{fine}	2010	GFED	ER impact

*Single year simulations were continued beyond 12 months until 95% of the emitted Hg had been removed from the atmosphere

3.2 Results

Although the primary aim of this study is to identify the areas most impacted by Hg emissions from BB, and to see how greatly these differ from one BB inventory to another, the first simulations were performed using Hg emissions from all sources. The full version of the model, including all the mercury emissions sources as described in [28] (but implementing the most recent AMAP/UNEP emission inventory, [4]) was run for the year 2010 (with 4 years of spin-up), using both the oxidation mechanisms detailed in this section. The Base model was run with all three inventories, whereas the Br-based simulation was performed using just GFED. GFED was also used for simulations using a fixed lifetime against oxidation ("pseudo" oxidation mechanism). The results from these simulations were compared to available measurement data, and a statistical summary of the comparison for gas phase Hg and for Hg wet deposition can be found in table 3.2.1,

Table 3.2.1: Comparison of the Base, Br and fixed lifetime simulations with global observations for 2010

		FINN Base	GFAS Base	GFED Base	GFED Br-Oxdn	GFED 12-m fixed
TGM	Intercept	0.34	0.31	0.34	0.18	0.34
	Slope	0.68	0.69	0.67	0.72	0.70
	Pearson's r	0.77	0.78	0.77	0.75	0.76
	NRMSE(%)	14.6	14.4	14.3	16.7	15.5
Wet Dep	Intercept	9.26	9.05	9.11	10.4	7.15
	Slope	0.32	0.31	0.31	0.22	0.19
	Pearson's r	0.21	0.21	0.21	0.14	0.17
	NRMSE(%)	19.1	18.6	18.8	19.6	13.9

whereas figures 3.2.1 to 3.2.3 shows the map of such comparison. The comparison between the different model versions and observations all yield similar results, which are reasonable for Total Gaseous Mercury (TGM, the sum of gas phase elemental and oxidized Hg species), and less good for Hg wet deposition. Interestingly simply assuming a fixed atmospheric lifetime for Hg does not give results that are significantly worse than when a more detailed chemical mechanism is employed. However it should be pointed out that for the year 2010 almost all the observations are from the northern hemisphere, and this may not be the case when southern hemisphere sites are taken into account. (Currently the Global Mercury Observation System project is performing Hg monitoring at a number of sites in the southern hemisphere [5]).

3.2.1 Geographical distribution and seasonality of emissions

The temporal and spatial distribution of the Hg emissions is dictated by the distribution of CO emissions because of the way they have been calculated. The differ-

[4] http://www.amap.no/mercury-emissions
[5] www.gmos.eu

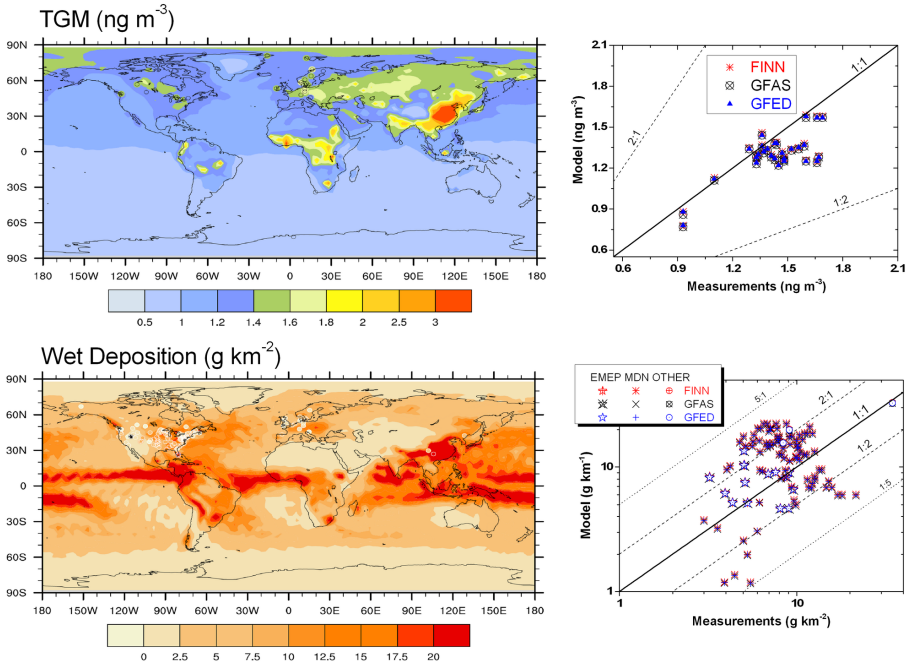

Figure 3.2.1: Validation of the Base Model. Note that the deposition scatter plot has a log scale (both for x and y) to better visualize the outliers.

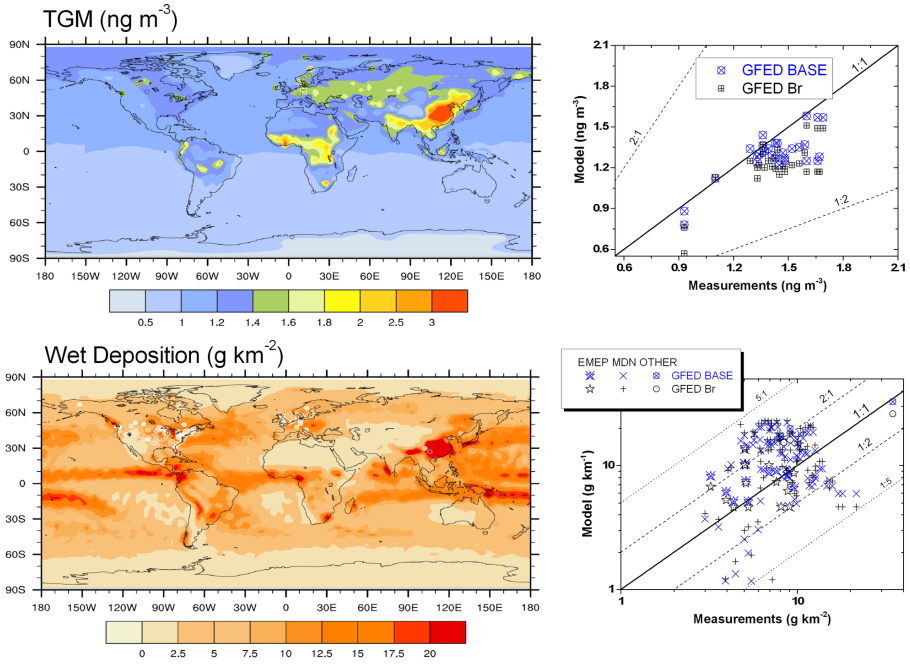

Figure 3.2.2: Validation of Br-Based Model using the GFED inventory. Performance is compared to the GFED Base simulation. Note that the deposition scatter plot has a log scale (both for x and y) to better visualize the outliers.

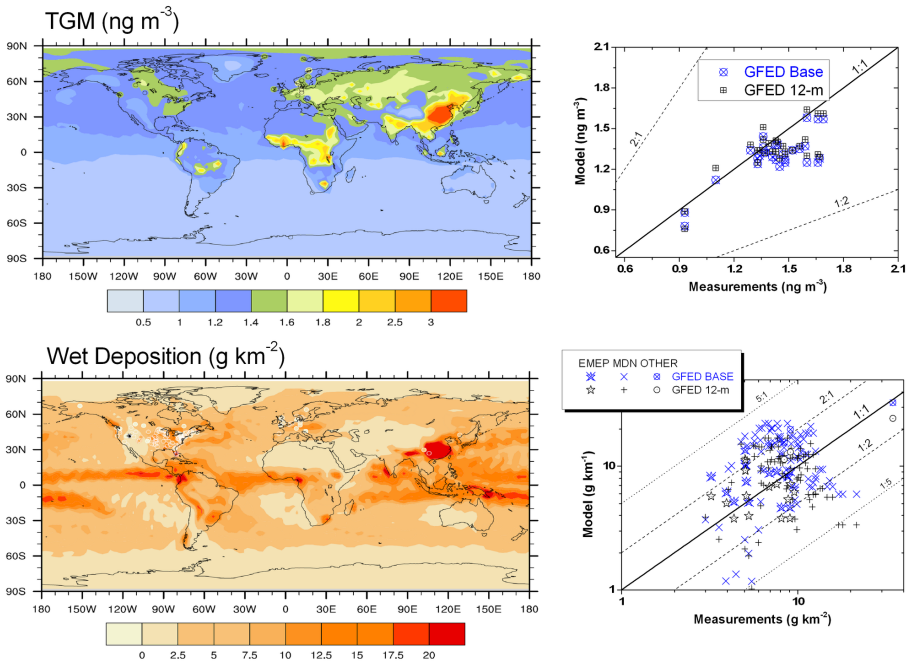

Figure 3.2.3: Validation of the 12 month fixed lifetime using the GFED inventory. Performance is compared to the GFED Base simulation. Note that the deposition scatter plot has a log scale (both for x and y) to better visualize the outliers.

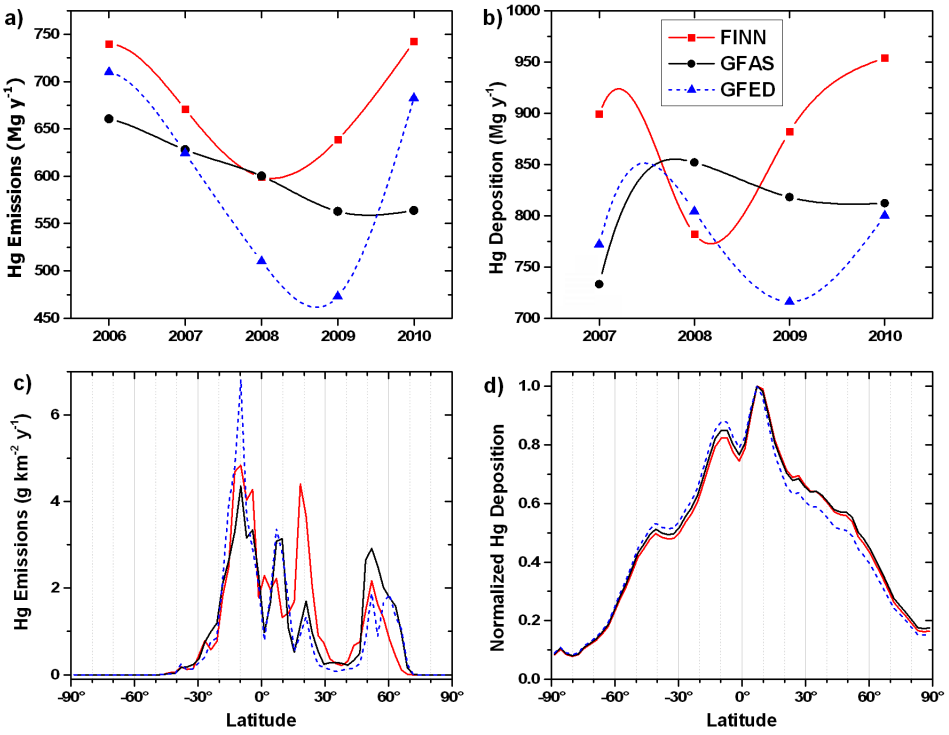

Figure 3.2.4: Annual trends and averaged latitudinal profiles of mercury emissions ((a) and (c)) and deposition ((b) and (d)). Figure (b) excludes 2006 due to low re-emissions, see section 3.2.2

ences between the inventories, in terms of CO emissions, are described elsewhere [1, 56, 112, 125, 130].

Although the annual average Hg emitted between 2006–2010 is similar: 678, 603 and 600 Mg for FINN, GFAS and GFED respectively, there are significant interannual differences and noticeable variations in the latitudinal distribution (see Figure 3.2.4). The highest year to year variability is seen in the GFED inventory. While the FINN and GFED inventories have similar temporal profiles and are reasonably correlated ($r = 0.9$). The GFAS inventory shows a markedly different temporal profile, Figure 3.2.4(a) ($r = 0.2$ and 0.5, with FINN and GFED respectively).

The decreasing trend in emissions over time seen in the GFAS inventory is also at odds with the other two inventories.

The latitudinal profiles of the emissions, for the period 2006-2010, while similar, do have noticeable differences (Figure 3.2.4(c)). The GFED inventory has significantly higher emissions at around 10°S (6.4 g km^{-2} y^{-1}), whereas the FINN inventory shows a much higher peak at around 20°N (4.2 g km^{-2} y^{-1}). The FINN inventory also lacks the peaks at 7°N and at 65°N which are evident in the GFAS and GFED inventories. In terms of the latitudinal profile the GFAS and GFED inventories show the highest correlation (r = 0.9). The global Hg emission spatial and seasonal distributions are shown in Figure 3.2.5, as is the distribution of the emissions between source regions.

3.2.2 Hg deposition

Five year simulations

Figure 3.2.6 shows the geographical distribution of the annual total deposition (wet plus dry) due to BB averaged over the last four years of the 5 year simulation period, (to avoid the first year where re-emission is lower). Not surprisingly, high emissions combined with high precipitation downwind of emission source regions gives rise to high deposition fluxes. Figure 3.2.6 also shows that while BB emissions are terrestrial, most of the Hg deposition occurs over the oceans. The yearly Hg deposition totals using each inventory follow the emission totals (but also include deposition of re-remitted Hg), (see figures 3.2.4(a) and 3.2.4(b)). The emissions latitudinal profile have well defined peaks and a distinct cut-off at the southern and northern limits of vegetation (Fig. 3.2.4(c)). The deposition profile, due to the lifetime of Hg in the atmosphere, shows far less pronounced peaks, a broader profile, and never reaches zero, at any latitude, Fig. 3.2.4(d). Looking at the southern hemisphere, almost all emissions are between the equator and 30°S, even at 50°S the Hg deposition is still 40% of that seen in the high Hg deposition regions. This latitudinal distribution of the Hg is almost independent of the BB emissions in-

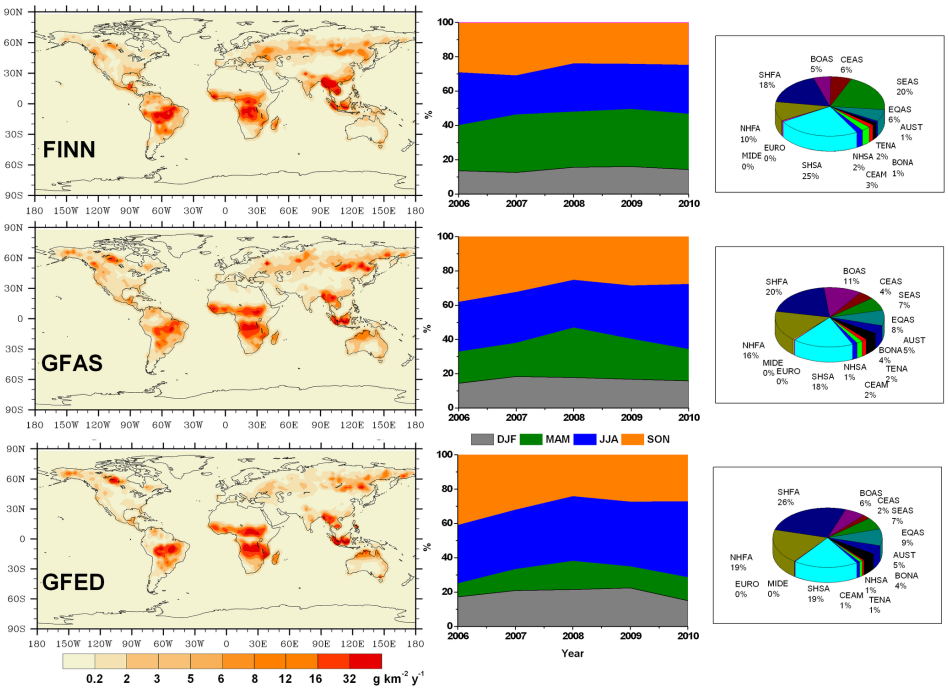

Figure 3.2.5: Geographical (left), seasonal (center, DJF - December January February, MAM - March April May etc.) and regional (right) distribution of mercury emissions. Annual averages over the 2006–2010 period. The regions are, following the nomenclature used in van der Werf et al. [125], (Boreal North America (BONA), Temperate North America (TENA), Central America (CEAM), Northern Hemisphere South America (NHSA), Southern Hemisphere South America (SHSA), Europe (EURO), Middle East (MIDE), Northern Hemisphere Africa (NHAF), Southern Hemisphere Africa (SHAF), Boreal Asia (BOAS), Central Asia (CEAS), Southeast Asia (SEAS), Equatorial Asia (EQAS) and Australia (AUST)

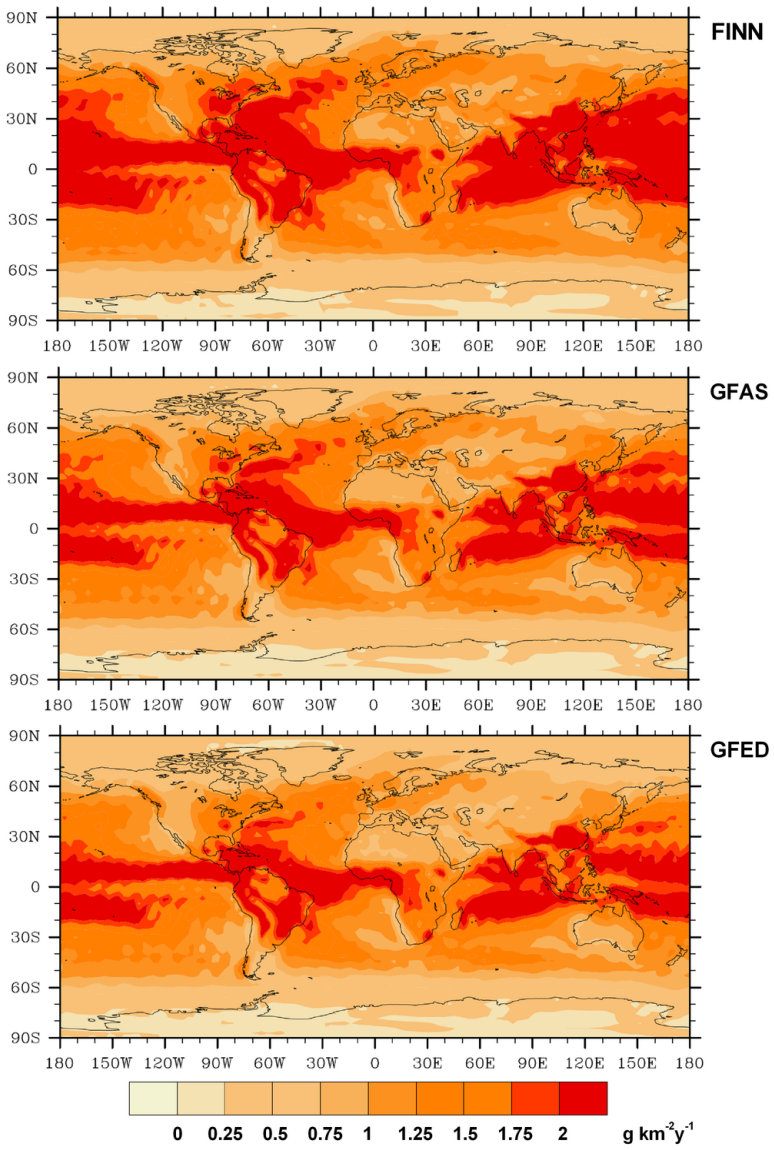

Figure 3.2.6: Geographical distribution of the total mercury deposition (wet + dry) that result from BB. Annual averages over the 2007–2010 period.

ventory used, indicating that atmospheric transport determines to a great extent the Hg deposition flux distribution.

Another way to illustrate the importance of atmospheric transport on the simulated deposition fields is to compare the spatial correlation (R) of the emission and the deposition fields, Table 3.2.2. The values reported were calculated using the horizontal pattern correlation method [89, 90]. The highest correlation for the emission inventories is found between GFAS and GFED (R = 0.68), the lowest between FINN and GFED (R = 0.38). The value of R varies from year to year (Table 3.2.2), reflecting differences in the approaches used to compile the inventories, which are discussed by Andela et al. [1]. Higher spatial correlations (R very close to 1) are found for the simulated Hg deposition fields, due to the effect of the $Hg^{0}_{(g)}$ atmospheric lifetime, and hence transport, which smooths the variations seen in the emissions.

Table 3.2.2: Spatial correlations (R) between the emissions inventories and the simulated deposition fields

	Emissions			Deposition		
Year	FINN-GFAS	FINN-GFED	GFAS-GFED	FINN-GFAS	FINN-GFED	GFAS-GFED
2006	0.47	0.33	0.82	1.00	0.97	0.98
2007	0.42	0.35	0.66	1.00	0.98	0.99
2008	0.30	0.31	0.56	0.99	0.99	0.99
2009	0.29	0.24	0.47	0.99	0.99	0.99
2010	0.31	0.37	0.46	0.99	0.99	0.99
2006-10	0.42	0.38	0.68	0.99	0.98	0.99

The net effect of BB in tropical regions is essentially to cycle Hg from the tropics to mid-latitudes and to a lesser extent to high latitudes (see Figure 3.2.7). Northern boreal BB directly impacts mid- and high latitudes.

3.2.3 Overall and yearly deposition comparison

To compare the deposition fields simulated using the three inventories, maps of agreement which highlight similarities and differences in geographically resolved

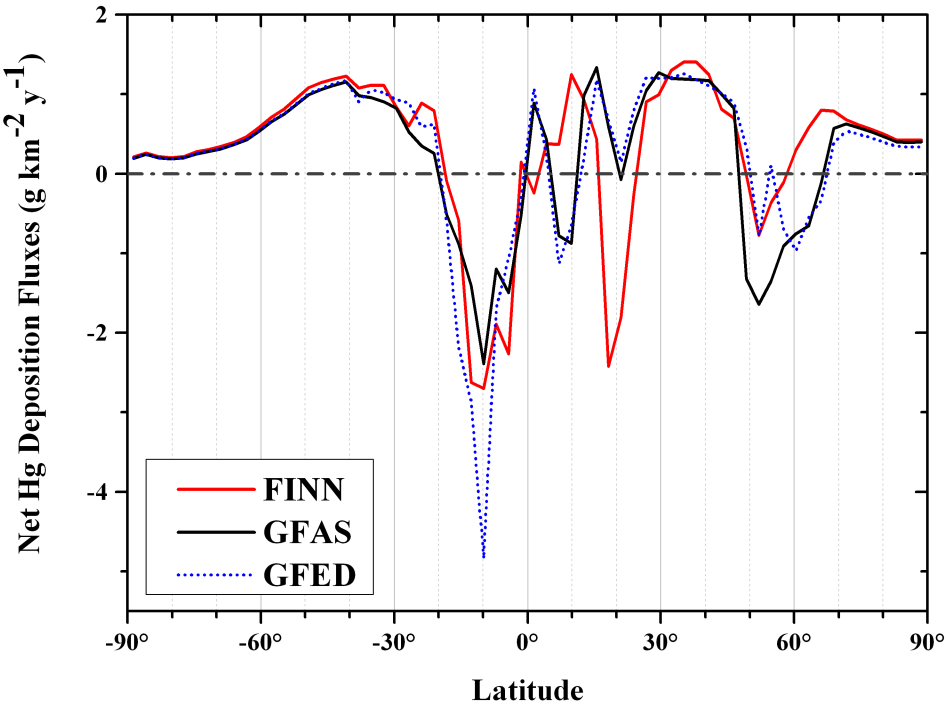

Figure 3.2.7: Latitudinal profile of annual Hg net deposition flux (Deposition - Emission), averaged over the period 2007–2010.

datasets can be used. Model cells in which the Hg deposition was greater than the average plus one standard deviation ($\mu + \sigma$) were identified for each BB inventory simulation. These cells were mapped to see how consistent the extremes of the deposition distribution is between the simulations. Figure 3.2.8 shows all of the areas where the deposition is greater than $\mu + \sigma$, for the 5 year (Base) simulations. The color of the cells denotes the level of agreement between the inventories. The high Hg deposition regions on which all the inventories agree represents roughly 15% of the Earth's surface, and as the map makes quite clear, most of these regions are over the tropical and northern oceans. The map (Figure 3.2.8) shows the agreement between the FINN and GFAS simulations (gray plus orange cells), and there are relatively few cells where these inventories are the only ones to predict high Hg deposition (red and yellow cells). In contrast the simulations performed using the GFED inventory show a difference in the prediction of regions of high Hg deposition, and particularly in the southern hemisphere, and to the southern edge of the region where all three inventories agree.

All of the inventories have an emission peak at roughly 10°S but while that of FINN and GFAS is $\approx$ 4.5-5 g km^{-2} y^{-1}, that in GFED is $\approx$ 7 g km^{-2} y^{-1}. This accounts for the large number of cells in the southern hemisphere where the simulation performed with GFED predicts high Hg deposition values. Interestingly, at around 20°N there is a peak in the FINN inventory that is more than twice as high as the corresponding values in GFED and GFAS. Given the relatively few areas where only the simulations with the FINN inventory predict high Hg deposition, this peak in emissions seems to affect the results relatively little, suggesting that at certain latitudes, differences (in magnitude and precise location) in the inventories have a negligible influence on the simulation results. (See Figure 3.2.4(c)). However in the case with the simulation performed using GFED, the magnitude and location of the emissions are much more important. Anthropogenic emissions in the southern hemisphere are low compared to the northern hemisphere, therefore the contribution to atmospheric Hg from BB is relatively more important in this region. From these results it appears that precision in the magnitude

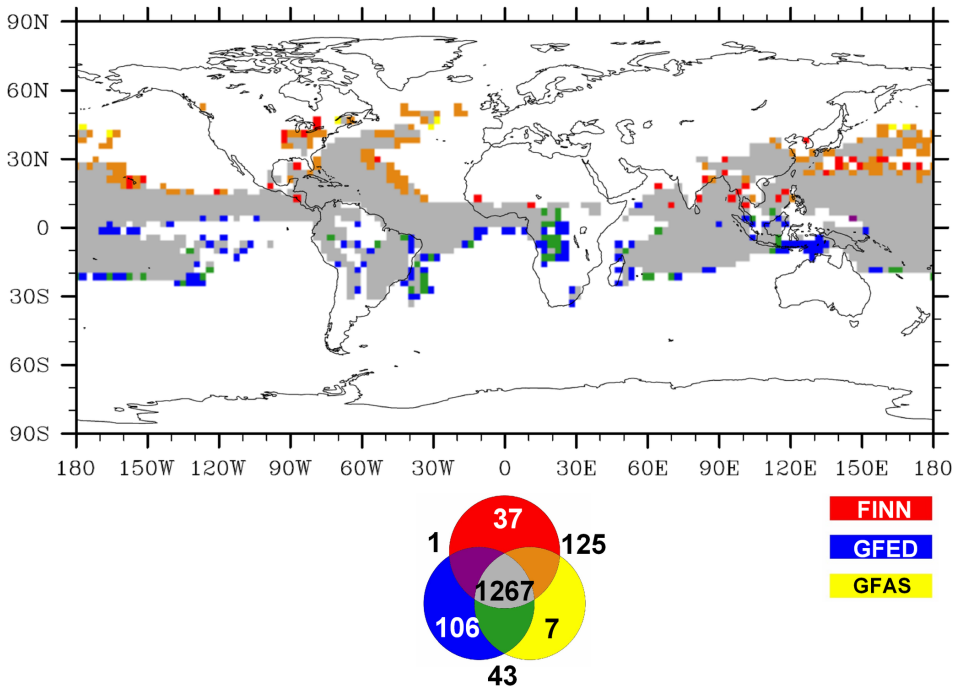

Figure 3.2.8: Agreement map of Hg deposition fields obtained from GFAS, GFED and FINN for the five year simulation. The map shows the areas where deposition is $> \mu+\sigma$. Primary colors (red, blue and yellow) represent non-agreement between inventories, green, purple and brown indicate agreement between two of the inventories and gray indicates agreement between all three. The numbers refer to the number of cells in common between the simulations using the different inventories (The whole globe is represented by 8192 cells)

and location of BB emissions in the southern hemisphere is particularly necessary.

ECHMERIT has also been run for individual years (2006–2010) using each of the emission inventories. As above for the 5 year simulation, agreement maps for deposition greater than $\mu + \sigma$ for each inventory have been prepared to compare the results from each inventory for each year. The simulations predict the same total global area of high deposition ($\approx$14-16%) each year, and also that these areas are consistent from year to year. While the FINN and GFAS inventories give similar results, the GFED inventory consistently predicts higher deposition in the Southern hemisphere. This is true for each of the single year simulations as it was for the 5 year simulation. Since the major BB source in south of the Equator is the Amazon, this may well reflects the fact that GFED is "tuned" to capture large scale deforestation in this region [1] (Figure 3.2.9).

3.2.4 Sensitivity Studies

The emission inventories used for these studies have their own intrinsic uncertainties [56, 125, 127, 130]. Biome specific emission factors, assumptions concerning the oxidation mechanism and the atmospheric lifetime of Hg, and also the height (model layer) at which the BB emissions are introduced into the atmosphere are all potential sources of uncertainty. Some of these uncertainties are common to all BB studies, such as plume modeling, injection height, diurnal variation of fire intensity, fire areas and enhancement ratios [37, 52]. To investigate the impact of the parameterizations on the Hg deposition fields a number of sensitivity runs were performed (see Table 3.1.2).

Enhancement ratio

The most critical of all the assumptions made concerning Hg emissions from BB is the Enhancement Ratio (ER). Using ER_{av} makes the modeling studies themselves more simple, and also avoids making a series of interconnected assumptions concerning ERs, vegetation types and their distribution, each of which could

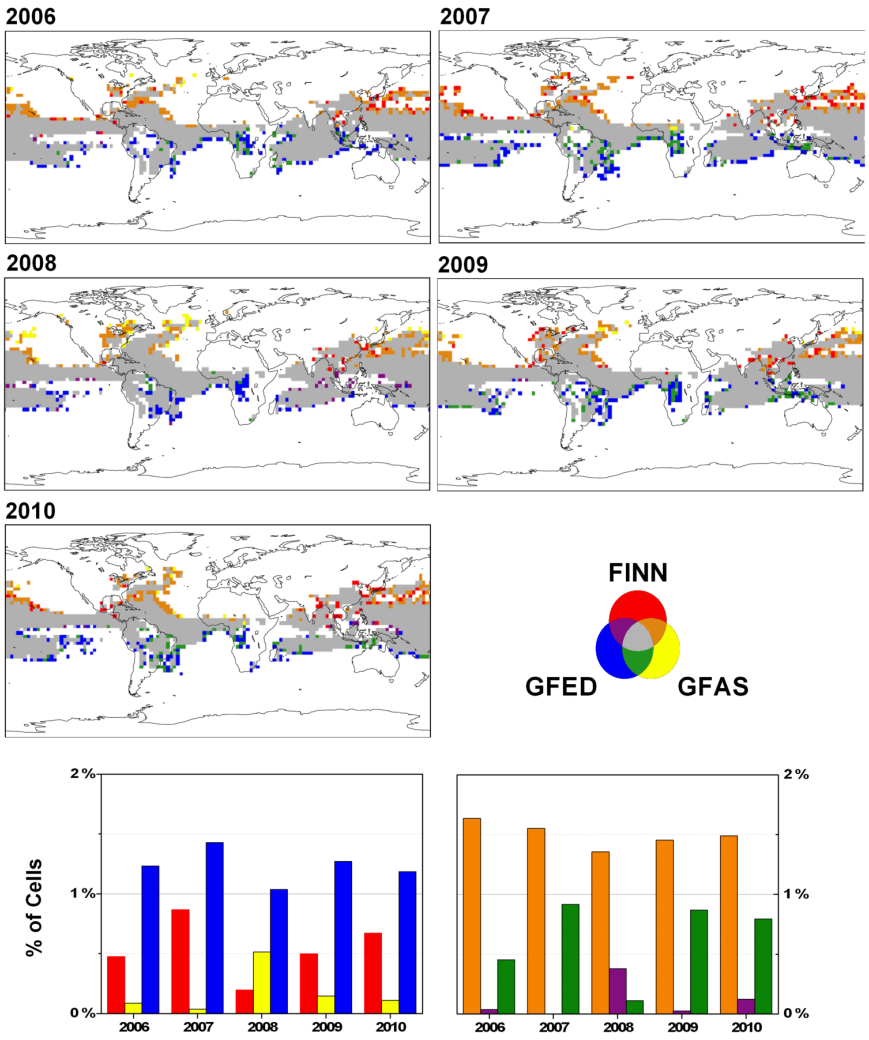

Figure 3.2.9: Agreement maps of Hg deposition for GFED, GFAS and FINN, for the single year simulations. The maps show the areas where deposition is greater than $\mu+\sigma$. Primary colors (red, blue and yellow) represent non-agreement between inventories, green, purple and brown indicate agreement between two of the inventories, and gray indicates agreement between all three. The numbers refer to the number of cells in common between the simulations using the different inventories (The whole globe is represented by 8192 cells)

potentially introduce further errors into the model. The two major uncertainties when attempting to use a biome dependent approach to Hg emissions from BB are knowledge of the distribution of vegetation types, and the ER associated with a given type of vegetation, which may vary with location. There have been relatively few determinations of Hg concentrations in BB plumes for specific vegetation types [37]. The ERs reported vary significantly for most vegetation types and can differ by more than an order of magnitude for a given biome. This is most likely due to a combination of factors including soil Hg content, fire intensity and fire location. Two biome specific ER simulations were performed using the GFED inventory. The first, ER_{coarse}, was calculated using the vegetation type characterization published in Friedli et al. [37], whereas the second set, ER_{fine}, was obtained following a more detailed characterization methodology as described in the Annex A. Using ER_{av} (leads to Hg emissions from BB of 599.4 ± 104.6 Mg, whereas ER_{coarse} and ER_{fine} give 447.9 ± 81.2 Mg and 301.9 ± 114.0 Mg respectively, see Table 3.2.3. Not only does the emission total change with ER calculation method,

Table 3.2.3: Annual mercury emissions and spatial correlation (R) using the global ER ($ER_{av} = 1.54 \times 10^{-7}$) and biome specific ERs (ER_{coarse} and ER_{fine}), all simulations used the GFED inventory. Average over the 2006–2010 period.

Year	ER_{av}	ER_{coarse}		ER_{fine}	
	Mg	Mg	R	Mg	R
2006	710	502	0.80	481	0.82
2007	624	473	0.97	279	0.58
2008	510	379	0.90	205	0.49
2009	473	348	0.92	208	0.51
2010	683	538	0.97	336	0.66
Average	600	448		302	
Sigma	105	81		114	

but so does interannual variability (from 17% to 38%) and the spatial correlation pattern (see R in Table 3.2.3). Nearly all of the difference is due to the distinction between savanna and tropical forest in Africa. The ER for savanna, at 0.28×10^{-7}

is less than 20% of ER_{av} (1.54×10^{-7}), and even though the tropical forest ER is higher than the global average (2.05×10^{-7}) this does not compensate for the decrease in Hg emissions from the vast savanna regions of Africa. In comparison the higher ratio of forest to savanna in South America means that overall there is little change in the total Hg emissions for this region. The simulations using the more detailed ER estimates show a decreased spatial correlation for Hg deposition with respect to the simulations using an average ER, see Tables 3.2.2, 3.2.5 and 3.2.3. Although the magnitude of Hg emission, and therefore also the magnitude of the Hg deposition flux, is different using the specific ERs, the impact on the geographical distribution of the deposition is limited.

Injection height

The height at which emissions from BB are introduced into the model can have a significant impact on pollutant transport. Some recent studies have shown that boreal fire emissions can be lofted above the boundary layer [58, 123]. A long term study of the CALIOP (Cloud-Aerosol Lidar with Orthogonal Polarization) profiles over South-Western Russia and Eastern Europe for 2006–2008 showed that as much as 50% of the BB plumes were above the boundary layer [8]. A detailed review of injection heights and plume rise models can be found in Ichoku et al. [52]. Simulations were performed in which the emissions were added to different model levels up to approximately 2000 m. Further simulations, one in which the emissions were distributed uniformly throughout the lower levels of the model, and a second with a prescribed latitudinally dependent vertical distribution, were performed [30, 132]. Comparing the Hg deposition patterns obtained in these experiments to the base case reveals a very high correlation, $R \approx 1$, see table 3.2.5. The atmospheric lifetime of $Hg^{\circ}_{(g)}$ is the main reason for this lack of influence of the emission height on the simulated deposition fields. Similar results have been obtained in studies of CO plumes, where the impact of emission height on atmospheric composition is significant locally, and only has a minor influence on regions distant from the plume source [44, 54, 60].

Sensitivity to oxidation mechanism

As mentioned in Section 3.1.2 the precise mechanism by which $Hg^{\circ}_{(g)}$ is oxidized in the atmosphere is not yet certain [51, 113, 114]. Most models opt for a combination of O_3/OH, or alternatively a Br based oxidation mechanism. In either case $Hg^{\circ}_{(g)}$ has an atmospheric lifetime of approximately 8 to 12 months, which is consistent with the observed difference in the hemispherical background concentrations of $Hg^{\circ}_{(g)}$ (roughly 1.7 ng m^{-3} in the Northern Hemisphere and 1.2 in the southern). For 2010 simulations were performed utilizing each oxidation pathway with each BB emission inventory. Further simulations, using fixed atmospheric lifetimes against oxidation of 12 and 6 months were also performed. The agreement maps for the simulations are presented in figure 3.2.10.

Although the number of cells where all the inventories agree that Hg deposition is high does not differ greatly between the different simulations, the distribution of the 'agreement' does. This is particularly true of the tropical Atlantic; using the Br mechanism there is no 'high' deposition area to the west of Africa, however the 'high' deposition region in the North Atlantic reaches Iceland, which it does not in the O_3/OH simulation. Again, in the Br simulation the 'high' deposition area reaches into the Gulf of Alaska, whereas in the O_3/OH simulation the 'high' deposition regions are more closely confined to a relatively narrow latitude band between the tropics, reflecting the distribution of O_3 in the troposphere. The Br simulation does show noticeably more areas where only the GFED inventory predicts high deposition, particularly in the Southern Ocean. This is in part due to the higher southern hemisphere emissions in GFED, but also because the period of the year when biomass burning is most prevalent in South America, July to September, coincides with low tropospheric Br concentrations, so that the emissions are transported much further in this simulation than in the O_3/OH simulation.

The simulations using a fixed atmospheric lifetime for Hg give results that are more similar to the Br mechanism, particularly in the case of the 12 month lifetime. In neither of the two simulations is the high deposition distribution as closely con-

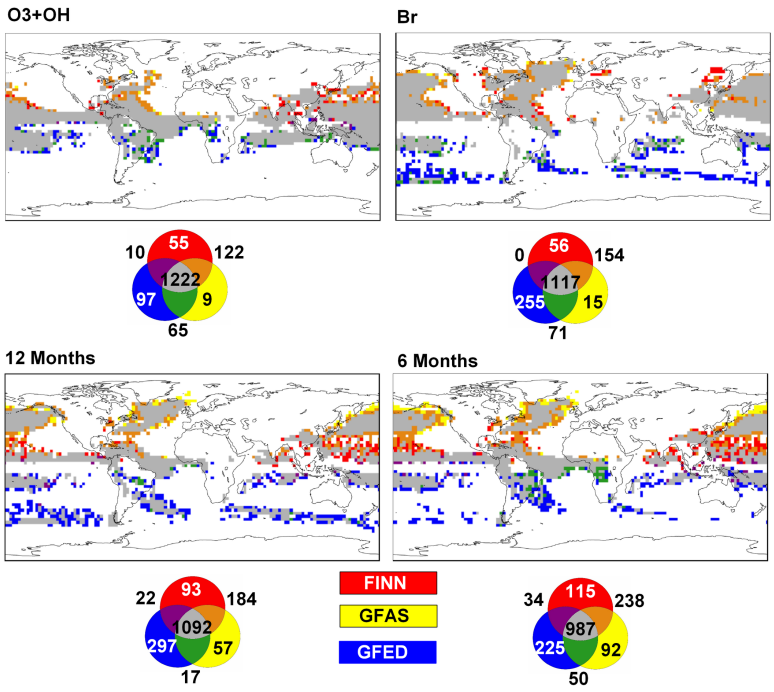

Figure 3.2.10: Agreement maps for Hg deposition exceeding $\mu+\sigma$ for simulations using the Base (O_3+OH) and the Br-based oxidation mechanisms, and fixed Hg^0 lifetimes of 6 and 12 months. The map shows the areas where deposition is $> \mu+\sigma$. Primary colors (red, blue and yellow) represent non-agreement between inventories, green, purple and brown indicate agreement between two of the inventories and gray indicates agreement between all three. The numbers refer to the number of cells in common between the simulations using the different inventories (The whole globe is represented by 8192 cells)

fined to the area between the tropics as in the O_3/OH case. In all the simulations most Hg deposition from BB emissions is deposited to the oceans. Clearly more monitoring sites in the Tropics would help immensely to understand more fully the importance of BB Hg emissions on oceanic Hg deposition. Table 3.2.4 summarises the simulated Hg deposition to the world's ocean basins. The table in-

Table 3.2.4: Annual mercury deposition (Mg) to the Oceans.
The Arctic has been defined as the region north of 66°N, and the Southern Ocean as south of 60°S. The 2010 O_3/OH and Br simulations included, anthropogenic, natural and BB emissions, hence the higher deposition totals.

Year	FINN	GFAS	GFED	FINN	GFAS	GFED	FINN	GFAS	GFED	FINN	GFAS	GFED
	North Atlantic			**South Atlantic**			**North Pacific**			**South Pacific**		
2006	80	71	70	51	45	50	158	137	137	139	123	135
2007	74	68	63	47	45	48	144	131	124	131	124	131
2008	71	72	59	41	41	37	136	135	111	113	111	100
2009	74	64	52	42	38	34	146	125	102	118	106	94
2010	84	65	73	50	40	50	164	122	142	142	111	139
Base	1206	1181	1193	686	671	685	2380	2326	2353	1984	1940	1979
Br	-	-	1112	-	-	733	-	-	2242	-	-	2022
	Indian Ocean			**Mediterranean**			**Arctic Ocean**			**Southern Ocean**		
2006	91	81	89	2.1	1.9	1.8	10	9.9	8.8	6.1	5.4	5.9
2007	82	77	80	2.0	1.8	1.6	10	9.5	8.0	5.6	5.2	5.6
2008	72	70	62	2.0	2.1	1.6	10	12	8.6	4.6	4.6	4.2
2009	76	67	59	2.1	1.8	1.4	11	10	7.3	4.9	4.4	4.0
2010	87	67	82	2.3	1.8	1.9	12	9.6	10	6.0	4.8	6.1
Base	1232	1205	1226	40	40	40	197	193	194	89	87	89
Br	-	-	1141	-	-	42	-	-	242	-	-	184

6

cludes the simulated deposition totals calculated using full atmospheric emissions (natural, anthropogenic and BB) for the two oxidation mechanisms for 2010.

Uncertainty in the Deposition fields

The Hg deposition fields obtained in this study vary and it is not immediately clear where and to what extent the results agree. In order to examine the 'ensemble' of results, rather than just averaging the full set of simulations, the model output has been tested against the Base run (GFED, O_3/OH, global ER, year 2010) to ascertain the probability that the deposition fields belong to the same distribution.

This then permits those results which differ the most to be identified. This form of 'inspected' ensemble was recently described by Solazzo and Galmarini [104] for a multi-model ensemble. The non-parametric Kolmogorov-Smirnov two-sample test has been used to examine the results of the sensitivity tests performed using the GFED inventory. The test was repeated with the model output obtained using the FINN and GFAS inventories with the O_3/OH and Br oxidation mechanisms and with the 12 month pseudo-oxidation approach. The results of the test are shown in Table 3.2.5. A value of $Prob_{KS-test} \leq 0.05$ indicates that it is improbable that the simulated Hg deposition fields belong to the same distribution. The height at

Table 3.2.5: Correlations and probabilities that the sensitivity run Hg deposition fields belong to the same distribution as the GFED 2010 simulation deposition field, and comparison with FINN and GFAS

		12 m		O_3+OH		Br	
RUN	Assessment	R	P_{KS}	R	P_{KS}	R	P_{KS}
Emiss.	Z dist.	1.00	1.00	1.00	1.00	1.00	1.00
Emiss.	Z Inj. lev	1.00	1.00	1.00	1.00	1.00	1.00
Ox. mech.	O_3/OH	0.91	<0.05	–	–	0.81	<0.05
Ox. mech.	Br	0.96	<0.05	0.81	<0.05	–	–
Lifetime Hg(0)	12 m	–	–	0.91	<0.05	0.96	<0.05
Lifetime Hg(0)	6 m	0.99	0.41	0.97	<0.05	0.89	<0.05
ER	ER_{coarse}	1.00	0.99	1.00	1.00	1.00	1.00
ER	ER_{fine}	0.99	0.52	1.00	0.17	1.00	0.10
	FINN 2010	0.97	<0.05	1.00	<0.05	0.98	<0.05
	GFAS 2010	0.97	<0.05	1.00	0.08	0.99	0.09

which the emissions are introduced into the model, and the first Enhancement Ratio variation (ER_{coarse}) make very little difference to the output results. The most important factors influencing the output fields are the inventory and the oxidation mechanism. The second variation of the Enhancement Ratio (ER_{fine}) described in Section 3.2.4 also results in noticeably different deposition fields even if the hypothesis that the model output belongs to the same distribution as the Base case cannot be rejected, $Prob_{KS-test}$ = 0.17 and 0.10, with the O_3/OH and Br oxida-

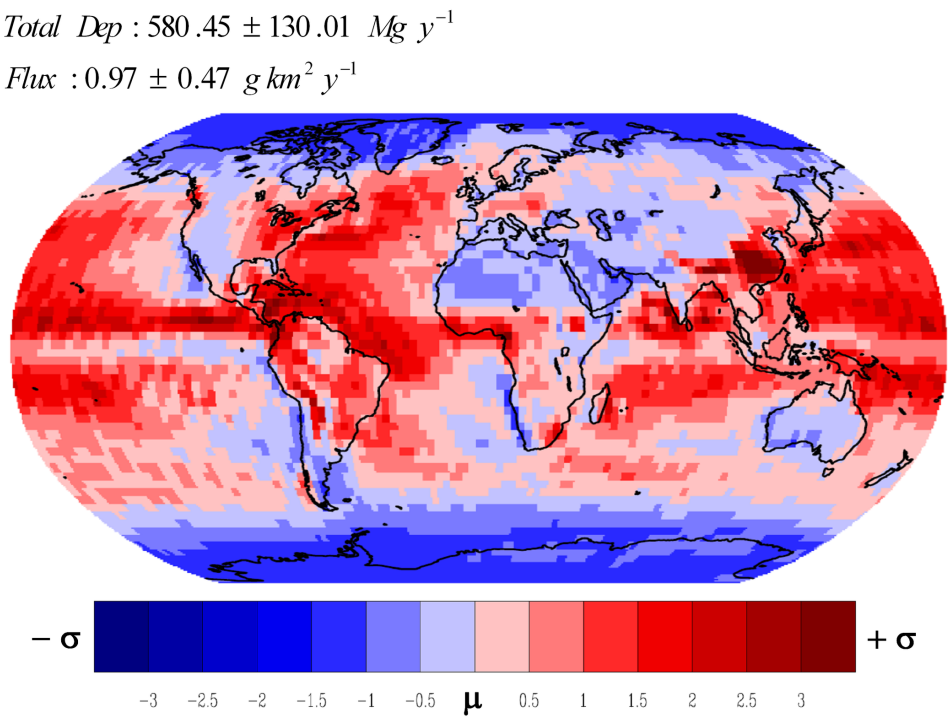

Figure 3.2.11: Geographical distribution of the probability density function of the total Hg deposition obtained from an inspected ensemble of simulations for the year 2010. Total deposition is illustrated in terms of the average (μ) and standard deviation σ of the ensemble.

tion mechanisms respectively. This is also true for the GFAS inventory $Prob_{KS-test}$ = 0.08 and 0.09, however these values indicate that the probability of belonging to the same distribution is low. The results from the three inventories, and also the ER2 sensitivity run, with both the O_3/OH and Br oxidation mechanisms have therefore been averaged to obtain an 'ensemble' deposition field, which is illustrated in figure 3.2.11. The figure makes it evident that however much the simulated deposition fields differ, the regions most influenced by Hg deposition from biomass burning are the tropical areas of the oceans, the North Atlantic and the North Pacific.

3.3 Discussion

Just over 75% of the Hg released by BB is deposited to the world's oceans and seas. As is well known, human exposure to methylmercury (the most toxic form) occurs predominantly through fish consumption. Hg^{II} deposited to the ocean may be reduced and re-emitted from the sea surface, but a part can be methylated in surface or subsurface waters, where it can enter the food web [17, 32, 116]. The maximum deposition fluxes in the individual oceanic regions, are very similar for all the BB inventories. From the results obtained from the five year runs it was found that the North Atlantic has the highest peak deposition flux value at 21 g km^{-2}, followed by the North Pacific and Indian Oceans at ≈20 g km^{-2}. The maximum Hg deposition flux in the Arctic reaches 7 g km^{-2}, higher than the Mediterranean (6 g km^{-2}) and the Southern Ocean (3 g km^{-2}). The total calculated emissions of Hg from BB are similar for all three inventories used in this study, although there are differences in their geographical distribution. GFED has a higher proportion of emissions in the southern hemisphere (Figure 3.2.4c) in comparison to the other two inventories and this is also visible in the deposition fields ((Figure 3.2.4d). However the lifetime of $Hg^{\circ}_{(g)}$ is such that the differences in the spatial distribution of the emissions is far less evident in the simulated deposition fields. GFED is a slight exception as the distribution, relatively to the other two inventories has a higher proportion of emissions in the southern hemisphere (Figure 3.2.4c) this is visible also in the deposition fields (Figure 3.2.4d). One effect of BB is to emit Hg from lower latitudes for eventual deposition at higher latitudes, in both hemispheres. The presence of higher latitude boreal forests in the Northern Hemisphere does mean that the Arctic is more impacted than the Antarctic by Hg deposition resulting from BB. The highest Hg deposition fluxes are found in the North Atlantic, while the the greatest total Hg deposition is to the North Pacific.

The oxidation mechanism and the choice of emission inventory have the greatest influence on the spatial distribution of the Hg deposition fields. The factor which most influences the total calculated Hg emission from BB is the enhancement ratio. More biome specific Hg/CO enhancement ratios are needed to better

constrain the magnitude of Hg emissions from BB. In order to build a bottom-up inventory it would be necessary to perform measurements of Hg and CO released by BB and also ideally to distinguish between the same biomes on different continents. As the number of Hg monitoring sites around the world increases, intermittent information will become more abundant as stations will at times be downwind of BB plumes, however a more targeted approach addressing, tropical, savanna and boreal ecosystems would be far better. Biomass burning will continue to play a role in the cycling of Hg, and legacy Hg particularly, for a long time to come. As the Minamata Convention comes into force and anthropogenic emissions begin to be curbed, the role of BB in cycling Hg from the tropics to higher latitudes, and particularly in transferring Hg from terrestrial reservoirs to the oceans will become more important. Understanding the recycling of legacy Hg is particularly important in the assessment of the response times of ecosystems to changes in anthropogenic emissions, especially should the frequency and scale of BB increase as the climate changes.

4

Hg Deposition Flux from Anthrogenic Activities

Much of the Hg present in the environment today is the result of past anthropogenic activity [12], with coal combustion, metal refining and, periodically, bellic industries all having made a significant impact. Current levels of Hg in the atmosphere and oceans are significantly perturbed with respect to pre-colonial times: the atmospheric burden is estimated to be 300 – 500% higher, and the concentrations in the upper ocean 200% higher [7, 69, 102]. Consequently the reductions in the use and emissions of Hg proposed in the Minamata Convention [1] will take place within a context of the continuous recycling of previously emitted Hg between environmental compartments. Most Hg input into ecosystems is the result of atmospheric deposition, both dry and wet. Hence the atmosphere is

[1] http://www.mercuryconvention.org/

fundamental in distributing Hg, and the lifetime of Hg^0_g of 8–12 months ensures that this occurs on a global scale. To assess the impact of future changes in anthropogenic emissions of Hg on the overall environmental burden, it is important to constrain the uncertainties associated with Hg emissions to and deposition from the atmosphere. In the previous Chapter 3 the impact of the uncertainties in biomass burning inventories on Hg emission and subsequent deposition were investigated. Adopting a similar approach, the influence of the choice of anthropogenic Hg emission inventory used in the model has been investigated. Three global Hg emission inventories are currently freely available, AMAP/UNEP [7], EDGARv4.tox1 [70] and a version of the AMAP/UNEP 2005 inventory [6, 75] which has been adapted for use in the GEOS-Chem model [2] as described in Corbitt et al. [25], based on Streets et al. [109].Due to the differences between the AMAP/UNEP 2005 and 2010 inventories [7], in particular with respect to the relative importance of coal combustion for power generation and artisanal and small scale gold mining (ASGM) this inventory has also been included in the study. The distribution of Hg emissions between Hg^0_g, Hg^{II}_g and Hg^P, and also emission height differ between the inventories, and as these characteristics influence Hg deposition patterns their impact has also been investigated. Most human exposure to Hg is through the consumption of fish and therefore the differences in the calculated deposition fluxes to the oceans is assessed. It goes without saying that a wider monitoring network for Hg in precipitation would be beneficial to constrain uncertainties in Hg fluxes, and thus also in emissions. Ultimately better constrained models will lead to better estimates of the time scales of environmental response times to future reductions in anthropogenic Hg emissions.

[2] http://geos-chem.org/

4.1 Methodology

4.1.1 Anthropogenic emission inventories

The details of the three principal inventories used, which are referred to as AMAP2010, EDGAR and STREETS hereafter, have been described in detail in the literature [7, 25, 70, 109]. A summary of the major characteristics of the inventories can be found in table 4.1.1, as can be seen they are broadly similar in most respects. Emission height and speciation have been identified as being important parameters in regional modelling studies, but on a global scale they tend to be less so. The differences in Hg speciation can lead to marked differences in local concentrations of Hg^{II}_g and Hg^P particularly in regional models [16]. In global models where the spatial resolution is more coarse the effect is less noticeable, and will depend on the height distribution employed to partition the emissions between model levels, see section 4.1.4. Only the AMAP2010 inventory gives a vertical distribution for the emissions, they are divided into three height ranges and differentiate between Hg^0_g, Hg^{II}_g and Hg^P. The EDGAR inventory provides speciated emissions divided into sectors identified using standard IPCC codes (see [3], and therefore a height distribution can be inferred, see Annex B. The spatial distribution of the emission inventories does differ as can be seen in figure 4.1.1. One of the major reasons for this is the uncertainty involved in the estimation of emissions from ASGM. The AMAP/UNEP 2005 inventory (on which the Streets inventory is based), included emissions from ASGM but used the "distribution mask" from large scale gold production to distribute the emissions. The AMAP2010 inventory

Table 4.1.1: Emission inventory characteristics in Mg

Inventory	Reference year	Resolution	Total Hg	Hg^0_g	Hg^{II}_g	Hg^P
AMAP	2010	0.5 by 0.5°	1960	81%	14%	4%
EDGAR	2008	0.1 by 0.1°	1287	72%	22%	6%
STREETS	2005	1 by 1°	1900	58%	combined 42%	

[3] http://edgar.jrc.ec.europa.eu/faq6.php

uses a more realistic distribution as does EDGAR, and this results in proportionally increased emissions in the Tropics and the Southern Hemisphere, as can be seen in the side panel of figure 4.1.1.

4.1.2 Model set-up and Simulations

The global Hg chemical transport model ECHMERIT [28, 55] is based on the fifth generation General Circulation Model ECHAM5 [84, 85]. ECHMERIT was run using T42 horizontal resolution (roughly 2.8° by 2.8° at the equator) and 19 vertical levels up to 10 hPa. The AMAP2010 inventory was first converted to NetCDF and then all the emission inventories were interpolated onto the ECHMERIT grid using the mass conserving Climate Data Operators (CDO) remapping tool [5]. A first set of simulations was performed which included all emissions, anthropogenic, marine and also from biomass burning. Monthly biomass burning mercury emissions calculated using the FINNv1 inventory [130] and a globally averaged emission ratio [37], as described in De Simone et al. [29]. Emissions from oceans were calculated on-line in the model, as described in De Simone et al. [28], and prompt re-emission of deposited Hg was included as in Selin et al. [99]. A spin-up period of 4 years was employed and the results from the fifth year, 2010, were used for this study. As there remains some uncertainty concerning atmospheric Hg oxidation pathways [51, 113, 114], simulations were run using an O_3/OH oxidation scheme and an alternative Br based oxidation mechanism. Oxidant fields were imported from the Mozart model [35] for the O_3/OH simulations, and from p-Tomcat [134, 135] for the Br/BrO fields. The results of these simulations were used for comparison with observed atmospheric Hg concentrations and wet deposition flux measurements.

4.1.3 Anthropogenic emission only simulations

To evaluate the Hg deposition which results directly from human activities, further simulations were performed which included only anthropogenic emissions,

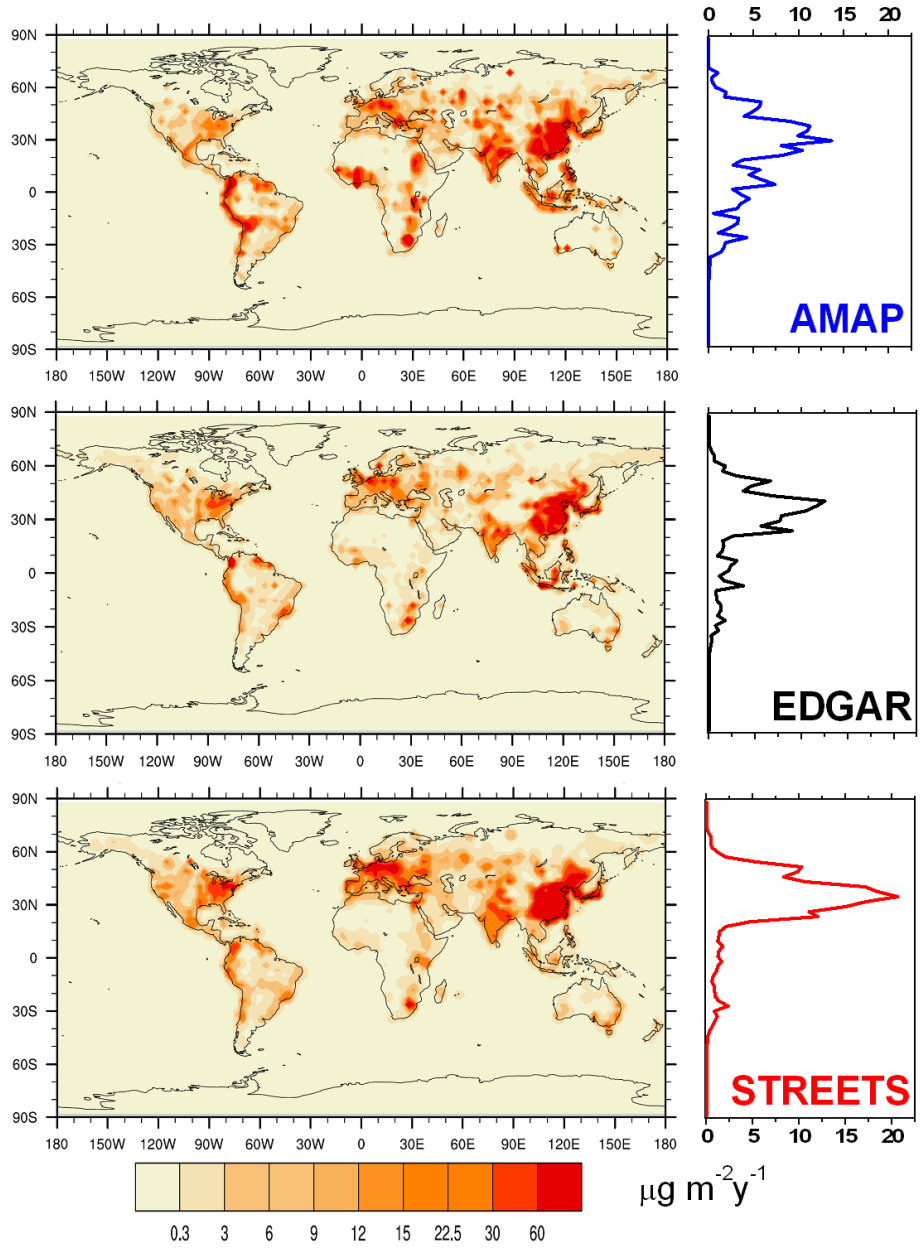

Figure 4.1.1: Geographical distribution of annual mercury emissions and the latitudinal vertical profile of the increase in atmospheric Hg concentration resulting from anthropogenic emissions as estimated by STREETS, EDGAR and AMAP inventories.

and in which the prompt re-emission mechanism was not used. Simulations were performed using each of the three inventories using their original height distribution and employing each of the oxidation mechanisms. Further simulations one set assuming all the emissions were emitted to the first model level and one with the emissions dispersed uniformly throughout the the boundary layer (BL), using the O_3/OH oxidation mechanism. The height distribution of each inventory was applied to the other inventories for a further set of simulations with the O_3/OH oxidation mechanism. The height distributions are described in section 4.1.4 and the details of the simulations are summarised in table 4.1.2. Further simulations

Table 4.1.2: Simulations performed with ECHMERIT. The last column indicates the simulations included in the final ensemble 4.2.4.

Inventory used	Height distribution	Ox. Mechanism	Focus	Final Ensemble
AMAP	NATIVE AMAP	O3-OH	Inventory	yes
AMAP	1st level	O3-OH	Level	
AMAP	3th level	O3-OH	Level	
AMAP	uniform PBL	O3-OH	Level	
AMAP	SNAP like	O3-OH	Level	
AMAP	NATIVE AMAP	O3-OH	Spec. All Hgo	yes
AMAP	NATIVE AMAP	O3-OH	Spec. All Hg2	
AMAP	NATIVE AMAP	Fixed 12	Oxidation	yes
AMAP	NATIVE AMAP	Fixed 6	Oxidation	
AMAP	NATIVE AMAP	BR Tomcat-1	Oxid. Br set	yes
EDGAR	NATIVE EDGAR (SNAP)	O3-OH	Inventory	yes
EDGAR	1st level	O3-OH	Level	
EDGAR	uniform PBL	O3-OH	Level	
EDGAR	AMAP like	O3-OH	Level	
EDGAR	NATIVE EDGAR	BR Tomcat-1	Oxid. Br set	yes
STREETS	NATIVE STREETS (PBL)	O3-OH	Inventory	yes
STREETS	1st level	O3-OH	Level	
STREETS	AMAP like	O3-OH	Level	
STREETS	SNAP like	O3-OH	Level	
STREETS	NATIVE STREETS	BR Tomcat-1	Oxid. Br set	yes
AMAP-2005	NATIVE AMAP	O3-OH	Inventory	

were performed using assuming a fixed lifetime against oxidation ("pseudo" oxidation mechanism), by varying the native inventory emissions height distributions as well as the native speciation.

4.1.4 Height Distribution of emissions

For Hg sources that predominantly emit elemental Hg, ($Hg^{0}_{(g)}$) such asbiomass burning, the vertical distribution of the emissions in the model levels does not have a significant effect on the eventual Hg deposition pattern, see De Simone et al. [29]. For shorter live Hg species, $Hg^{II}_{(g)}$ and $Hg^{II}_{(p)}$, the model level into which they are placed will influence deposition. The three inventories used here all take different approaches, the AMAP2010 gives three height ranges, up to 50 m, between 50 and 150 m and above 150 m. The EDGAR inventory provides emissions divided into sectors following the Intergovernmental Panel on Climate Change (IPPC) identification code [4], without specific information on the height distribution. The IPCC sectors were mapped to Standardized Nomenclature for Air Pollutants (SNAP) categories and the emission height table used in the Unified EMEP model [100] was used [5]. The STREETS inventory gives no information regarding emission height or emission sector, they are therefore distributed throughout the BL as in GEOS-Chem. The distributions above are referred to as the 'native' distributions. In addition simulations in which different distributions were imposed were performed, in order to evaluate the impact of the vertical emission distribution on the final deposition fields.

4.2 Results

4.2.1 Emission inventory comparison

Figure 4.1.1 shows the geographical distribution and the latitudinal profile of the total anthropogenic Hg emissions from the AMAP2010, EDGAR and STREETS inventories. The total annual Hg emission is similar in the AMAP2010 and STREETS inventories at around 1900 Mg, whereas the EDGAR inventory has a noticelably lower total of 1300 Mg. However the uncertainty associated with the emission totals, in the case of AMAP2010, emissions are estimated to be between 1010

[4] http://edgar.jrc.ec.europa.eu/faq6.php
[5] http://www.emep.int/UniDoc/node7.html

and 4070 Mg annually, meaning that the EDGAR total is well within the range of uncertainty [70]. The geographical locations of the emissions are similar among the inventories, with the greatest sources distributed over the industrialised areas of North America, Europe, South and East Asia. The most notable difference is the higher emissions in the AMAP2010 inventory at tropical latitudes in Africa and western South America. This difference is the direct result of the revised estimation of emissions due to ASGM in this inventory, which are estimated to be higher than those from coal combustion [7]. The latitudinal profiles in the right-hand panel of Figure 4.1.1 show the differences between the three inventories clearly. The AMAP2010 and EDGAR inventories have broader distributions, the AMAP2010 inventory having higher emissions in equatorial and tropical regions due to its higher estimation of emissions from ASGM. The STREETS inventory has almost all emissions in the northern hemisphere centred around 40°N.

The correlation (r) between the latitudinal profiles of the inventories is ≥ 0.86 in all cases, however the agreement map in figure 4.2.1 shows how much they differ in terms of the location of areas of higher emissions. Figure 4.2.1 indicates the areas in the world where the inventories have emissions greater than $\mu + \sigma$ (average + the standard deviation). With the exception of the industrial regions of the northern hemisphere the three inventories agree on the areas of highest emissions in very few instances.

4.2.2 Model Performance

The results from simulations including all emissions for the year 2010 were compared to available measurement data. A statistical summary of the comparison for gas phase Hg and for Hg wet deposition from the main runs can be found in table 4.2.1. The comparison between the different model runs and the observations are reasonable and similar for TGM, the comparison with wet deposition is less good and there is a greater variation in the quality of the comparison. For TGM, using the AMAP2010,EDGAR or STREETS inventories does not lead to statistically

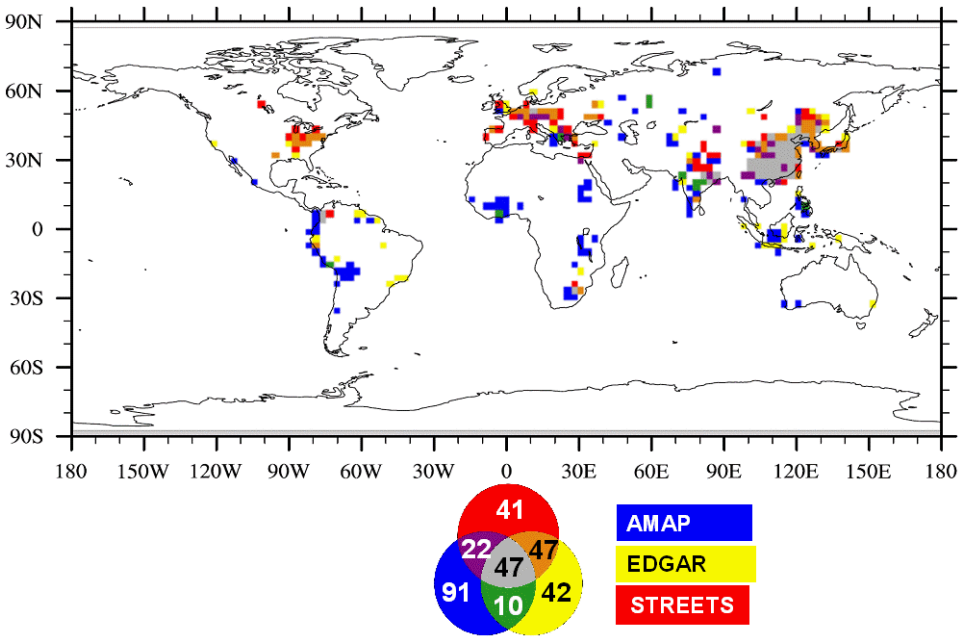

Figure 4.2.1: Agreement map of Total Hg emissions for the AMAP2010, EDGAR and STREETS inventories. The map shows the areas where the emissions are $> \mu+\sigma$. Primary colors (red, blue and yellow) represent non-agreement between inventories, green, purple and brown indicate agreement between two of the inventories and gray indicates agreement between all three. The numbers refer to the number of model cells in common between the different inventories, the whole globe is represented by 8192 cells.

Table 4.2.1: Comparison of the native height inventory simulations varying Oxidation Mechanism with global observations for 2010

		TGM				Wet Deposition			
		Regress. param.		Stats		Regress. param.		Stats	
Inventory	Oxid.	Intercept	Slope	r	NRMSE	Intercept	slope	r	NRMSE
AMAP2010	O_3-OH	0.4	0.85	0.86	13.08	4.53	0.23	0.23	12.82
EDGAR	O_3-OH	0.32	0.83	0.83	14.27	4.64	0.18	0.18	12.12
STREETS	O_3-OH	0.24	0.96	0.87	14.33	5.35	0.27	0.21	16.58
AMAP05	O_3-OH	0.09	1.12	0.85	17.96	4.67	0.27	0.24	14.48
AMAP2010	Br pT.	-0.2	0.82	0.83	14.69	7.11	0.08	0.07	15.10
EDGAR	Br pT.	-0.06	0.82	0.79	16.73	6.86	0.06	0.06	14.28
STREETS	Br pT.	-0.13	0.94	0.84	15.44	7.82	0.15	0.11	18.43
AMAP2010	Fix. 12m	0.42	0.85	0.85	13.86	4.57	0.16	0.17	12.10

significant ($a = 0.05$) different regression slopes even when using the different oxidation mechanisms. For the wet deposition the results are worse when using the Br oxidation mechanism.

4.2.3 Modelled Hg Deposition

Latitudinal variation

While the latitudinal profile of the emissions shows separate peaks and two cut-offs at the latitudinal limits of significant industrial human activity (45°S and 75°N) (Fig. 4.2.2(a)), the profile of the total deposition never reaches zero at any latitude (Fig. 4.2.2(b) and 4.2.2(c).The latitudinal profiles of Hg deposition due to anthropogenic emissions are very similar in the Northern Hemisphere (NH) above 30°N, with a broad peak centred around the latitude of the major NH industrial regions (≈40°N). This is the case for both the O_3 + OH and the Br oxidation mechanisms, and also whether considering soley anthropogenic or total Hg emissions.

South of 30°N the oxidation mechanism used in the simulations has a marked influence on the deposition profile, as can be seen in figures 4.2.2(b) and (c). The O_3+OH simualtions give peaks in deposition almost equal to the NH industrial region peak just above and below the equator (all sources, the peaks are less pronounced in the anthropogenic only simulations) with a fairly steady decrease southwards towards the Antarctic region. The deposition profile in the SH in the Br simulation differs because the Br concentration profile is more constant with latitude when compared to the O_3+OH concentration, and in particular does not peak around the equator. The broad peak in the simulation with all sources is a result of the combination of marine evasion of Hg and significant Br concentrations between roughly 15 and 60°S. The latitudinal deposition profiles when only anthropogenic Hg emissions are considered begin to differ below roughly 40°N. Below this latitude the AMAP2010 inventory predicts roughly twice the deposition flux compared to the simulations using the STREETS inventory, with the EDGAR inventory resulting in fluxes between the two, irrespective of the oxida-

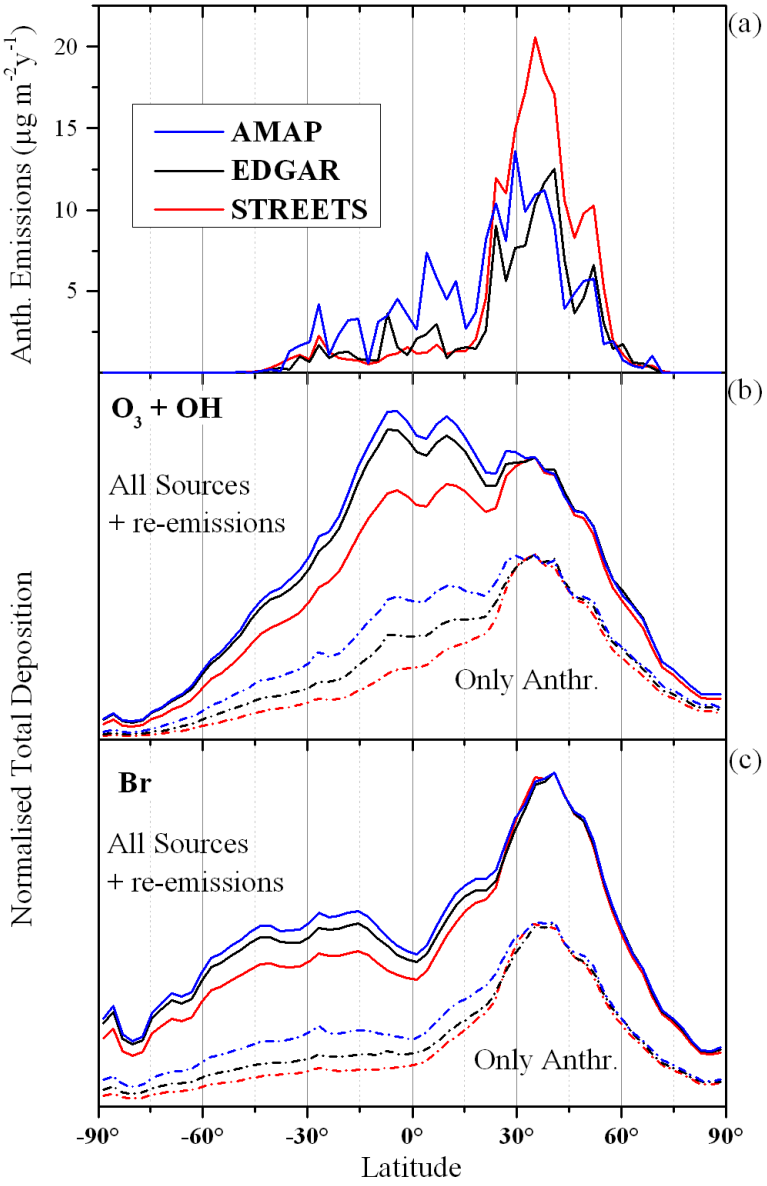

Figure 4.2.2: Latitudinal profiles of mercury emissions (a) and normalised total deposition that result from model runs adopting O_3 + OH (b) and Bromine (c) driven oxidation mechanism for the different inventories. Panels (a) and (b) reports deposition obtained by including all emission sources (plus re-emissions) and only anthropogenic emissions. Deposition profiles are not in scale.

tion mechanism employed. The simulations using the O_3+OH mechanism however simulate proportionally higher deposition south of 40°N. The differences in the latitudinal profiles when all Hg emissions sources are included highlight even more markedly the influence of the oxidation mechanism used in the simulations. Using the O_3+OH mechanism gives results with peaks either side of the equator, figure 4.2.2(b), in the figure the deposition profiles have been normalise to the value of the peak at 35°N which coincides with the peak in the anthropogenic emission profiles. These peaks are higher than the deposition peak at 40°N in the case of the AMAP2010 and EDGAR inventories and only slightly lower using the STREETS inventory. By comparison in the simulations using the Br oxidation mechanism the highest deposition south of the equator is between 45 and 60% of the NH peak deposition value. The case for the expansion of monitoring Hg in precipitation to cover equatorial and tropical regions is clear, and not only to quantify the impact that Hg deposition has on ecosystems in this region. Combined with the ongoing monitoring in North America, Europe and China, data from the tropics would also give an insight into the atmospheric oxidation mechanisms which determine the atmospheric cycle of Hg. To illustrate this point figure 4.2.3 shows the simulated latitudinal distribution of wet deposition using the different inventories and the two oxidation mechanisms. Notwithstanding the differences in the inventories the profiles make it quite clear that wet deposition fluxes would be expected to be roughly similar in the tropics and NH if Br is globally responsible for atmospheric Hg^0_g oxidation. If it is the case that O_3+OH are the major oxidants then the Hg wet deposition flux would be roughly twice as high in the tropics than in northern mid-latitudes.

Geographical distribution

The spatial distribution of the simulated total Hg deposition flux is shown in figure 4.2.4 for the simulations including all the emissions, the same maps for the anthropogenic emissions only simulations can be found in figure 4.2.5. The differ-

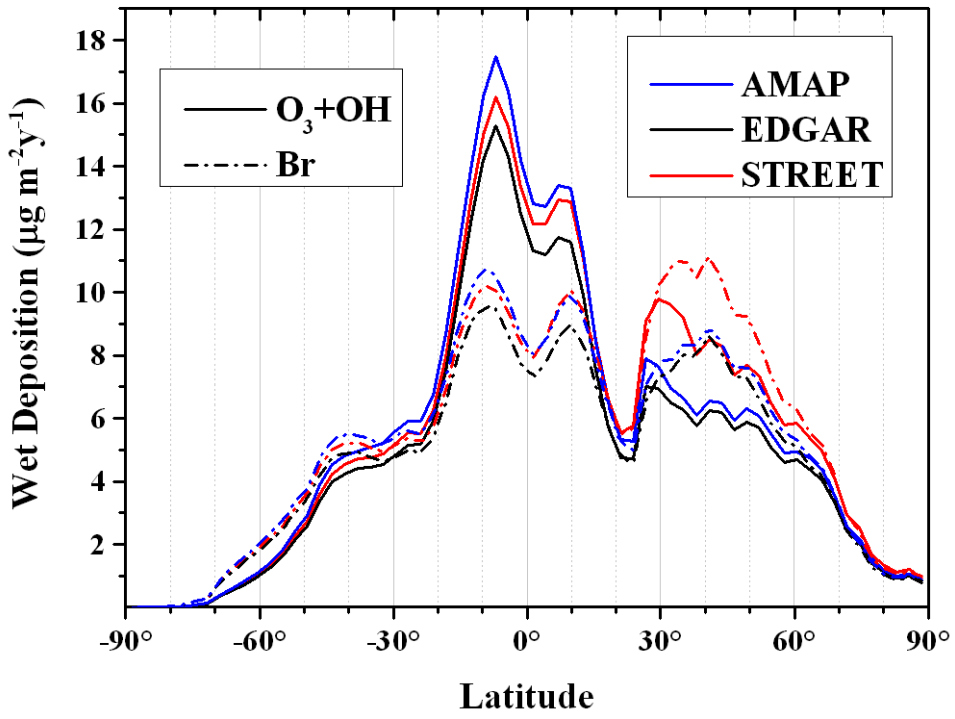

Figure 4.2.3: The latitudinal profile of the simulated wet deposition flux using the three inventories and the both atmospheric oxidation mechanisms

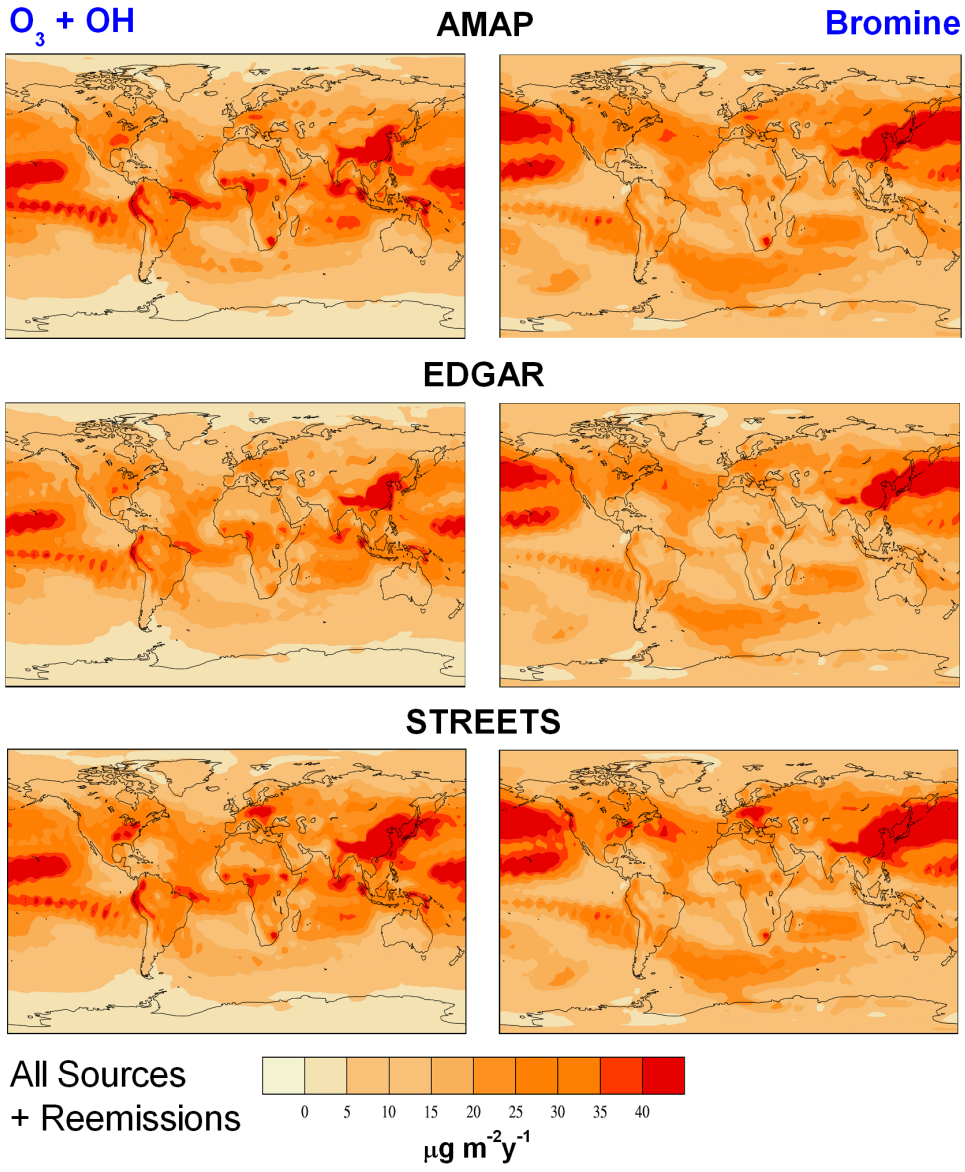

Figure 4.2.4: Geographical distribution of the total mercury deposition (wet + dry) that result from model runs including all sources, for the three inventories and the two oxidation mechanisms.

ences between the inventories are limited, using the STREETS inventory produces higher deposition in Europe, while overall the results using the EDGAR inventory are generally lower everywhere due to the lower total emission estimate. The STREETS inventory also results in somewhat lower deposition in the SH generally. The major differences in the results are a result of the choice of the oxidation mechanism. In particular the simulations with Br as the oxidant have distinctly higher deposition fluxes over the Northern Pacific and somewhat higher over the North Atlantic. The deposition to the equatorial Pacific is however in the Br simulations compared to the O_3+OH simulations. The simulated fluxes to the ocean basins is discussed further in the following section, 4.2.4. The agreement maps in figure 4.2.6 are used to highlight the similarities and differences in the spatial distribution of the regions of high Hg deposition, defined here as greater than the average plus one standard deviation ($> \mu+\sigma$). The primary colours highlight those areas where only one of the inventories simulated fluxes greater than $\mu+\sigma$, whereas the grey areas indicate the regions where the results of the simulations with all three inventories predict particularly high Hg deposition. In the simulations including only the anthropogenic emissions the AMAP2010 inventory shows more regions where only it predicts high deposition, and these are mostly in the equatorial region. In the simulations with either oxidation mechanism there are regions in which all the inventories agree, East Asia, Europe and the Eastern USA. However while both mechanisms predict high deposition over the nort-west Pacific this region extends to the western Pacific in the Br simulations but not in the O_3+OH simulations. Considering all Hg emissions leads to generally broader agreement, with the exception of the STREETS inventory which gives higher deposition in the NH compared to the other two inventories.The AMAP2010 and EDGAR inventories predict higher deposition in the southern Indian Ocean, the the far south Atlantic and the western south Pacific than does the STREETS inventory.

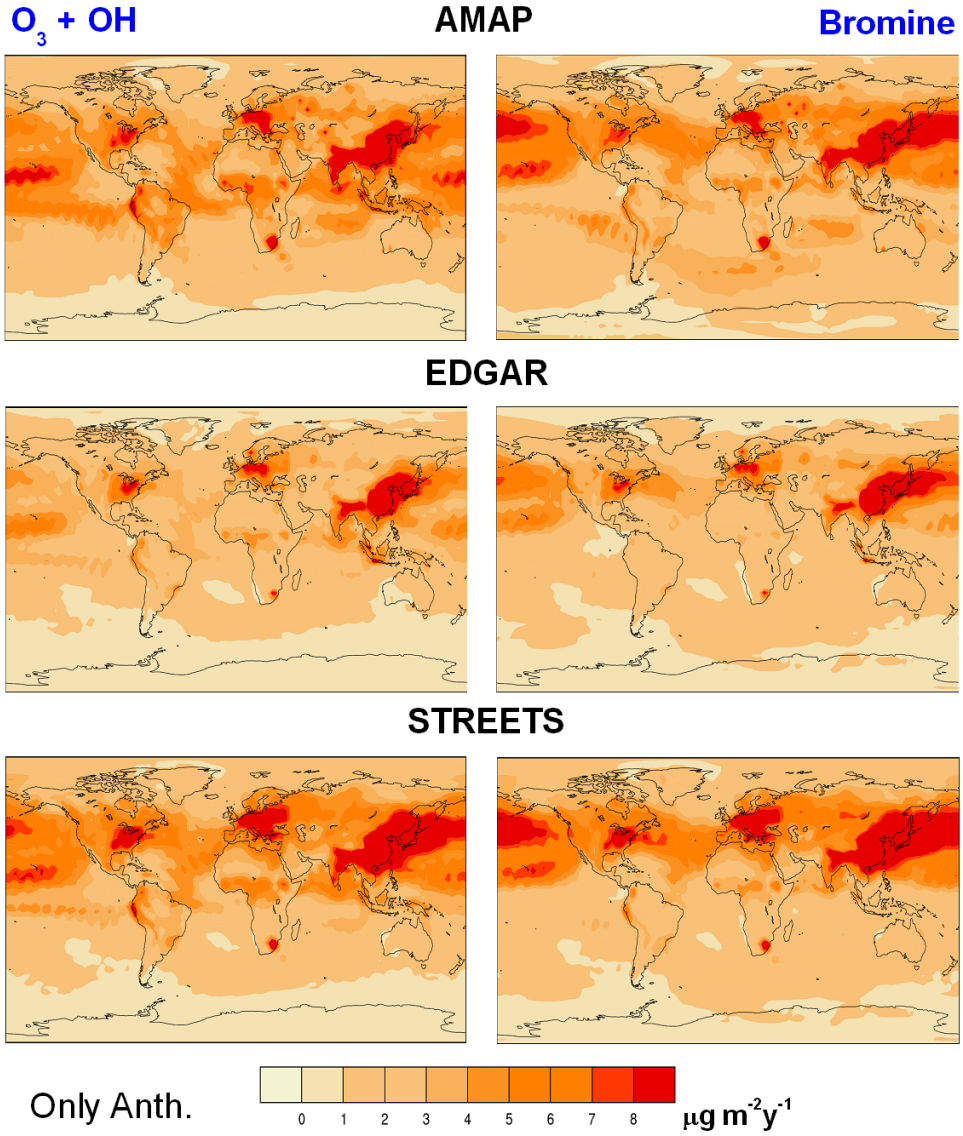

Figure 4.2.5: Geographical distribution of the total mercury deposition (wet + dry) that result from model runs including only anthropogenic emission sources for the three inventories and the two oxidation mechanisms.

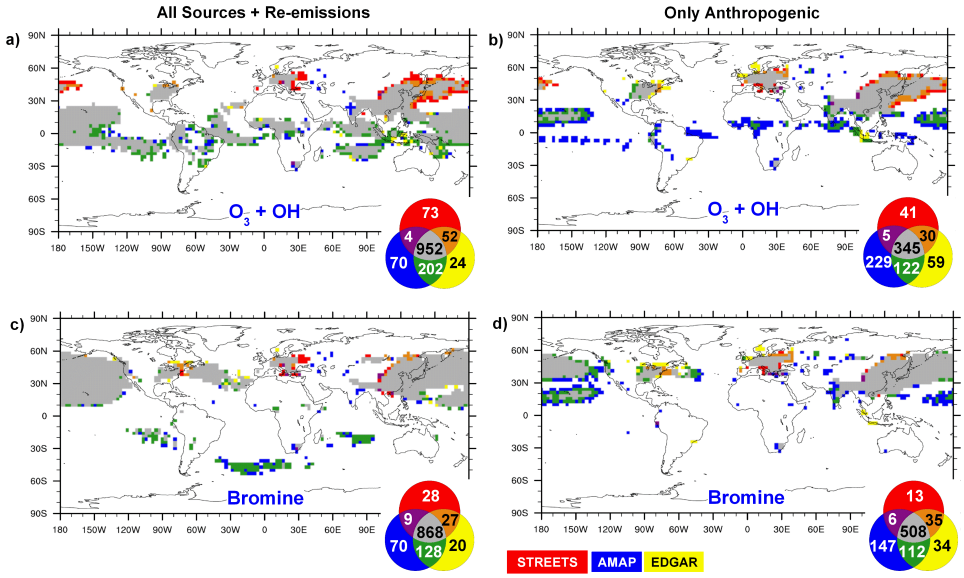

Figure 4.2.6: Agreement maps of Hg deposition fields obtained from runs considering STREETS, EDGAR and AMAP inventories and including all emission sources plus re-emissions (a and c) and only anthropogenic emissions (b and d). Maps are computed for both oxidation mechanism adopted: Bromine (c and d) and $OH^{+}O_3$ (a and b). The maps show the areas where deposition is $> \mu+\sigma$.

4.2.4 Uncertainty and Impact Assessment

The emission inventory and oxidation mechanism used in the simulations have the most influence on the calculated Hg deposition fields. However the speciation of the emissions and the vertical distribution of the emissions in the model also have an influence even if it is less marked. In order to obtain an estimate of the impact current anthropogenic emissions have on the HG deposition flux the results from a number of of the simulations were combined in an 'ensemble'. To avoid redundancy of information within the ensemble [29, 104], the modelled deposition fields were tested to see how well correlated they were among themselves. The horizontal pattern correlation method [89, 90] was used to ascertain the probability that the deposition fields belong to the same distribution, by making use of the non-parametric Kolmogorov-Smirnov two-sample test. The simulations used to construct the ensemble are indicated in Table 4.1.2. The test showed that the vertical distribution of the emissions resulted in only differences in the modelled deposition fields and therefore these simulations were excluded from the ensemble. As seen in a previous study of Hg emissions from biomass burning [29] the long atmospheric lifetime of $Hg^{\circ}_{(g)}$ tend to neutralise the effects of the initial injection height of emissions. The results from each of the inventories using the O_3/OH and Br oxidation mechanisms were included in the ensemble, as were the results from the simulation using the AMAP2005 inventory and the simulation in which $Hg^{\circ}_{(g)}$ was assumed to habe a fixed lifetime of 12 months. The 'ensemble' deposition field of the anthropogenic emission only simulations is shown in the upper panel of the figure 4.2.7. The upper panel in figure 4.2.7 clearly shows that the major imact from anthropogenic emissions is deposition downwind of the major source regions, and is particularly significant over East Asia, and the northern Pacific and Atlantic oceans. The lower panel of figure 4.2.7 compares the anthropogenic emission only ensemble with the same same simulations including all emission sources as well as re-emissions. It shows that the anthropogenic contribution to Hg deposition in the Tropics is around 15%and reaches 25% over significant areas of the northern hemisphere. Due to the importance of the the Oceans in the Hg cycle

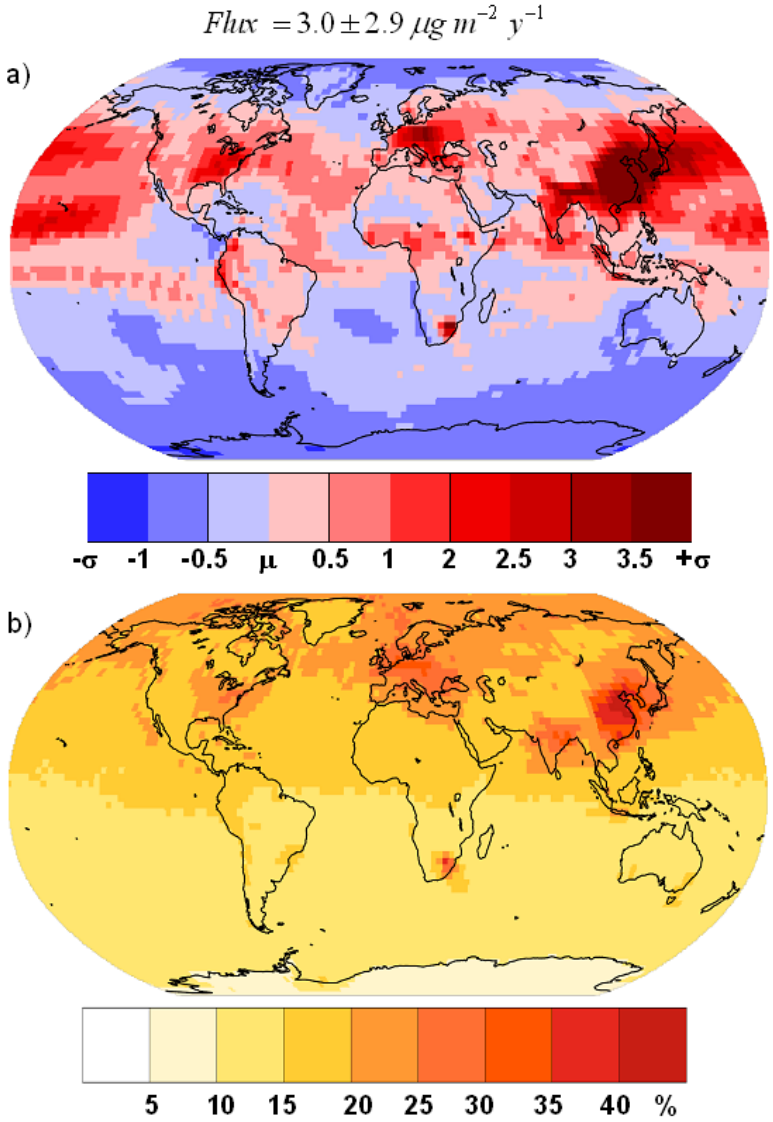

Figure 4.2.7: Geographical distribution of the total Hg deposition from anthropogenic emissions only obtained from an inspected ensemble of simulations for the year 2010 (a) in terms of the average (μ) and standard deviation σ of the ensemble. In (b) such distribution is compared with the ensemble of the same simulations including all other emission source to have a Geographical distribution of the impact.

and because the major human route of Hg exposure is through fish consumption, the deposition to Ocean basins and Seas has been calculated and is summarised in table 3.2.4. In spite of all the uncertainties and unknowns related to the mercury,

Table 4.2.2: Annual mercury deposition (Mg) to the Oceans.
The Arctic has been defined as the region north of 66°N, and the Southern Ocean as south of 60°S. The 2010 O_3/OH and Br simulations included, anthropogenic, natural and BB emissions, hence the higher deposition totals.

O_3/OH				**BASINS**					**%**	
	NA	SA	NP	SP	IN	ME	ANT	AR	LAND	SEA
AMAP	149	104	425	268	190	9	15	34	35	65
EDGAR	112	62	317	160	117	7	8	26	37	63
STREETS	171	74	511	192	147	14	10	43	39	61
Ensemble Full	842	723	2392	1828	1185	44	106	149	30	70
Avg. Impact (%)	17	11	17	11	13	**23**	10	**23**		
Br				**BASINS**					**%**	
	NA	SA	NP	SP	IN	ME	ANT	AR	LAND	SEA
AMAP	158	113	466	249	180	12	38	34	33	67
EDGAR	120	66	352	144	106	9	21	26	35	65
STREETS	181	77	554	172	134	16	23	42	38	62
Ensemble Full	882	774	2574	1660	1084	54	306	195	28	72
Avg. Impact (%)	17	11	18	11	13	**22**	9	17		

the ensemble of simulations suggest that 20-25% of the deposition over the Arctic is due to the anthropogenic activities. The Arctic and the Mediterranean Seas are also the basins where the anthropogenic emission impact is proportionally greatest (table 4.2.2).

4.3 Discussion

EDGAR and AMAP are the inventories with the most similar geographical distributions, and in comparison to the STREETS inventory have a higher proportion of emissions at more southerly latitudes. This is due mostly to the recent re-evaluation of the importance of ASGM as a source of Hg to the atmosphere which

was not so evident in the AMAP 2005 inventory on which STREETS is based. Primary Hg anthropogenic emissions are responsible for up to 23% of the total Hg deposition in some areas where the ecosystem is already under significant anthropogenic and/or climate pressure , such as the Arctic and the Mediterranean Basin. In simulations using either the O_3/OH or Br oxidation schemes roughly two-thirds of anthropogenic emissions are deposited to the world's Oceans. The northern hemisphere is unsurprisingly more influenced by anthropogenic emissions it is also therefore the region which will benefit most from emission reduction. This seems to the case in the North Atlantic where it is believed that the Ocean is already responding to a reduction in riverine inputs which occurred from the 1970s onwards [103]. Although on a global scale the emission height and speciation of Hg emissions have a relatively limited effect on the simulations, they are far more important on a regional scale and should be better constrained for the assessment of local versus regional/hemispheric sources for regions or ecosystems at particular risk. Similarly to the Hg emissions from biomass burning, the oxidation mechanism is of great importance in determining the spatial distribution of Hg deposition. Continued monitoring, particularly at tropical latitudes and particularly of Hg in precipitation have the potential to give greater understanding of the mechanisms driving the global atmospheric Hg cycle.

5

Conclusions

For this thesis an improved version of the global on-line chemical transport model ECHMERIT has been developed and used to investigate and assess a number of the uncertainties related to the atmospheric cycle of Hg.

The total source of Hg to the atmosphere is 11800 $Mg\,y^{-1}$, at the upper end of the range (6200-11200 $Mg\,y^{-1}$) previously estimated by GEOS-Chem [98, 99] and slightly higher than the recent independent estimate of 9700 $Mg\,y^{-1}$ using CAM-Chem [59]. Almost all atmospheric Hg is removed as $Hg^{II}_{(g/aq)}$. Dry deposition of $Hg^{II}_{(g)}$ in ECHMERIT is somewhat greater globally than wet deposition of $Hg^{II}_{(aq)}$, (6500 vs 5300 $Mg\,y^{-1}$). The dry deposition of Hg^0 is negligible (less than 10 $Mg\,y^{-1}$) due to the approach used for modelling the Hg^0 deposition velocity (section 2.6).

The total simulated oceanic flux of Hg^0 to the atmosphere is 5500 $Mg\,yr^{-1}$, at the at the high end of the range of previous estimates (800-5300 $Mg\,yr^{-1}$) and is

comparable with the estimate of Selin et al. [99] of 5000 Mg yr^{-1}. Terrestrial primary emissions from soils and biogenic activities account for 2000 Mg y^{-1} close to other modelling estimates [99]. The prompt recycling of the previously deposited Hg species account for 1400 Mg y^{-1}, greater than previously reported [59, 99], reflecting the greater total deposition.

Recent estimates suggest that approx. 2000 Mg of Hg are released each year from human activities into the atmosphere. EDGAR and AMAP are the anthropogenic emission inventories with the most similar geographical distributions, and in comparison to the STREETS inventory have a higher proportion of emissions at more southerly latitudes. This is due mostly to the recent re-evaluation of the importance of ASGM as a source of Hg to the atmosphere which was not so evident in the AMAP 2005 inventory on which STREETS is based. Primary Hg anthropogenic emissions are responsible for up to 23% of the total Hg deposition in some areas, such as the Arctic and the Mediterranean Basin. Independently of the oxidation mechanism employed (O_3/OH or Br) roughly two-thirds of anthropogenic emissions are deposited to the world's Oceans. The northern hemisphere is unsurprisingly more influenced by anthropogenic emissions it is also therefore the region which will benefit most from emission reduction.

GFED, GFAS and FINN are three recent inventories for Biomass Burning emissions. The total calculated emissions of Hg from BB are similar for all three inventories and account for approx. 600 Mg y^{-1}, although there are differences in their geographical distribution. However the lifetime of $Hg^{\circ}_{(g)}$ is such that the differences in the spatial distribution of the emissions is far less evident in the simulated deposition fields. The GFED inventory is a slight exception as the distribution, relatively to the other two inventories has a higher proportion of emissions in the southern hemisphere, and this is also visible in the deposition fields. Just over 75% of the Hg released by BB is deposited to the world's oceans and seas. The maximum deposition fluxes in the individual oceanic regions, are very similar for all the BB inventories analyzed. One effect of BB is to emit Hg from lower latitudes for eventual deposition at higher latitudes, in both hemispheres. The presence of higher latitude boreal forests in the Northern Hemisphere does mean that the Arctic is

more impacted than the Antarctic by Hg deposition resulting from BB. The highest Hg deposition fluxes are found in the North Atlantic, while the the greatest total Hg deposition is to the North Pacific. The factor which most influences the total calculated Hg emission from BB is the enhancement ratio. More biome specific Hg/CO enhancement ratios are needed to better constrain the magnitude of Hg emissions from BB. The oxidation mechanism is of great importance in determining the spatial distribution of Hg deposition. Continued monitoring, particularly at tropical latitudes and particularly of Hg in precipitation have the potential to give greater understanding of the mechanisms driving the global atmospheric Hg cycle.

A

Methodology to calculate specific Enhancement Ratios

An estimate of specific Enhancement Ratios (ERs) (i.e. on a cell by cell basis) was made considering land cover maps, biome classification and ERs from the literature.

A.1 Land cover

The land cover map used was obtained from the Global Land Cover Facility (GLCF) (University of Maryland, Department of Geography and NASA, [36]). The vegetation classification was obtained from the analysis of the MODIS (MCD12Q1) granules, and identifies 17 land cover classes (excluding water bodies) defined by the International Geosphere Biosphere Programme (IGBP), which includes 11

natural vegetation classes, three developed and mosaicked land classes, and three non-vegetated land classes. The map is on the WGS 1984 coordinate reference system (EPSG: 4326) and dataset boundaries are -180.0° $\leq$ longitude $\leq$ 180.0°; -64.0° $\leq$ latitude $\leq$ 84.0°. The data are at 5' $\times$ 5' resolution, 1776 rows $\times$ 4320 columns and a geographic pixel size of approximately 0.083333°.

A.2 Peat soils

Boreal peatlands are becoming hot spots for mercury emissions as a result of increased burning. Due to their high carbon content they have adsorbed mercury from the atmosphere for millennia [120]. Therefore in preparing the ERs this specific emission source was taken into account using a digital soil map. The Harmonized World Soil Database was obtained from the IIASA soil portal [2]. This map is also on the WGS 1984 coordinate reference system (EPSG: 4326) at 30" $\times$ 30" resolution, consisting of 21600 rows and 43200 columns at a geographic pixel size of approximately 0.008333 °. Selection of soils with high carbon content was made on the basis of soil units. All Histosols (Eutric, Dystric and Gelic) and a unit of Podzols (Placic) were selected.

A.3 Biomes

The biome classification map was obtained from The Nature Conservancy website [4] and is based on the Priority Ecoregions for global conservation [74], the World Wildlife Fund's ecoregions and also loosely based on Bailey's ecoregions. The classification includes 16 biome classes and again is on the WGS 1984 coordinate reference system (EPSG: 4326).

A.4 Enhancement Ratios

On the basis of a previous paper [37] and recent literature [126], ER_{coarse} were estimated for specific land cover classes and biomes (Table SI-A.5.1). The ERs

Table A.5.1: Emission factors for CO and Hg and the calculated ER_{coarse} for different land cover types

	EF_{CO} $g\,kg^{-1}\,DM^{-1}$	EF_{Hg} $\mu g\,kg^{-1}\,DM^{-1}$	Ref.	ER $\times\,10^{-7}$
Tropical Forest	96.5	198.0	1	2.05
Savanna & Grassland	63.5	17.6	2	0.28
Chaparral	67.0	41.1	2	0.61
Woodland	88.3	41.1	2	0.47
Extratropical Forest	116.0	242.0	1	2.09
Boreal Forest	127.0	314.9	2	2.48
Temperate Forest	89.0	238.8	2	2.68
Peatland	210.0	315.0	2	1.5
Agricultural Area	98.5	17.6	2	0.18
Average	106.2	158.4	2	1.44

References: van Leeuwen and van der Werf [126]; 1. this work; 2. Friedli et al. [37]

obtained were assigned to selected land cover classes divided into biomes to derive ER_{fine}, (Table SI-A.5.2).

A.5 Map calculations

Maps of land cover, biomes and organic soils were elaborated using ArcGIS (ESRI [1]) by means of the raster calculator. Before this step, maps were pre-processed to harmonize the spatial resolution. All maps were re-gridded to 1' x 1' resolution comprising 30317 rows $\times$ 84205 columns, giving a geographic pixel size of approximately 0.016667°. The following step associated the organic soil map with the land cover map resulting in a new map with an additional class. The 18 classes were then assigned to their respective biomes, namely boreal, temperate and tropical. The final result was the ER_{fine} map (Fig. SI-A.5.1). This output was, finally, re-gridded to $1^{\circ} \times 1^{\circ}$ to be used as input for ECHMERIT.

[1] http://www.esri.com/software/arcgis

Table A.5.2: ER_{fine} ($\times 10^{-7}$) for different land cover classes and biomes

Class	name	Boreal	Temperate	Tropical
0	Water Bodies	-	-	-
1	Evergreen Needleleaf Forests	2.48	2.68	2.05
2	Evergreen Broadleaf Forests	2.48	2.68	2.05
3	Deciduous Needleleaf Forests	2.48	2.68	2.05
4	Deciduous Broadleaf Forests	2.48	2.68	2.05
5	Mixed Forests	2.48	2.68	2.05
6	Closed Shrublands	-	0.61	0.61
7	Open Shrublands	-	0.61	0.61
8	Woody Savannas	-	0.28	0.28
9	Savannas	0.28	0.28	0.28
10	Grasslands	0.28	0.28	0.28
11	Permanent Wetlands	-	-	-
12	Cropland	0.18	0.18	0.18
13	Urban and Built-up	-	-	-
14	Cropland/Natural Vegetation Mosaics	0.18	0.18	0.18
15	Snow and Ice	-	-	-
16	Barren	-	-	-
17	Tundra	-	-	-
18	Peat	1.50	1.15	1.15

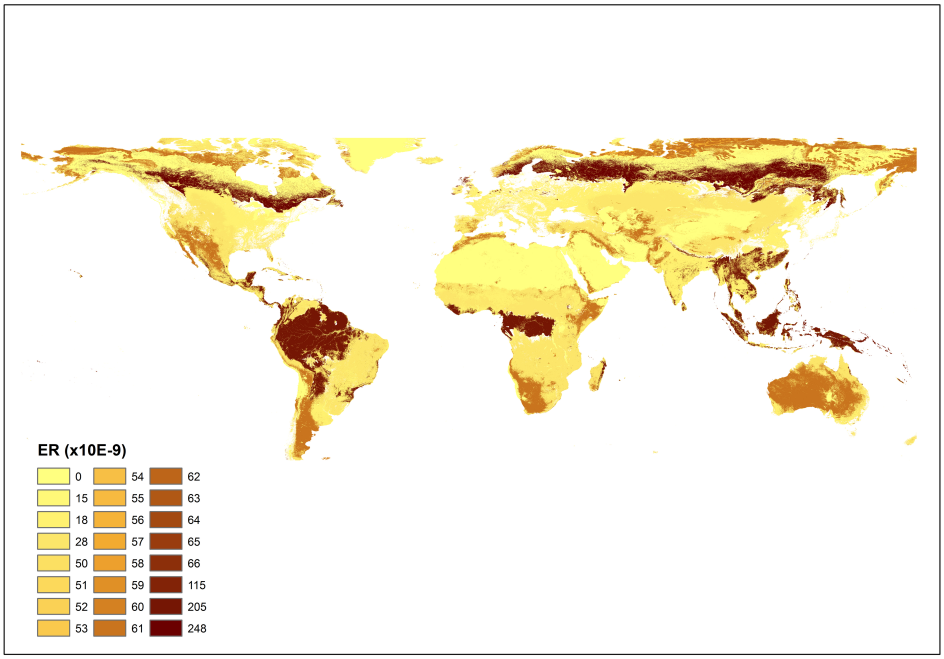

Figure A.5.1: Map of the distribution ER_{fine}

B

EDGAR IPCC to SNAP Categories Conversion

EDGARv4.tox1 mercury emissions are provided with no information about the vertical distribution of emissions. However they are disaggregated by sector[1], defined by using the IPCC source categories and codes developed by the IPCC National Greenhouse Gas Inventories Programme [22]. These IPCC source categories have been defined for reporting of national greenhouse gas inventories under the UN Climate Convention and also for reporting by European countries of national air pollutant emission inventories to the UN-ECE secretariat under the Convention on Long-range Transboundary Air Pollution (CLRTAP) and to the European Commission as required in the NEC directive.

The EMEP/CORINAIR Nomenclature for Reporting (NFR) source categories

[1] http://edgar.jrc.ec.europa.eu/faq6.php

have been developed to be compatible to the IPCC reporting categories. A table for converting NFR09 to SNAP main sectors is provided by CEIP (the EMEP Centre on Emission Inventories and Projections) and available at [2]. Such information have been used to convert EDGAR emissions sources to SNAP sector (see Table B.0.1)

Table B.0.1: Conversion among IPCC, NFR09 and SNAP 11 Categories

EDGAR Hg sector	IPCC Code	NFR09	SNAP
cement production,	2A	2A1	4
chlor-alkali industry, mercury cell technology,	2B	2B5a	4
combustion in power generation and in industry,	1a1a,1a1bc	1a1a,1a1c	1
combustion in residential and other combustion,	1A2,1A4,1A1bc	1A2f,1A4Bi,1A1B	1,2,3
large scale gold production,	2A7	2A7A	5
iron and steel production,	2C	2C1	4
production of Zn, Cu, Pb and Hg,	2C	2C5	4
solid waste incineration and agricultural waste burning.	6	6	9

The EDGAR Hg emissions have been then finally vertically distributed according to a default distribution based upon the SNAP codes as in EMEP model, as shown in Table B.0.2. These distributions have been based upon plume-rise calculations performed for different types of emission source which are thought typical for different emission categories, under a range of stability conditions [3].

[2] http://www.ceip.at/fileadmin/inhalte/emep/pdf/nfr09_to_snap.pdf
[3] http://www.emep.int/UniDoc/node7.html

Table B.0.2: Vertical distribution of Anthropogenic Emissions based on SNAP sector (in meter).

		Height of Emission Layer (m)					
SNAP Sector	Sources	0-92	93-184	185-324	325-522	523-781	782-1106
1	Combustion in energy and transformation industries	0	0	8	46	29	17
2	Non-industrial combustion plants	50	50				
3	Combustion in manufacturing industry	0	4	19	41	30	6
4	Production processes	90	10				
5	Extraction and distribution of fossil fuels and geothermal energy	90	10				
6	Solvents and other product use	100					
7	Road transport	100					
8	Other mobile sources and machinery	100					
9	Waste treatment and disposal	10	15	40	35		
10	Agriculture	100					

References

[1] Assessment of the Global Fire Assimilation System (GFASv1). MACC-II (Monitoring Atmospheric Composition and Climate) project, 2013; http://juser.fz-juelich.de/record/186645.

[2] Harmonized world soil database (version 1.2), (FAO/IIASA/ISRIC/ISSCAS/JRC). http://webarchive.iiasa.ac.at/Research/LUC/External-World-soil-database/HTML/.

[3] Fire_emis: Fortran based preprocessor for creating fire emission inputs for WRF-Chem. http://www.acd.ucar.edu/wrf-chem/.

[4] Terrestrial ecoregions of the world. http://maps.tnc.org/gis_data.html.

[5] Climate data operators, 2014. Max-Plank Institute fur Meteorologie, 2014; https://code.zmaw.de/projects/cdo.

[6] AMAP/UNEP. Technical background report for the global mercury assessment 2008. Technical report, 2008. URL http://www.unep.org/hazardoussubstances/Mercury/Informationmaterials/ReportsandPublications/tabid/3593/Default.aspx.

[7] AMAP/UNEP. Technical background report for the global mercury assessment 2013. Technical report, 2013. URL http://www.unep.org/hazardoussubstances/Mercury/Informationmaterials/ReportsandPublications/tabid/3593/Default.aspx.

[8] V. Amiridis, E. Giannakaki, D. S. Balis, E. Gerasopoulos, I. Pytharoulis, P. Zanis, S. Kazadzis, D. Melas, and C. Zerefos. Smoke injection heights

from agricultural burning in Eastern Europe as seen by CALIPSO. *Atmos. Chem. Phys.*, 10(23):11567–11576, 2010.

[9] H. M. Amos, D. J. Jacob, C. D. Holmes, J. A. Fisher, Q. Wang, R. M. Yantosca, E. S. Corbitt, E. Galarneau, A. P. Rutter, M. S. Gustin, A. Steffen, J. J. Schauer, J. A. Graydon, V. L. St. Louis, R. W. Talbot, E. S. Edgerton, Y. Zhang, and E. M. Sunderland. Gas-particle partitioning of atmospheric hg(ii) and its effect on global mercury deposition. *Atmospheric Chemistry and Physics*, 12(1):591–603, 2012. doi: 10.5194/acp-12-591-2012.

[10] Helen M. Amos, Daniel J. Jacob, David G. Streets, and Elsie M. Sunderland. Legacy impacts of all-time anthropogenic emissions on the global mercury cycle. *Global Biogeochem. Cycles*, 27(2):410–421, 2013. ISSN 1944-9224.

[11] Helen M. Amos, Daniel J. Jacob, David Kocman, Hannah M. Horowitz, Yanxu Zhang, Stephanie Dutkiewicz, Milena Horvat, Elizabeth S. Corbitt, David P. Krabbenhoft, and Elsie M. Sunderland. Global biogeochemical implications of mercury discharges from rivers and sediment burial. *Environmental Science & Technology*, 48(16):9514–9522, 2014. doi: 10.1021/es502134t. PMID: 25066365.

[12] Helen M. Amos, Jeroen E. Sonke, Daniel Obrist, Nicholas Robins, Nicole Hagan, Hannah M. Horowitz, Robert P. Mason, Melanie Witt, Ian M. Hedgecock, Elizabeth S. Corbitt, and Elsie M. Sunderland. Observational and modeling constraints on global anthropogenic enrichment of mercury. *Environmental Science & Technology*, 49(7):4036–4047, 2015. doi: 10.1021/es5058665.

[13] Maria E. Andersson, Katarina Gårdfeldt, Ingvar Wängberg, and Dan Strömberg. Determination of henry's law constant for elemental mercury. *Chemosphere*, 73(4):587–592, September 2008. ISSN 0045-6535.

[14] Maria E. Andersson, Jonas Sommar, Katarina Gårdfeldt, and Sara Jutterström. Air–sea exchange of volatile mercury in the north atlantic ocean. *Marine Chemistry*, 125(1–4):1 – 7, 2011. ISSN 0304-4203. doi: 10.1016/j.marchem.2011.01.005.

[15] M.E. Andersson, K. Gårdfeldt, I. Wängberg, F. Sprovieri, N. Pirrone, and O. Lindqvist. Seasonal and daily variation of mercury evasion at coastal and off shore sites from the mediterranean sea. *Marine Chemistry*, 104(3-4):214–226, 2007.

[16] J. Bieser, F. De Simone, C. Gencarelli, B. Geyer, I. Hedgecock, V. Matthias, O. Travnikov, and A. Weigelt. A diagnostic evaluation of modeled mercury wet depositions in europe using atmospheric speciated high-resolution observations. *Environmental Science and Pollution Research*, 21(16):9995–10012, 2014. doi: 10.1007/s11356-014-2863-2. URL http://dx.doi.org/10.1007/s11356-014-2863-2.

[17] Joel D. Blum, Brian N. Popp, Jeffrey C. Drazen, C. Anela Choy, and Marcus W. Johnson. Methylmercury production below the mixed layer in the North Pacific Ocean. *Nat. Geosci.*, 6(10):879–884, October 2013. ISSN 1752-0894.

[18] E.-G. Brunke, R. Ebinghaus, H. H. Kock, C. Labuschagne, and F. Slemr. Emissions of mercury in southern africa derived from long-term observations at cape point, south africa. *Atmospheric Chemistry and Physics*, 12(16):7465–7474, 2012. doi: 10.5194/acp-12-7465-2012. URL http://www.atmos-chem-phys.net/12/7465/2012/.

[19] O. Russell Bullock, Dwight Atkinson, Thomas Braverman, Kevin Civerolo, Ashu Dastoor, Didier Davignon, Jia-Yeong Ku, Kristen Lohman, Thomas C. Myers, Rokjin J. Park, Christian Seigneur, Noelle E. Selin, Gopal Sistla, and Krish Vijayaraghavan. The north american mercury model intercomparison study (nammis): Study description and model-to-model comparisons. *Journal of Geophysical Research: Atmospheres*, 113 (D17):D17310–, 2008. ISSN 2156-2202.

[20] O. Russell Jr Bullock, Dwight Atkinson, Thomas Braverman, Kevin Civerolo, Ashu Dastoor, Didier Davignon, Jia Y. Ku, Kristen Lohman, Thomas C. Myers, Rokjin J. Park, Christian Seigneur, Noelle E. Selin, Gopal Sistla, and Krish Vijayaraghavan. An analysis of simulated wet deposition of mercury from the north american mercury model intercomparison study. *J. Geophys. Res.*, 114(D8):D08301–, April 2009. ISSN 0148-0227.

[21] Jack G. Calvert and Steve E. Lindberg. Mechanisms of mercury removal by o3 and oh in the atmosphere. *Atmospheric Environment*, 39(18):3355–3367, June 2005. ISSN 1352-2310.

[22] Intergovernmental Panel On Climate Change. Revised 1996 ipcc guidelines for national greenhouse gas inventories, 1996.

[23] Sergio Cinnirella and Nicola Pirrone. Spatial and temporal distributions of mercury emissions from forest fires in Mediterranean region and Russian federation. *Atmos. Environ.*, 40(38):7346 – 7361, 2006. ISSN 1352-2310.

[24] Andrew B. Collier and Arthur R.W. Hughes. Lightning and the african {ITCZ}. *Journal of Atmospheric and Solar-Terrestrial Physics*, 73(16):2392 – 2398, 2011. ISSN 1364-6826. doi: 10.1016/j.jastp.2011.08.010.

[25] Elizabeth S Corbitt, Daniel J Jacob, Christopher D Holmes, David G Streets, and Elsie M Sunderland. Global source–receptor relationships for mercury deposition under present-day and 2050 emissions scenarios. *Environmental science & technology*, 45(24):10477–10484, 2011.

[26] V. Damian, Sandu A., Damian M., Potra F., and Carmichael G.R. The kinetic preprocessor kpp-a software environment for solving chemical kinetics. *Computers and Chemical Engineering*, 26(11):1567–1579, 2002. doi: doi:10.1016/S0098-1354(02)00128-X.

[27] Ashu P. Dastoor and Yvan Larocque. Global circulation of atmospheric mercury: a modelling study. *Atmospheric Environment*, 38(1):147–161, January 2004. ISSN 1352-2310.

[28] F. De Simone, C. N. Gencarelli, I. M. Hedgecock, and N. Pirrone. Global atmospheric cycle of mercury: a model study on the impact of oxidation mechanisms. *Environ. Sci. Pollut. Res.*, 21(6):4110–4123, 2014. ISSN 0944-1344.

[29] Francesco De Simone, Sergio Cinnirella, Christian Gencarelli, Xin Yang, Ian Hedgecock, and Nicola Pirrone. A model study of global mercury deposition from biomass burning. *Environmental science & technology*, 2015.

[30] F. Dentener, S. Kinne, T. Bond, O. Boucher, J. Cofala, S. Generoso, P. Ginoux, S. Gong, J. J. Hoelzemann, A. Ito, L. Marelli, J. E. Penner, J.-P. Putaud, C. Textor, M. Schulz, G. R. van der Werf, and J. Wilson. Emissions of primary aerosol and precursor gases in the years 2000 and 1750 prescribed data-sets for aerocom. *Atmos. Chem. Phys.*, 6(12):4321–4344, 2006.

[31] D. L. Donohoue, D. Bauer, B. Cossairt, and A. J. Hynes. Temperature and pressure dependent rate coefficients for the reaction of hg with br and the reaction of br with br: A pulsed laser photolysis-pulsed laser induced fluorescence study. *J. Phys. Chem. A*, 110:6623–6632, 2006.

[32] Charles T. Driscoll, Robert P. Mason, Hing Man Chan, Daniel J. Jacob, and Nicola Pirrone. Mercury as a Global Pollutant: Sources, Pathways, and Effects. *Environ. Sci. Technol.*, 47(10):4967–4983, 2013.

[33] D. Durnford, A. Dastoor, D. Figueras-Nieto, and A. Ryjkov. Long range transport of mercury to the arctic and across canada. *Atmospheric Chemistry and Physics*, 10(13):6063–6086, 2010.

[34] D. A. Durnford, A. P. Dastoor, A. O. Steen, T. Berg, A. Ryzhkov, D. Figueras-Nieto, L. R. Hole, K. A. Pfaffhuber, and H. Hung. How relevant is the deposition of mercury onto snowpacks? – part 1: A statistical study on the impact of environmental factors. *Atmospheric Chemistry and Physics Discussions*, 12(1):387 – 439, 2012.

[35] L. K. Emmons, S. Walters, P. G. Hess, J.-F. Lamarque, G. G. Pfister, D. Fillmore, C. Granier, A. Guenther, D. Kinnison, T. Laepple, J. Orlando, X. Tie, G. Tyndall, C. Wiedinmyer, S. L. Baughcum, and S. Kloster. Description and evaluation of the model for ozone and related chemical tracers, version 4 (mozart-4). *Geoscientific Model Development*, 3(1):43–67, 2010.

[36] Mark A. Friedl, Damien Sulla-Menashe, Bin Tan, Annemarie Schneider, Navin Ramankutty, Adam Sibley, and Xiaoman Huang. Modis collection 5 global land cover: Algorithm refinements and characterization of new datasets. *Remote Sens. Environ.*, 114(1):168–182, January 2010. ISSN 0034-4257.

[37] H. R. Friedli, A. F. Arellano, S. Cinnirella, and N. Pirrone. Initial estimates of mercury emissions to the atmosphere from global biomass burning. *Environ. Sci. Technol.*, 43(10):3507–3513, 2009.

[38] Katarina Gårdfeldt and Mats Jonsson. Is bimolecular reduction of hg(ii) complexes possible in aqueous systems of environmental importance. *The Journal of Physical Chemistry A*, 107(22):4478 – 4482, 2003.

[39] D. A. Gay, D. Schmeltz, E. Prestbo, M. Olson, T. Sharac, and R. Tordon. The atmospheric mercury network: measurement and initial examination of an ongoing atmospheric mercury record across north america. *Atmospheric Chemistry and Physics Discussions*, 13(4):10521–10546, 2013.

[40] M. E. Goodsite, J. M. C. Plane, and H. Skov. A theoretical study of the oxidation of hgo to hgbr2 in the troposphere. *Environ. Sci. Technol.*, 38(6): 1772–1776, February 2004. ISSN 0013-936X. doi: doi:10.1021/es034680s.

[41] M. E. Goodsite, J. M. C. Plane, and H. Skov. Correction to a theoretical study of the oxidation of hg^{o} to $hgbr_2$ in the troposphere. *Environ. Sci. Technol.*, 46(9):5262–5262, 2012.

[42] M.E. Goodsite, P.M. Outridge, J.H. Christensen, A. Dastoor, D. Muir, O. Travnikov, and S. Wilson. How well do environmental archives of atmospheric mercury deposition in the arctic reproduce rates and trends depicted by atmospheric models and measurements? *Science of The Total Environment*, 452–453(0):196–207, May 2013. ISSN 0048-9697.

[43] C. Granier, J.F. Lamarque, A. Mieville, J.F. Muller, J. Olivier, J. Orlando, J. Peters, G. Petron, G. Tyndall, and S. Wallens. Poet, a database of surface emissions of ozone precursors,. *available on internet*, 2005.

[44] H. Guan, R. B. Chatfield, S. R. Freitas, R. W. Bergstrom, and K. M. Longo. Modeling the effect of plume-rise on the transport of carbon monoxide over africa with NCAR CAM. *Atmos. Chem. Phys.*, 8(22):6801–6812, 2008.

[45] Stefan Hagemann, Klaus Arpe, and Erich Roeckner. Evaluation of the hydrological cycle in the echam5 model. *J. Climate*, 19(16):3810–3827, August 2006. ISSN 0894-8755.

[46] B. Hall. The gas phase oxidation of elemental mercury by ozone. *Wat. Air Soil Pollut.*, 80(1-4):301–315, 1995.

[47] Reed Harris, Curtis Pollman, William Landing, David Evans, Donald Axelrad, David Hutchinson, Steven L. Morey, Darren Rumbold, Dmitry Dukhovskoy, Douglas H. Adams, Krish Vijayaraghavan, Christopher Holmes, R. Dwight Atkinson, Tom Myers, and Elsie Sunderland. Mercury in the gulf of mexico: Sources to receptors. *Environmental Research*, 119 (0):42–52, November 2012. ISSN 0013-9351.

[48] Ian M. Hedgecock, Giuseppe A. Trunfio, Nicola Pirrone, and Francesca Sprovieri. Mercury chemistry in the mbl: Mediterranean case and sensitivity studies using the amcots (atmospheric mercury chemistry over the sea) model. *Atmospheric Environment*, 39(38):7217–7230, December 2005. ISSN 1352-2310.

[49] C. D. Holmes, D. J. Jacob, E. S. Corbitt, J. Mao, X. Yang, R. Talbot, and F. Slemr. Global atmospheric model for mercury including oxidation by

bromine atoms. *Atmospheric Chemistry and Physics*, 10(24):12037–12057, 2010. doi: 10.5194/acp-10-12037-2010.

[50] Larry W. Horowitz, Stacy Walters, Denise L. Mauzerall, Louisa K. Emmons, Philip J. Rasch, Claire Granier, Xuexi Tie, Jean-François Lamarque, Martin G. Schultz, Geoffrey S. Tyndall, John J. Orlando, and Guy P. Brasseur. A global simulation of tropospheric ozone and related tracers: Description and evaluation of mozart, version 2. *Journal of Geophysical Research: Atmospheres*, 108(D24):4787 –, 2003. ISSN 2156-2202.

[51] Anthony J. Hynes, Deanna L. Donohoue, Michael E. Goodsite, and Ian M. Hedgecock. Our current understanding of major chemical and physical processes affecting mercury dynamics in the atmosphere and at the air-water/terrestrial interfaces. In N. Pirrone and R. P. Mason, editors, *Mercury Fate and Transport in the Global Atmosphere: Emissions, Measurements and Models*, chapter 14, pages 427–457. Springer, 2009.

[52] Charles Ichoku, Ralph Kahn, and Mian Chin. Satellite contributions to the quantitative characterization of biomass burning for climate modeling. *Atmos. Res.*, 111(0):1–28, July 2012. ISSN 0169-8095.

[53] Mark Z Jacobson. *Fundamentals of atmospheric modeling*. Cambridge University Press, 1999.

[54] Y. Jian and T.-M. Fu. Injection heights of springtime biomass-burning plumes over peninsular Southeast Asia and their impacts on long-range pollutant transport. *Atmos. Chem. Phys.*, 14(8):3977–3989, 2014.

[55] G. Jung, I. M. Hedgecock, and N. Pirrone. Echmerit v1.0 â€“ a new global fully coupled mercury-chemistry and transport model. *Geoscientific Model Development*, 2(2):175–195, 2009. doi: 10.5194/gmd-2-175-2009.

[56] J. W. Kaiser, A. Heil, M. O. Andreae, A. Benedetti, N. Chubarova, L. Jones, J.-J. Morcrette, M. Razinger, M. G. Schultz, M. Suttie, and G. R. van der Werf. Biomass burning emissions estimated with a global fire assimilation system based on observed fire radiative power. *Biogeosciences*, 9(1):527–554, 2012.

[57] A. Kerkweg, J. Buchholz, L. Ganzeveld, A. Pozzer, H. Tost, and P. Jöckel. Technical note: An implementation of the dry removal processes dry deposition and sedimentation in the modular earth submodel system (messy).

Atmospheric Chemistry and Physics, 6(12):4617–4632, 2006. doi: 10.5194/acp-6-4617-2006.

[58] K. Lapina, R. E. Honrath, R. C. Owen, M. Val Martín, E. J. Hyer, and P. Fialho. Late summer changes in burning conditions in the boreal regions and their implications for NOx and CO emissions from boreal fires. *J. Geophys. Res. Atmos.*, 113(D11):D11304–, 2008. ISSN 2156-2202.

[59] H. Lei, X.-Z. Liang, D. J. Wuebbles, and Z. Tao. Model analyses of atmospheric mercury: present air quality and effects of transpacific transport on the united states. *Atmospheric Chemistry and Physics Discussions*, 13(4):9849–9893, 2013. doi: 10.5194/acpd-13-9849-2013. URL http://www.atmos-chem-phys-discuss.net/13/9849/2013/.

[60] Fok-Yan T. Leung, Jennifer A. Logan, Rokjin Park, Edward Hyer, Eric Kasischke, David Streets, and Leonid Yurganov. Impacts of enhanced biomass burning in the boreal forests in 1998 on tropospheric chemistry and the sensitivity of model results to the injection height of emissions. *J. Geophys. Res. Atmos.*, 112(D10):D10313–, May 2007. ISSN 2156-2202.

[61] S.-J. Lin and R. B. Rood. Multidimensional Flux-Form Semi-Lagrangian Transport Schemes. *Monthly Weather Review*, 124:2046, 1996. doi: 10.1175/1520-0493(1996)124<2046:MFFSLT>2.0.CO;2.

[62] Steve E. Lindberg Simo O. Pehkonen Daewon Byun Carey Jang Lin Che-Jen, Pruek Pongprueksa. Scientific uncertainties in atmospheric mercury models i: Model science evaluation. *Atmospheric Environment*, 40:2911–2928, 2006.

[63] Steve Lindberg, Russell Bullock, Ralf Ebinghaus, Daniel Engstrom, Xinbin Feng, William Fitzgerald, Nicola Pirrone, Eric Prestbo, and Christian Seigneur. A synthesis of progress and uncertainties in attributing the sources of mercury in deposition. *AMBIO: A Journal of the Human Environment*, 36(1):19–33, 2007.

[64] P. S. Liss and P. G. Slater. Flux of gases across the air-sea interface. *Nature*, 247(5438):181–184, January 1974.

[65] Kristen Lohman, Christian Seigneur, Eric Edgerton, and John Jansen. Modeling mercury in power plant plumes. *Environ. Sci. Technol.*, 40(12):3848–3854, May 2006. ISSN 0013-936X.

[66] Kristen Lohman, Christian Seigneur, Mae Gustin, and Steve Lindberg. Sensitivity of the global atmospheric cycle of mercury to emissions. *Applied Geochemistry*, 23(3):454–466, March 2008. ISSN 0883-2927.

[67] R. P. Mason and G.-R. Sheu. Role of the ocean in the global mercury cycle. *Global Biogeochem. Cycles*, 16(4):1093–, November 2002. ISSN 0886-6236.

[68] Robert P Mason. Mercury emissions from natural processes and their importance in the global mercury cycle. In *Mercury fate and transport in the global atmosphere*, pages 173–191. Springer, 2009.

[69] Robert P Mason, Anna L Choi, William F Fitzgerald, Chad R Hammerschmidt, Carl H Lamborg, Anne L Soerensen, and Elsie M Sunderland. Mercury biogeochemical cycling in the ocean and policy implications. *Environmental research*, 119:101–117, 2012.

[70] Marilena Muntean, Greet Janssens-Maenhout, Shaojie Song, Noelle E. Selin, Jos G.J. Olivier, Diego Guizzardi, Rob Maas, and Frank Dentener. Trend analysis from 1970 to 2008 and model evaluation of {EDGARv4} global gridded anthropogenic mercury emissions. *Science of The Total Environment*, 494–495(0):337 – 350, 2014. ISSN 0048-9697. doi: http://dx.doi.org/10.1016/j.scitotenv.2014.06.014.

[71] John Munthe. The aqueous oxidation of elemental mercury by ozone. *Atmos. Environ.*, 26(8):1461 – 1468, 1992.

[72] T.E. Nordeng. Extended versions of the convection parametrization scheme at ecmwf and their impact upon the mean climate and transient activity of the model in the tropics. Technical report, Research Dept Technical Memorandum No. 206, ECMWF, Shinfield Park, Reading RG2 9AX, United Kingdom., 1994.

[73] Daniel Obrist, Hans Moosmüller, Roger Schürmann, L-W Antony Chen, and Sonia M Kreidenweis. Particulate-phase and gaseous elemental mercury emissions during biomass combustion: Controlling factors and correlation with particulate matter emissions. *Environ. Sci. Technol.*, 42(3): 721–727, 2007.

[74] D. M. Olson and E. Dinerstein. The global 200: Priority ecoregions for global conservation. *Ann. Mo. Bot. Gard.*, 89:125–126, 2002.

[75] E.G. Pacyna, J.M. Pacyna, K. Sundseth, J. Munthe, K. Kindbom, S. Wilson, F. Steenhuisen, and P. Maxson. Global emission of mercury to the atmosphere from anthropogenic sources in 2005 and projections to 2020. *Atmospheric Environment*, 44(20):2487 – 2499, 2010. ISSN 1352-2310. doi: http://dx.doi.org/10.1016/j.atmosenv.2009.06.009. URL http://www.sciencedirect.com/science/article/pii/S1352231009005007.

[76] Simo O Pehkonen and Che-Jen Lin. Aqueous photochemistry of mercury with organic acids. *Journal of the Air & Waste Management Association*, 48 (2):144–150, 1998.

[77] J. A. H W. Peters and J. G J. Olivier. Edgar3/poet enussuibs; 1997 emissions and scenarios for 1995–2020; technical background infromation on global and regional sectoral emissions. *RIVM, Bilthoven, report no. 773301003*, 2003.

[78] N Pirrone, S Cinnirella, Xinbin Feng, RB Finkelman, HR Friedli, J Leaner, R Mason, AB Mukherjee, GB Stracher, DG Streets, et al. Global mercury emissions to the atmosphere from anthropogenic and natural sources. *Atmospheric Chemistry and Physics*, 10(13):5951–5964, 2010.

[79] Nicola Pirrone, Ivo Allegrini, Gerald J. Keeler, Jerome O. Nriagu, Ronald Rossmann, and John A. Robbins. Historical atmospheric mercury emissions and depositions in north america compared to mercury accumulations in sedimentary records. *Atmospheric Environment*, 32(5):929 – 940, 1998.

[80] U. Platt and C. Janssen. Observation and role of the free radicals no_3, clo, bro and io in the troposphere. *Faraday Discuss.*, 100:175–198, 1995.

[81] Pruek Pongprueksa, Che-Jen Lin, Steve E. Lindberg, Carey Jang, Thomas Braverman, O. Russell Bullock Jr., Thomas C. Ho, and Hsing-Wei Chu. Scientific uncertainties in atmospheric mercury models iii: Boundary and initial conditions, model grid resolution, and hg(ii) reduction mechanism. *Atmospheric Environment*, 42(8):1828 – 1845, 2008.

[82] L Pozzoli, I Bey, S Rast, MG Schultz, P Stier, and J Feichter. Trace gas and aerosol interactions in the fully coupled model of aerosol-chemistry-climate echam5-hammoz: 1. model description and insights from the spring 2001 trace-p experiment. *Journal of Geophysical Research: Atmospheres (1984–2012)*, 113(D7), 2008.

[83] Ligia Pérez-Cruz. Hydrological changes and paleoproductivity in the gulf of california during middle and late holocene and their relationship with itcz and north american monsoon variability. *Quaternary Research*, 79(2): 138–151, March 2013. ISSN 0033-5894.

[84] E. Roeckner, G. Bäuml, L. Bonaventura, R. Brokopf, M. Esch, M. Giorgetta, S. Hagemann, I. Kirchner, L. Kornblueh, E. Manzini, A. Rhodin, U. Schlese, U. Schulzweida, and Tompkins A. The atmospheric general circulation model echam 5. part i: Model description. Technical report, Max Planck Institute for Meteorology (MPI-M), Hamburg, Germany, 2003. MPI-Report No. 349.

[85] E. Roeckner, R. Brokopf, M. Esch, M. Giorgetta, S. Hagemann, L. Kornblueh, E. Manzini, U. Schlese, and U. Schulzweida. Sensitivity of simulated climate to horizontal and vertical resolution in the echam5 atmosphere model. *J. Climate*, 19(16):3771–3791, August 2006. ISSN 0894-8755.

[86] R. Sander, A. Kerkweg, P. Jöckel, and J. Lelieveld. Technical note: The new comprehensive atmospheric chemistry module mecca. *Atmospheric Chemistry and Physics*, 5(2):445–450, 2005.

[87] A. Sandu and R. Sander. Technical note: Simulating chemical systems in fortran90 and matlab with the kinetic preprocessor kpp-2.1. *Atmospheric Chemistry and Physics*, 6(1):187–195, 2006. doi: 10.5194/acp-6-187-2006.

[88] H. Sanei, P.M. Outridge, F. Goodarzi, F. Wang, D. Armstrong, K. Warren, and L. Fishback. Wet deposition mercury fluxes in the canadian sub-arctic and southern alberta, measured using an automated precipitation collector adapted to cold regions. *Atmospheric Environment*, 44(13):1672–1681, 2010.

[89] B. D. Santer, K. E. Taylor, T. M. L. Wigley, T. C. Johns, P. D. Jones, D. J. Karoly, J. F. B. Mitchell, A. H. Oort, J. E. Penner, V. Ramaswamy, M. D. Schwarzkopf, R. J. Stouffer, and S. Tett. A search for human influences on the thermal structure of the atmosphere. *Nature*, 382(6586):39–46, July 1996.

[90] Benjamin D. Santer, Karl E. Taylor, Tom M.L. Wigley, Joyce E. Penner, Philip D. Jones, and Ulrich Cubasch. Towards the detection and attribution of an anthropogenic effect on climate. *Clim. Dyn.*, 12(2):77–100, 1995.

[91] William H. Schroeder and John Munthe. Atmospheric mercury – An overview. *Atmos. Environ.*, 32(5):809 – 822, 1998.

[92] Stephen E Schwartz. Mass-transport considerations pertinent to aqueous phase reactions of gases in liquid-water clouds. *Chemistry of multiphase atmospheric systems*, 6:415–471, 1986.

[93] C. Seigneur, K. Vijayaraghavan, and K. Lohman. Atmospheric mercury chemistry: Sensitivity of global model simulations to chemical reactions. *Journal of Geophysical Research D: Atmospheres*, 111(22):D22306, 2006.

[94] Christian Seigneur, Prakash Karamchandani, Kristen Lohman, Krish Vijayaraghavan, and Run-Lie Shia. Multiscale modeling of the atmospheric fate and transport of mercury. *Journal of Geophysical Research: Atmospheres*, 106(D21):27795–27809, 2001. ISSN 2156-2202.

[95] John H Seinfeld and Pandis. *Atmospheric chemistry and physics: from air pollution to climate change*. Wiley-Interscience, 1998.

[96] Noelle E. Selin. Global biogeochemical cycling of mercury: A review. *Annual Review of Environment and Resources*, 34(1):43–63, 2009.

[97] Noelle E. Selin. Global change and mercury cycling: Challenges for implementing a global mercury treaty. *Environ. Toxicol. Chem.*, 33(6):1202–1210, June 2014. ISSN 1552-8618.

[98] Noelle E. Selin, Daniel J. Jacob, Rokjin J. Park, Robert M. Yantosca, Sarah Strode, Lyatt Jaeglé, and Daniel Jaffe. Chemical cycling and deposition of atmospheric mercury: Global constraints from observations. *Journal Of Geophysical Research - Atmospheres*, 112(D2):D02308–, January 2007.

[99] Noelle E. Selin, Daniel J. Jacob, Robert M. Yantosca, Sarah Strode, Lyatt Jaeglé, and Elsie M. Sunderland. Global 3-d land-ocean-atmosphere model for mercury: Present-day versus preindustrial cycles and anthropogenic enrichment factors for deposition. *Global Biogeochem. Cycles*, 22:GB2011, May 2008.

[100] David Simpson, Anna Benedictow, Halldis Berge, Robert Bergström, Lisa D Emberson, Hilde Fagerli, Chris R Flechard, Garry D Hayman, Michael Gauss, Jan Eiof Jonson, et al. The emep msc-w chemical transport model–technical description. *Atmospheric Chemistry and Physics*, 12 (16):7825–7865, 2012.

[101] F. Slemr, E.-G. Brunke, R. Ebinghaus, and J. Kuss. Worldwide trend of atmospheric mercury since 1995. *Atmospheric Chemistry and Physics*, 11(10): 4779–4787, 2011.

[102] Anne L. Soerensen, Elsie M. Sunderland, Christopher D. Holmes, Daniel J. Jacob, Robert M. Yantosca, Henrik Skov, Jesper H. Christensen, Sarah A. Strode, and Robert P. Mason. An improved global model for air-sea exchange of mercury: High concentrations over the north atlantic. *Environmental Science & Technology*, 44(22):8574 – 8580, 2010.

[103] Anne L. Soerensen, Daniel J. Jacob, David G. Streets, Melanie L. I. Witt, Ralf Ebinghaus, Robert P. Mason, Maria Andersson, and Elsie M. Sunderland. Multi-decadal decline of mercury in the north atlantic atmosphere explained by changing subsurface seawater concentrations. *Geophys. Res. Lett.*, 39(21):L21810–, 2012. ISSN 0094-8276.

[104] E. Solazzo and S. Galmarini. A science-based use of ensembles of opportunities for assessment and scenario study: a re-analysis of htap-1 ensemble. *Atmos. Chem. Phys.*, 15(5):2535–2544, 2015.

[105] Jonas Sommar, Mattias Hallquist, Evert Ljungström, and Oliver Lindqvist. On the gas phase reactions between volatile biogenic mercury species and the nitrate radical. *Journal of atmospheric chemistry*, 27(3):233–247, 1997.

[106] Jonas Sommar, Katarina Gårdfeldt, Dan Strömberg, and Xinbin Feng. A kinetic study of the gas-phase reaction between the hydroxyl radical and atomic mercury. *Atmos. Environ.*, 35(17):3049 – 3054, 2001. ISSN 1352-2310.

[107] F. Sprovieri, N. Pirrone, R. Ebinghaus, H. Kock, and A. Dommergue. A review of worldwide atmospheric mercury measurements. *Atmospheric Chemistry and Physics*, 10(17):8245–8265, 2010.

[108] J.E. Stopa, K. F. Cheung, Hendrik L. Tolman, and Arun Chawla. Patterns and cycles in the climate forecast system reanalysis wind and wave data. *Ocean Modelling*, (0):–, 2012. ISSN 1463-5003. doi: 10.1016/j.ocemod.2012.10.005.

[109] David G. Streets, Qiang Zhang, and Ye Wu. Projections of global mercury emissions in 2050. *Environmental Science & Technology*, 43(8):2983–2988, 2009. doi: 10.1021/es802474j. URL http://dx.doi.org/10.1021/es802474j. PMID: 19475981.

[110] David G. Streets, Molly K. Devane, Zifeng Lu, Tami C. Bond, Elsie M. Sunderland, and Daniel J. Jacob. All-time releases of mercury to the atmosphere from human activities. *Environ. Sci. Technol.*, 45(24):10485–10491, November 2011. ISSN 0013-936X.

[111] Sarah A. Strode, Lyatt Jaeglé, Noelle E. Selin, Daniel J. Jacob, Rokjin J. Park, Robert M. Yantosca, Robert P. Mason, and Franz Slemr. Air-sea exchange in the global mercury cycle. *Global Biogeochem. Cycles*, 21(1):GB1017–, March 2007.

[112] D. Stroppiana, P. A. Brivio, J-M. Grégoire, C. Liousse, B. Guillaume, Claire Granier, Aude Mieville, M. Chin, and G. Pétron. Comparison of global inventories of CO emissions from biomass burning derived from remotely sensed data. *Atmos. Chem. Phys.*, 10(24):12173–12189, 2010.

[113] Mahamud Subir, Parisa A. Ariya, and Ashu P. Dastoor. A review of uncertainties in atmospheric modeling of mercury chemistry I. uncertainties in existing kinetic parameters – fundamental limitations and the importance of heterogeneous chemistry. *Atmospheric Environment*, 45(32):5664 – 5676, 2011. ISSN 1352-2310.

[114] Mahamud Subir, Parisa A. Ariya, and Ashu P. Dastoor. A review of the sources of uncertainties in atmospheric mercury modeling II. Mercury surface and heterogeneous chemistry – A missing link. *Atmos. Environ.*, 46:1 – 10, 2012. ISSN 1352-2310.

[115] Elsie M. Sunderland and Robert P. Mason. Human impacts on open ocean mercury concentrations. *Global Biogeochem. Cycles*, 21(4):GB4022–, December 2007. ISSN 0886-6236.

[116] Elsie M. Sunderland, David P. Krabbenhoft, John W. Moreau, Sarah A. Strode, and William M. Landing. Mercury sources, distribution, and bioavailability in the North Pacific Ocean: Insights from data and models. *Global Biogeochem. Cycles*, 23(2):GB2010–, May 2009. ISSN 0886-6236.

[117] M. Tiedtke. A comprehensive mass flux scheme for cumulus parameterization in large-scale models. *Mon. Wea. Rev.*, 117(8):1779–1800, August 1989. ISSN 0027-0644.

[118] O. Travnikov, J.E. Jonson, A.S Andersen, M. Gauss, A. Gusev, O. Rozovskaya, D. Simpson, V. Sokovyh, S. Valiyaveetil, and P. Wind. Development of the emep global modelling framework: Progress report.

emep/msc-e technical report 7/2009. Technical report, Meteorological Synthesizing Centre - East, Moscow, Russia, 2009.

[119] O Travnikov, JE Jonson, M Amann, J Angelbratt, M Gauss, J Griesfeller, A Gusev, C Heyes, I Ilyin, JE Jonson, et al. Global scale modelling within emep: Progress report. Technical report, Joint MSC-W/MSC-E Report. EMEP/MSC-E Technical Report 1, 2011.

[120] M.R. Turetsky, J.W. Harden, H.R. Friedli, M. Flannigan, N. Payne, J. Crock, and Radke L. Wildfires threaten mercury stocks in northern soils. *Geophys. Res. Lett.*, 33:L16403, 2006.

[121] UNEP. Mercury: Time to act. Technical report, Chemicals Branch, Division of Technology, Industry and Economics, United Nations Environment Programme (UNEP), 2013.

[122] UNEP. Global mercury assessment 2013: Sources, emissions, releases, and environmental transport. Technical report, Chemicals Branch, Division of Technology, Industry and Economics, United Nations Environment Programme (UNEP), 2013.

[123] M. Val Martin, J. A. Logan, R. A. Kahn, F.-Y. Leung, D. L. Nelson, and D. J. Diner. Smoke injection heights from fires in North America: analysis of 5 years of satellite observations. *Atmos. Chem. Phys.*, 10(4):1491–1510, February 2010. ISSN 1680-7324.

[124] Daniel Vallero. *Fundamentals of air pollution*. Academic press, 2014.

[125] G. R. van der Werf, J. T. Randerson, L. Giglio, G. J. Collatz, M. Mu, P. S. Kasibhatla, D. C. Morton, R. S. DeFries, Y. Jin, and T. T. van Leeuwen. Global fire emissions and the contribution of deforestation, savanna, forest, agricultural, and peat fires (1997–2009). *Atmos. Chem. Phys.*, 10(23): 11707–11735, 2010.

[126] T. T. van Leeuwen and G. R. van der Werf. Spatial and temporal variability in the ratio of trace gases emitted from biomass burning. *Atmos. Chem. Phys.*, 11(8):3611–3629, 2011.

[127] T. T. van Leeuwen, W. Peters, M. C. Krol, and G. R. van der Werf. Dynamic biomass burning emission factors and their impact on atmospheric CO mixing ratios. *J. Geophys. Res. Atmos.*, 118(12):6797–6815, June 2013. ISSN 2169-8996.

[128] Rik Wanninkhof. Relationship between wind speed and gas exchange over the ocean. *Journal Of Geophysical Research - Atmospheres*, 97:–, 1992.

[129] Rik Wanninkhof, William E. Asher, David T. Ho, Colm Sweeney, and Wade R. McGillis. Advances in quantifying air-sea gas exchange and environmental forcing*. *Annu. Rev. Marine. Sci.*, 1(1):213–244, January 2009. ISSN 1941-1405.

[130] C. Wiedinmyer, S. K. Akagi, R. J. Yokelson, L. K. Emmons, J. A. Al-Saadi, J. J. Orlando, and A. J. Soja. The fire inventory from NCAR (FINN): a high resolution global model to estimate the emissions from open burning. *Geosci. Model Dev.*, 4(3):625–641, 2011.

[131] Christine Wiedinmyer and Hans Friedli. Mercury emission estimates from fires: An initial inventory for the United States. *Environ. Sci. Technol.*, 41 (23):8092–8098, 2007.

[132] Jason E. Williams, Michiel van Weele, Peter F. J. van Velthoven, Marinus P. Scheele, Catherine Liousse, and Guido R. van der Werf. The Impact of Uncertainties in African Biomass Burning emission estimates on modeling global air quality, long range transport and tropospheric chemical lifetimes. *Atmosphere*, 3(1):132–163, 2012.

[133] Z.-Q. Xie, R. Sander, U. Pöschl, and F. Slemr. Simulation of atmospheric mercury depletion events (amdes) during polar springtime using the mecca box model. *Atmospheric Chemistry and Physics*, 8(23): 7165–7180, 2008. doi: 10.5194/acp-8-7165-2008. URL http://www.atmos-chem-phys.net/8/7165/2008/.

[134] X. Yang, R. A. Cox, N. J. Warwick, J. A. Pyle, G. D. Carver, F. M. O'Connor, and N. H. Savage. Tropospheric bromine chemistry and its impacts on ozone: A model study. *J. Geophys. Res. Atmos.*, 110:1984–2012, 2005.

[135] X. Yang, J. A. Pyle, R. A. Cox, N. Theys, and M. Van Roozendael. Snow-sourced bromine and its implications for polar tropospheric ozone. *Atmos. Chem. Phys.*, 10(16):7763–7773, 2010.

[136] Dušan Žagar, Nataša Sirnik, Matjaž Četina, Milena Horvat, Jože Kotnik, Nives Ogrinc, Ian M. Hedgecock, Sergio Cinnirella, Francesco De Simone, Christian N. Gencarelli, and Nicola Pirrone. Mercury in the Mediterranean. Part 2: processes and mass balance. *Environ. Sci. Pollut. Res.*, 21 (6):4081–4094, 2014. ISSN 0944-1344.

[137] Rahul A. Zaveri and Leonard K. Peters. A new lumped structure photochemical mechanism for large-scale applications. *J. Geophys. Res.*, 104 (D23):30387–30415, 1999. ISSN 0148-0227.

[138] L. Zhang, P. Blanchard, D. Johnson, A. Dastoor, A. Ryzhkov, C.J. Lin, K. Vijayaraghavan, D. Gay, T.M. Holsen, J. Huang, J.A. Graydon, V.L. St. Louis, M.S. Castro, E.K. Miller, F. Marsik, J. Lu, L. Poissant, M. Pilote, and K.M. Zhang. Assessment of modeled mercury dry deposition over the great lakes region. *Environmental Pollution*, 161(0):272 – 283, 2012. ISSN 0269-7491. doi: 10.1016/j.envpol.2011.06.003. <ce:title>Mercury in the Laurentian Great Lakes Region</ce:title>.

[139] Leiming Zhang, L Paige Wright, and Pierrette Blanchard. A review of current knowledge concerning dry deposition of atmospheric mercury. *Atmospheric Environment*, 43(37):5853–5864, 2009.

[140] Y. Zhang, L. Jaeglé, A. van Donkelaar, R. V. Martin, C. D. Holmes, H. M. Amos, Q. Wang, R. Talbot, R. Artz, S. Brooks, W. Luke, T. M. Holsen, D. Felton, E. K. Miller, K. D. Perry, D. Schmeltz, A. Steffen, R. Tordon, P. Weiss-Penzias, and R. Zsolway. Nested-grid simulation of mercury over north america. *Atmospheric Chemistry and Physics*, 12(14):6095 – 6111, 2012.

Research Products

The research was performed in the framework of the EU project GMOS (FP7 - 265113). During this three year long period the following results were produced:

De Simone, F., Cinnirella, S., Gencarelli, C., Yang, X., Hedgecock, I., Pirrone, N. (2015). **A model study of global mercury deposition from biomass burning.** Environmental science & technology 49 (11), pp 6712–6721.

DOI: 10.1021/acs.est.5b00969

Gencarelli, C. N., **De Simone, F.**, Hedgecock, I. M., Sprovieri, F., Yang, X., & Pirrone, N. (2015). **European and Mediterranean mercury modelling: local and long-range contributions to the deposition flux**. Atmospheric Environment, 117, pp 162-168, DOI: 10.1016/j.atmosenv.2015.07.015

Bieser, J., **De Simone, F.**, Gencarelli, C., Geyer, B., Hedgecock, I., Matthias, V., & Weigelt, A. (2014). **A diagnostic evaluation of modeled mercury wet depositions in Europe using atmospheric speciated high-resolution observations.** Environmental Science and Pollution Research, 21(16), pp 9995-10012.

Gencarelli, C. N., **De Simone, F.**, Hedgecock, I. M., Sprovieri, F., & Pirrone, N. (2014). **Development and application of a regional-scale atmospheric mercury model based on WRF/Chem: a Mediterranean area investigation.** Environmental Science and Pollution Research, 21(6), pp 4095-4109.

Žagar, D., Sirnik, N., Četina, M., Horvat, M., Kotnik, J., Ogrinc, N., ... **De Simone, F.**, ..., & Pirrone, N. (2014). **Mercury in the Mediterranean. Part 2: processes and mass balance.** Environmental Science and Pollution Research, 21(6), pp 4081-4094.

De Simone, F., Gencarelli, C. N., Hedgecock, I. M., & Pirrone, N. (2014). **Global atmospheric cycle of mercury: a model study on the impact of oxidation mechanisms.** Environmental Science and Pollution Research, 21(6), 4110-4123.

Gencarelli, C. N., **De Simone, F.**, Hedgecock, I. M., Sprovieri, F., & Pirrone, N. (2013). **Development of a regional scale atmospheric Hg model based on WRF-Chem: results of preliminary studies.** In E3S Web of Conferences (Vol.

1, pp 20003). EDP Sciences.